Εθνικό Μετσόβιο Πολυτεχνείο
Σχολή Πολιτικών Μηχανικών
Τομέας Γεωτεχνικής

National Technical University of Athens
School of Civil Engineering
Geotechnical Division

Διπλωματική εργασία

ΙΩΑΝΝΙΔΟΥ ΣΤΥΛΙΑΝΗΣ

Επιβλέπων:
Επίκουρος Καθηγητής Ν. Γερόλυμος

ΦΕΡΟΥΣΑ ΙΚΑΝΟΤΗΤΑ ΦΡΕΑΤΟΣ ΘΕΜΕΛΙΩΣΗΣ ΣΕ ΜΗ ΣΥΝΕΚΤΙΚΟ ΕΔΑΦΟΣ ΥΠΟ ΣΥΝΔΥΑΣΜΟ ΑΞΟΝΙΚΗΣ ΚΑΙ ΕΓΚΑΡΣΙΑΣ ΦΟΡΤΙΣΗΣ : ΑΡΙΘΜΗΤΙΚΗ ΚΑΙ ΗΜΙΑΝΑΛΥΤΙΚΗ ΕΠΙΛΥΣΗ
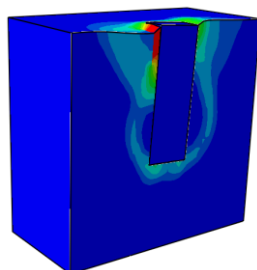
BEARING CAPACITY OF CAISSON FOUNDATIONS IN COHESIONLESS SOIL UNDER COMBINED AXIAL AND LATERAL LOADING : NUMERICAL AND ANALYTICAL STUDY

Diploma Thesis by

IOANNIDOU STYLIANI

Supervisor:
Assistant Professor N. Gerolymos

Table of Contents

CHAPTER 1

SUBJECT OF STUDY AND LITERATURE REVIEW

1.1. *Scope*

In this thesis, we examine the response of deeply embedded foundations (caissons) under combined axial, horizontal and moment loading. The initial goal of the thesis is the production of the soil-foundation system's "failure envelopes"; at the same time an effort is made to describe the laws that govern the behavior of the herein examined deeply embedded foundations, attempting to demonstrate the physical interpretation of the "failure envelopes". Furthermore, we attempt to appropriately utilize the results of three-dimensional finite element method (FEM) analyses, in order to propose closed-form analytical expressions capable of describing the capacities of the specific foundation type, as well as their yield surfaces. This approach is driven by the lack of complete tools that can effectively capture the behavior of embedded foundations under combined loading and by the need to develop an innovative mathematical tool, known as "macro-element". In the following sections a layout of the thesis is provided , as well as a short review of the literature regarding the analysis of deeply embedded foundations.

1.2. *Layout*

The second chapter deals with the modeling of the soil – foundation system using the commercial Finite Element code ABAQUS. The geometrical characteristics and constitutive laws adopted in the models, along with the Mohr-Coulomb failure criterion are analyzed in detail.

In the third chapter, we describe the methods for the conduction of the numerical analyses and present the results in terms of ultimate capacities and failure envelopes. Moreover, the importance of the use of the appropriate load reference point is examined and the method for the extraction of failure envelopes is analyzed. Throughout this chapter, the results of various embedment ratios as well as of different coefficients of friction are continuously compared.

In the fourth chapter, the soil deformation mechanisms that are mobilized during the failure of the herein investigated system are recorded; those mechanisms solely depend on the position of the examined point on the failure envelope. We classify the characteristic points of a failure envelope and map the yield locus on the M-Q plane.

In the fifth chapter, "closed-form" analytical expressions are provided for the description of the foundation's capacities. More specifically, we compose expressions appropriate for the description of the ultimate horizontal and moment capacities of caissons and eventually develop the suitable equations that describe the yielding of the herein examined foundation system.

In the last chapter, the basic conclusions derived from this thesis are summed up and further research recommendations are given.

1.3. *Use of deeply embedded foundations*

Figure 1.1 presents a rough categorization of the types of foundations that are generally used in order to support structural systems. Surface or shallow embedded foundations are distinguished by small slenderness ratios, while pile foundations are generally more slender elements. Caisson foundations lie somewhere in between in terms of slenderness or embedment; yet their limits are vague. The compressibility of the soil and the structural element should also be taken into consideration for a more realistic distinction of different foundation types.

Caisson foundations have been widely used on both soft and hard soils in order to support major structures, especially bridges. Characteristic examples include:

- the Tagus bridge in Portugal
- the San-Francisco-Oakland bay bridge
- the Williamsburg and Verrazano Narrows bridges in New York
- the Port island and Nishinomiya-ko bridges in Japan

Despite their large dimensions, caisson foundations have been shown not to be immune to seismic loading as it was believed for many years. This was confirmed in the Kobe (1995) earthquake, which caused many structures founded on caissons to suffer severe damage.

Deeply embedded foundations have also been consistently used in major offshore structures, where the study of their response under combined vertical, shear and moment loading is of great importance.

1.4. *Caisson Foundations under lateral loading*

Although a great deal of research has been done on the response of surface or shallow foundations under lateral loading and as a result numerous methods have been introduced, there is still a relatively small number of studies concerning the response of deeply embedded foundations and especially caissons. In crudely chronological order [*Gerolymos and Gazetas, 2006*], previous work on caisson foundations include: the analytical solution of Tajimi [*1969*] for a cylindrical foundation embedded in a stratum and bearing on bedrock; the versatile approximate analytical solutions of Novak and Beredugo [*1972*]; the 'consistent-boundary' finite element formulations of Kausel and Roesset [*1975*] for circular foundations in layered deposits over bedrock; the boundary element solution for rectangular foundations in a halfspace by Dominguez [*1978*]; the semi-numerical formulation of Tassoulas [*1981*] applied to embedded cylindrical foundations with variable sidewall heights; the time-domain boundary element method of Karabalis and Beskos [*1986*]; the hybrid boundary-element and finite element solution of Mita and Luco [*1989*] for square foundations embedded in a halfspace; and the 'flexible-volume' substructuring technique of Tajirian and Tabatabaie [*1981*]. Harada [*1981*] developed an approximate analytical solution for cylindrical foundations combining Tajimi's and Novak's concepts. One of the most comprehensive studies on the seismic response of flexible and rigid caissons was conducted by Saitoh [*2001*], who extended Tajimi's approximation to account for caisson flexibility and for soil and interface nonlinearities (separation and gapping of the caisson from the soil). He showed that Novak's plane strain approximation, logical as it may be, leads to inaccurate results. Most of the above methods refer to cylindrical foundations. Finally, a sophisticated and versatile Winkler model has been recently developed by Gerolymos and Gazetas [*2006*], which involves 4 types of nonlinear springs and is able to realistically simulate various foundation shapes, soil profiles, loading conditions and may

also account for interface nonlinearities. This model is analyzed extensively in the second part of this thesis.

A comprehensive series of studies on the static and dynamic response of embedded rigid foundations having various plan shapes (ranging from rectangular of any aspect ratio to triangular) have been published by Gazetas, and co-workers [*Gazetas, Dobry, Tassoulas 1985; Gazetas, Tassoulas 1987(a) και 1987(b); Fotopoulou, Kotsanopoulos, Gazetas, Tassoulas 1989*]. Utilizing an efficient boundary-element method, and numerous results from the published literature, they developed closed-form semi-analytical expressions and charts for stiffness and damping of horizontally and rotationally loaded arbitrarily-shaped rigid foundations embedded in homogeneous soil. Incomplete contact between the foundation vertical walls and the surrounding soil were taken into account in a crude way. Ample confirmation of the basic validity of some of the main concepts and results in these publications were recently provided by Gadre and Dobry [*1998*] through centrifuge modeling.

However, the above-mentioned analytical expressions and charts cannot directly apply to multi-layered soils. Furthermore, it would be impossible to even crudely extend them for use with nonlinearly behaving soils, or to model realistically phenomena such as separation (gapping) and uplifting that may take place under strong static and seismic excitation. On the other hand, the widely available commercial finite-element and finite-difference computer codes, while in principle capable of treating soil nonlinearities, are not yet an easy solution when rectangular caissons are studied (requiring a 3D mesh), embedded in deep soil deposits and subjected to seismic shaking (both requiring special and very distant boundaries), and undergoing strong oscillations with the aforementioned interface nonlinearities (requiring special interface elements).

This has led researchers to approach the response of deeply embedded foundations on the basis of "failure envelopes" or "interaction diagrams", namely the locus of points

that lead a foundation system to failure under combined *M-Q-N* loading [*Zaharescu 1961; Ticof 1977*]. Various studies have been published that deal with the capacity of –mainly-lightly embedded or surface foundations in the above sense [*Roscoe and Schofield 1957; Bransby and Randolph 1998; Taiebat and Carter 2000; Gourvenec and Randolph 2003; Gourvenec 2004, 2007, 2008; Randolph and Gourvenec 2011, Ukritchon et al. 1998; Martin and Houlsby 2001;*]

In a typical caisson foundation, the vertical component of loading originates from the weight of the supported structure as well as the self-weight of the foundation, which is of considerable importance in contrast to shallow foundations. Regarding the horizontal force and the overturning moment, the general approach so far has been that of a sDoF oscillator, where a force F is applied at a height h above the head of the caisson. This translates into a horizontal force $H = F$ as well as an overturning moment $M = F \cdot h$ at the head of the caisson. Typical loading conditions involve a small vertical component of loading (far from inducing failure in terms of vertical bearing capacity), while the combination of the two other load components *M-Q* is usually critical for the foundation.

The "interaction diagram" approach introduced by Zaharescu and Ticof has been adopted by many researchers and has considerably facilitated the design of foundations through an analytical expression of their "pure" capacities and their interaction law. However, researchers have not yet agreed upon a fixed reference point for the load components, a fact that affects the shape of the interaction diagram as will be displayed throughout this thesis.

FIGURES

$$\frac{D}{d} > 8$$

Pile

Caisson

Rigid :

$$\frac{D}{B} \approx 0.5 - 4$$

Flexible :

$$\frac{D}{B} \approx 3 - 8$$

Footing placed at depth

$$\frac{D}{B} \approx 0 - 1$$
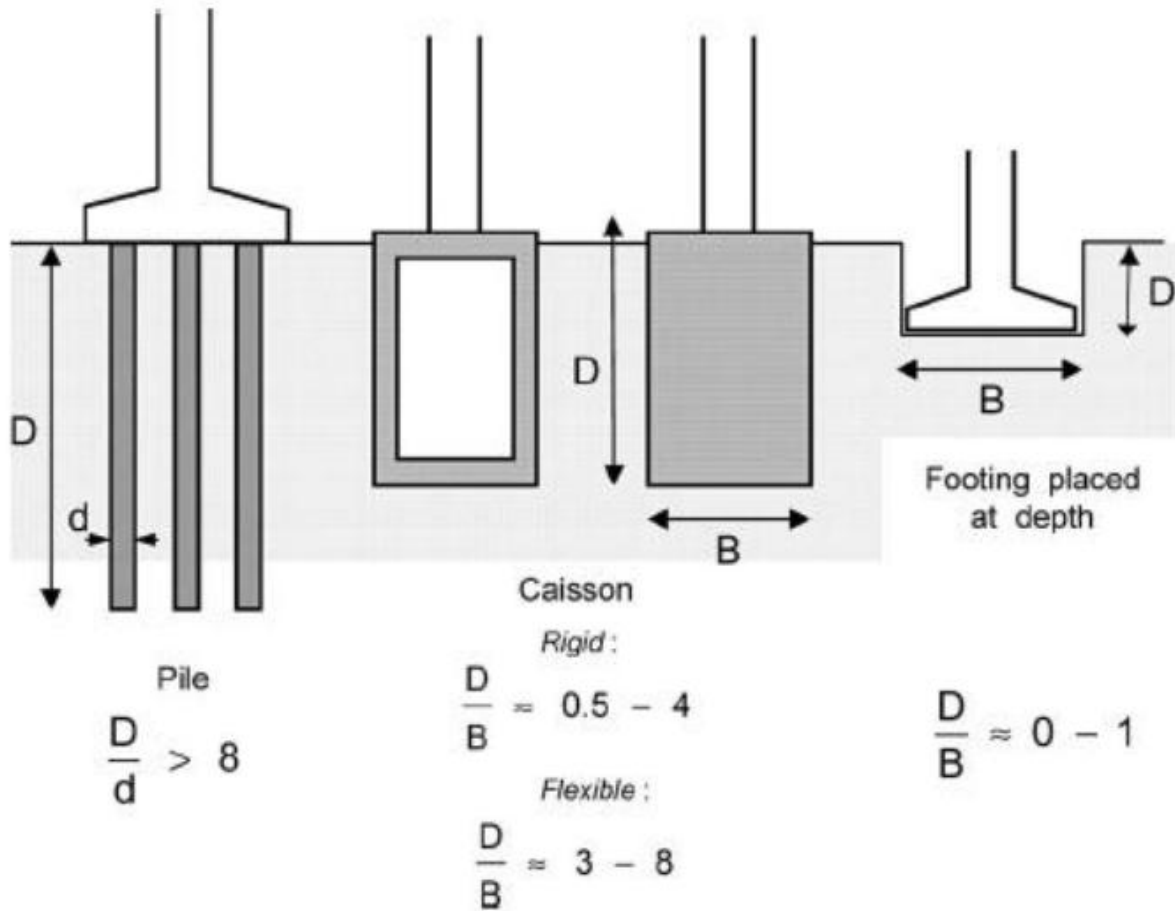
Figure 1.1 *A rough categorization of different foundation types based on their slenderness or embedment ratio D/B. From left to right we can distinguish: (a) piles (b) deeply embedded foundations (rigid and flexible) and (c) surface (or shallow) foundations. For the case of deeply embedded foundations that are studied in the herein thesis, the flexibility depends on other factors such as their material, whether they are massive or cellular, as well as on the stiffness of the surrounding soil.*

Figure 1.2 *The Tagus River Bridge in Portugal, founded on a 88-m high caisson.*

Figure 1.3 *The Nishinomiya-ko Bridge in Kobe, Japan*

Figure 1.4 *The Akashi-kaikyo bridge in Kobe, Japan founded on two massive 80-m diameter caissons.*

CHAPTER 2

FINITE ELEMENT MODELING

2.1 *Introduction*

In the following chapter, we provide the main characteristics of the three-dimensional finite element model that was created for the numerical analyses which were carried out with the finite element analysis program Abaqus. Special attention is given to the geometrical features as well as the soil's constitutive law .

2.2 *The Finite Element Model*

2.2.1. Geometry and soil properties

The herein examined problem consists of a square plan caisson of width B and embedment depth D that is subject to combined vertical load N, horizontal load Q and overturning moment M. The problem is analyzed with the use of the advanced Finite

Element code ABAQUS*. Figure 2.1.a* shows a half caisson cut through one of the orthogonal planes of symmetry. The size of the finite element mesh is 5Bx5Bx5B carefully weighing the effect of boundaries on the caisson's response and the computational time. More specifically, the boundaries should be placed far enough from the region of interest in order not to affect deformations within this region. The conservative approach would be to place the horizontal boundaries at least 5 times the width of the caisson measured from the foundations symmetrical axis, leading to a mesh 10Bx5Bx5B. However, in order to save a significant amount of computational time we examine whether the results of a 5Bx5Bx5B mesh are satisfactory compared to a 10Bx5Bx5B mesh. In *Figures 2.2* we provide indicative load-displacement curves for different coefficients of friction and factors of safety and for embedment ratio D/B=1. It is evident that both the ultimate horizontal and moment capacity do not change for a mesh of larger dimensions. We can therefore conclude that it is safe to use the 5Bx5Bx5B mesh as it does not interfere with the accuracy of our results.

In *Figure 2.1.b* the load or displacement reference point is specified as well as the signs of loads and displacements. Zero-displacement boundary conditions prevent the out of-plane displacements at the vertical sides of the model, while the base is fixed in all three coordinate directions. We investigate 3 typical embedment ratios: D/B = 1, 2 and 3 and the respective models are displayed in *Figure 2.3.* Note that embedment ratios *1* and *3* represent the limits of caisson foundations according to the conventional distinction.

Both caisson and soil are modeled with C3D8 3-D elements, elastic for the former and nonlinear for the latter. The caisson is connected to the soil through a special contact surface that allows for slippage but not separation to occur, thus permitting us to simulate reality, and we adopt a Coulomb friction law with a parametrically investigated coefficient of friction. To achieve a reasonable stable time increment without jeopardizing the accuracy of the analysis, we modified the default hard contact pressure-overclosure relationship

with a suitable exponential relationship (**Figure 2.4**). To ensure uniform stress distribution at the head of the caisson, the nodes of the associated elements are properly kinematically constrained.

2.2.2. Constitutive Soil Model

The plasticity model used in this study for cohesionless soil is an extension of the model used by Gerolymos et al *[2006]* for cohesive soils. Soil behavior is modeled through a constitutive model with kinematic hardening and associated plastic flow rule. According to this model, the evolution of stresses is described by the relation:

$$\sigma = \sigma_0 + \alpha \qquad\qquad (2.1)$$

where σ_0 is the value of stress at zero plastic strain, assumed to remain constant. The parameter α is the ''backstress'', which defines the kinematic evolution of the yield surface in the stress space. Integration of the backstress evolution law over a half cycle of a unidirectional load (e.g. tension or compression) yields the following expression:

$$\alpha = \frac{C}{\gamma}[1 - \exp(-\gamma \varepsilon^{pl})] \qquad\qquad (2.2)$$

in which C and γ are hardening parameters that define the maximum transition of the yield surface, and the rate of transition, respectively, and ε^{pl} is the plastic strain. Differentiating α with respect to ε^{pl} and taking the limit at zero, one obtains for parameter C:

$$\frac{\partial a}{\partial \varepsilon^{pl}}\Bigg|_{\varepsilon^{pl} \to 0} = C = E \qquad\qquad (2.3)$$

where E is the modulus of elasticity.

The evolution law of the model consists of two components: a kinematic hardening component, which describes the translation of the yield surface in the stress space (defined through the backstress α), and an isotropic hardening component, which defines the size of the yield surface σ_0 at zero plastic deformation. The kinematic hardening component is defined as an additive combination of a purely kinematic term (linear Ziegler hardening law) and a relaxation term (the recall term), which introduces the nonlinearity. The evolution of the kinematic component of the yield stress is described as follows:

$$\dot{a} = C\frac{1}{\sigma_0}(\sigma - \alpha)\dot{\varepsilon}^{pl} - \gamma\alpha\dot{\bar{\varepsilon}}^{pl} \qquad\qquad (2.4)$$

where $\dot{\varepsilon}^{pl}$ is the plastic flow rate (obtained through the equivalent plastic work), $\dot{\bar{\varepsilon}}^{pl}$ the equivalent plastic strain rate :

$$\dot{\bar{\varepsilon}}^{pl} = \sqrt{\frac{2}{3}\,\dot{\varepsilon}^{pl} : \dot{\varepsilon}^{pl}} \qquad\qquad (2.5)$$

The evolution law for the kinematic hardening component implies that the backstress is contained within a cylinder of radius:

$$\sqrt{\frac{2}{3}}a_s = \sqrt{\frac{2}{3}}\frac{C}{\gamma} \qquad\qquad (2.6)$$

where α_s is the magnitude of α at saturation. Since the yield surface remains bounded, this implies that any stress point must lie within a cylinder of radius $\sqrt{\frac{2}{3}}(\alpha_s + \sigma_s)$ where σ_s is the equivalent stress defining the size of the yielding surface at large plastic strain and σ_y is the uniaxial yield stress given by :

$$\sigma_y = \frac{C}{\gamma} + \sigma_0 \tag{2.7}$$

In the Mohr-Coulomb failure criterion σ_y is equal to :

$$\sigma_y = \sqrt{3J_2} \tag{2.8}$$

in which $\sqrt{J_2}$ is the square root of the second deviatoric stress invariant that satisfies the following equation:

$$I_1 \sin \varphi + \frac{1}{2}[3(1 - \sin \varphi) \sin \theta + \sqrt{3}(3 + \sin \varphi) \cos \theta]\sqrt{J_2} - $$
$$- 3c \cos \varphi = 0 \tag{2.9}$$

where I_1 is the first principal stress invariant , c is the cohesion, φ is the friction angle and θ the Lode angle which is given by :

$$\cos 3\theta = \frac{3\sqrt{3}}{2} \frac{J_3}{J_2^{3/2}} \tag{2.10}$$

where J_2 and J_3 are the second and third deviatoric stress invariants. Combining equations *(2.3)*, *(2.9)* and *(2.10)* one obtains for γ :

$$\gamma = \frac{E}{\sqrt{3J_2}} - \sigma_0 \qquad \textbf{(2.11)}$$

A user subroutine is imported in ABAQUS, which relates the model parameters to the principal stresses and the Lode angle at every loading step. Incorporating the Lode angle effect allows for significant accuracy in three-dimensional shear response environments. The yield surface of the proposed constitutive model is determined to fit the Mohr–Coulomb failure response in a triaxial loading test for both compression and extension conditions assuming linear interpolation for the intermediate stress states. For this reason, the parameter k is introduced which is a function of Lode angle and takes values from 0 to 1. k = 0 corresponds to pure triaxial extension conditions and k = 1 to pure triaxial compression conditions. In summary, the constitutive model parameters are calibrated to match the Coulomb failure criterion on the principal stresses plane for every apex of the hexagon with the smooth envelope of *Figure 2.5.*

In this study, the distribution of tangent Young's Modulus varies parabolically with depth according to:

$$C = E = E_0\, p^m \qquad \textbf{(2.12)}$$

where E_0 is the reference Young's Modulus, p is a stress invariant and m is a parameter that defines the rate of increase of E with depth.

In ***Figure 2.6*** the soil profile considered in the FE analyses is presented. The herein examined cohesionless soil has the following characteristics:

- friction angle $\varphi=30^{0}$
- mass density $\rho=2\ Mg/m^3$
- Poisson's ratio $v=0.25$
- Shear modulus $G_o=1000\ k_{II}\ \sqrt{p}$ (empirical relation for cohesionless soils). For a loose sand ($D_r \sim 35\%$) $k_{II} =8$, therefore $G_o= 8000\sqrt{p}$ and Young's modulus $E_o = 2\ G_o (1 + v)= 20000\sqrt{p}.$
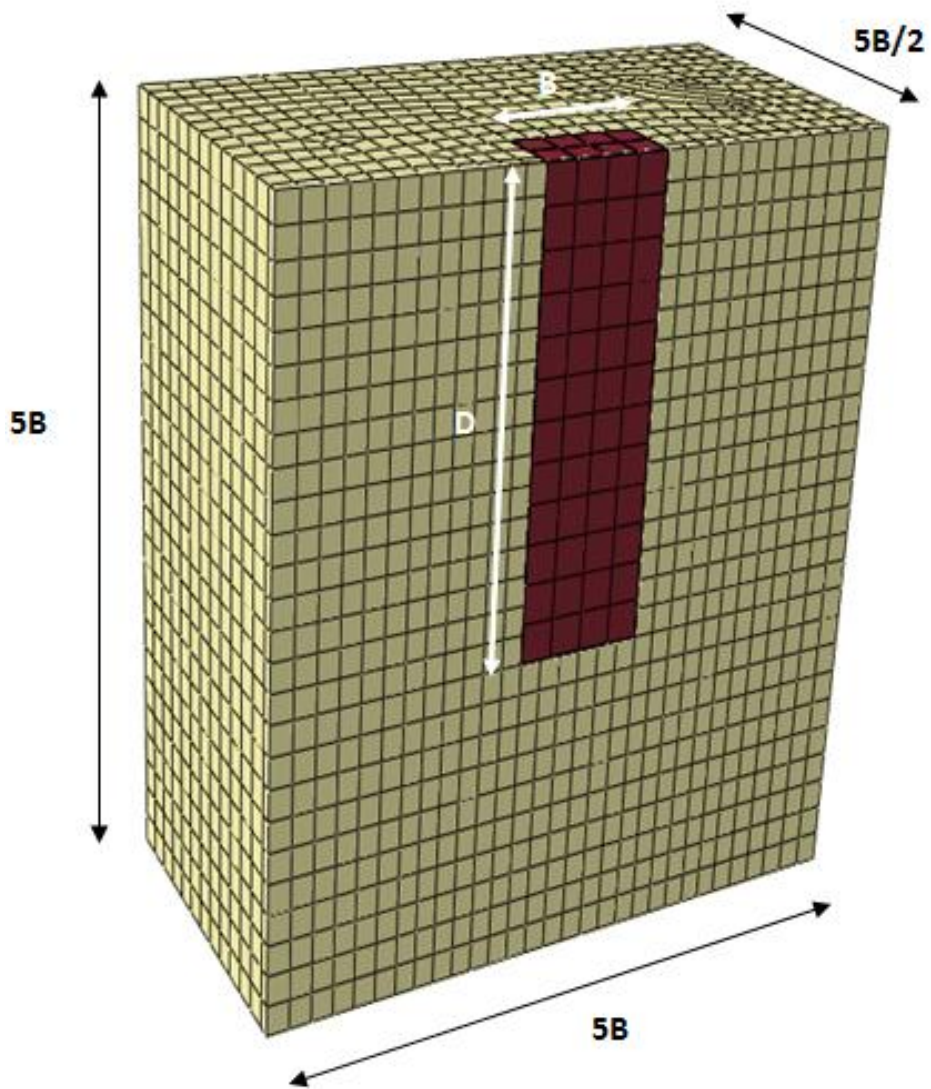
FIGURES

**Figure 2.1.a** *Geometry of the 3D Finite Element model used in the numerical analyses*
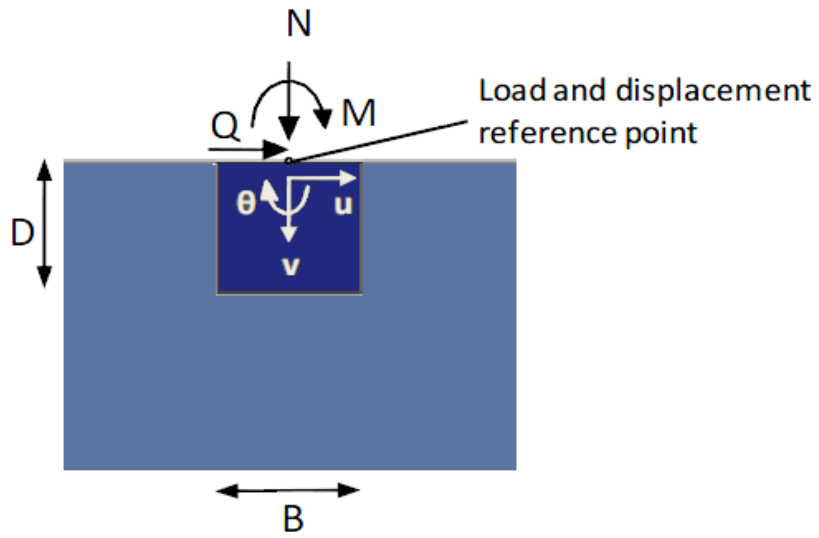
Figure 2.1.b *Displacement and load sign conventions as well as load and displacement reference point.*

a)

b)

c)

d)

e)
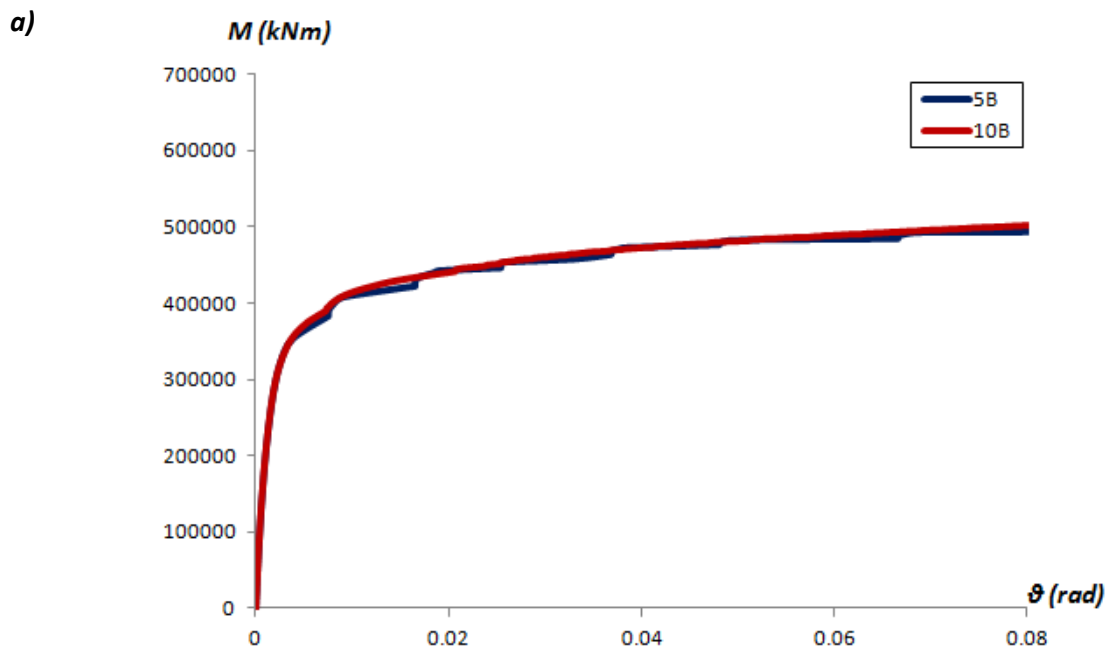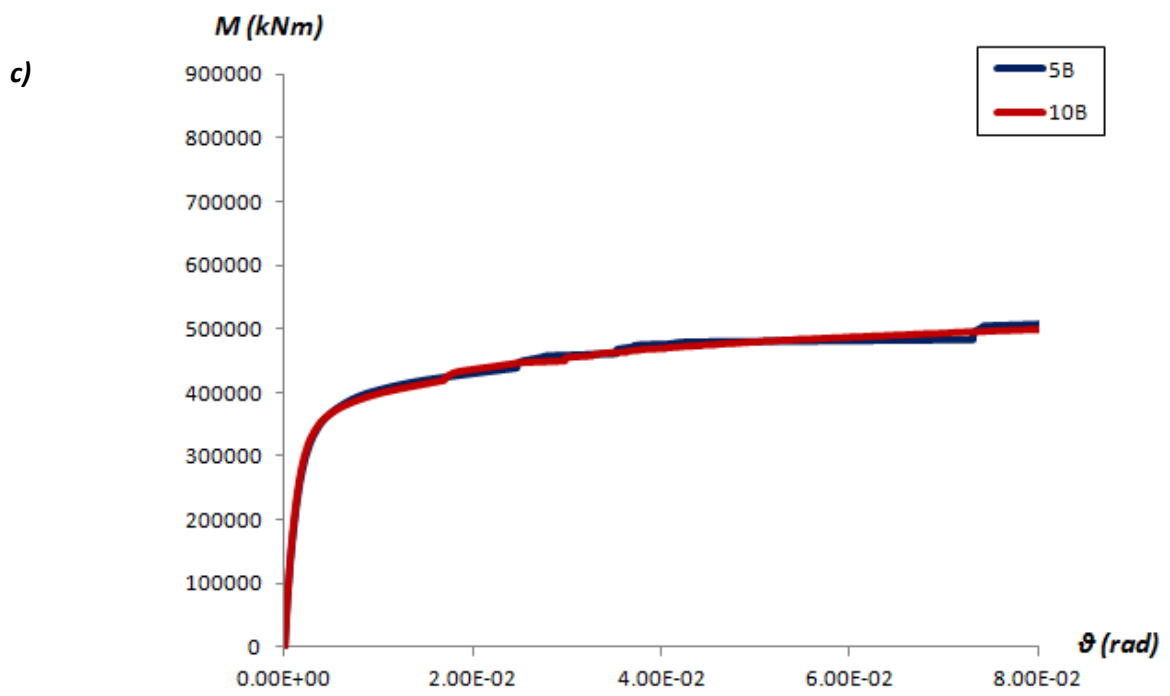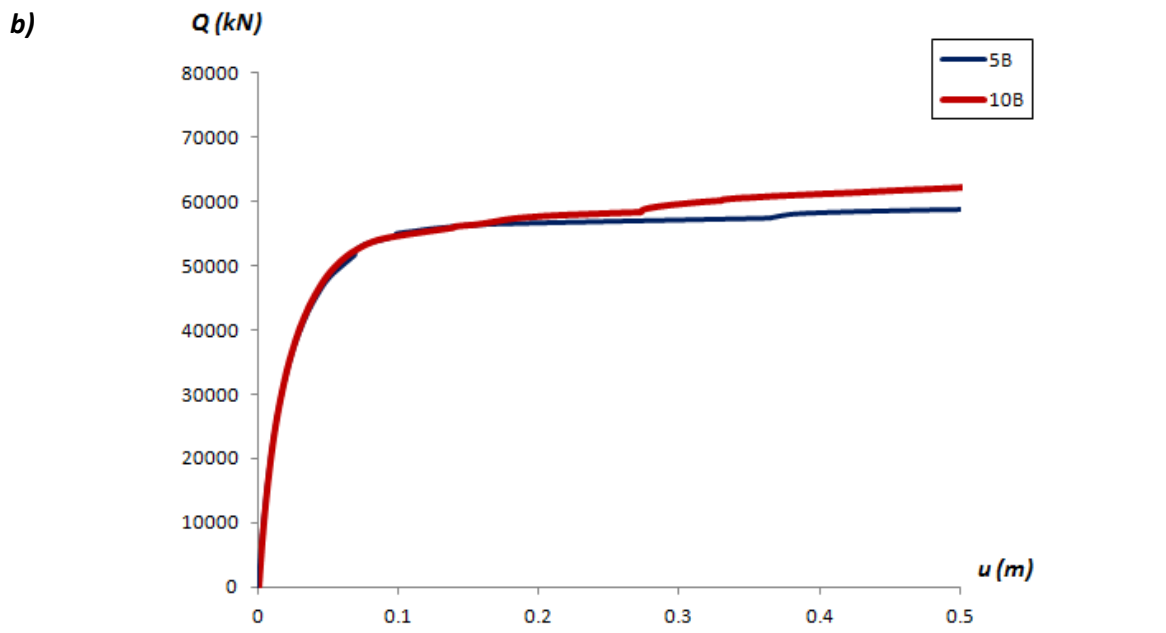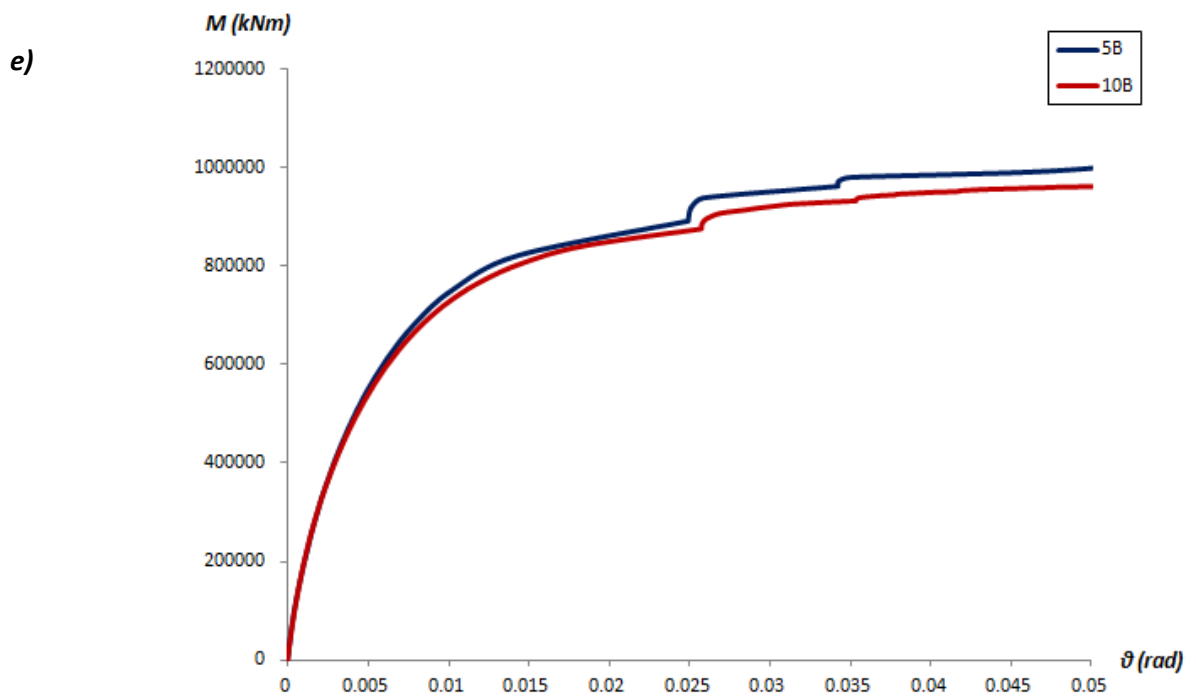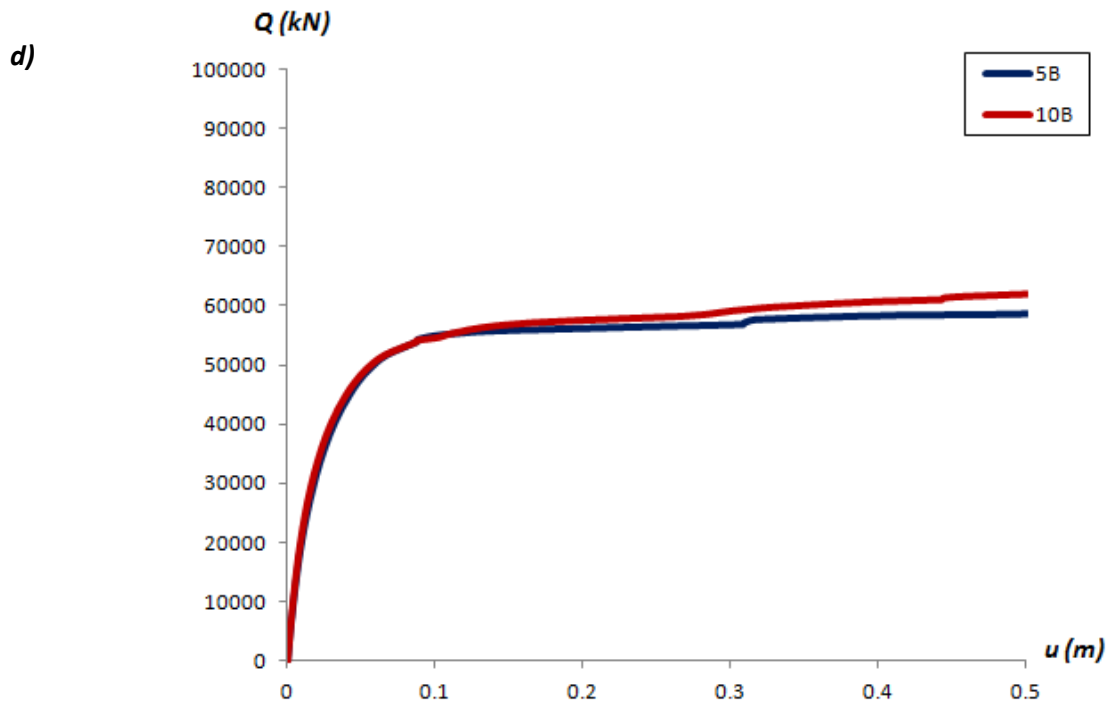
Figure 2.2 *Comparison of static pushover tests for mesh 5Bx5Bx5B and 10Bx5Bx5B* **(a)** *Moment-rotation curve for $FS_v=\infty$, $\mu=1$* **(b)** *Horizontal load-displacement curve for $FS_v=\infty$, $\mu=1$* **(c)** *Moment-rotation curve for $FS_v=\infty$, $\mu=0.5$* **(d)** *Horizontal load-displacement curve for $FS_v=\infty$, $\mu=0.5$* **(e)** *Moment-rotation curve for $FS_v=2$, $\mu=1$.*

a)

b)
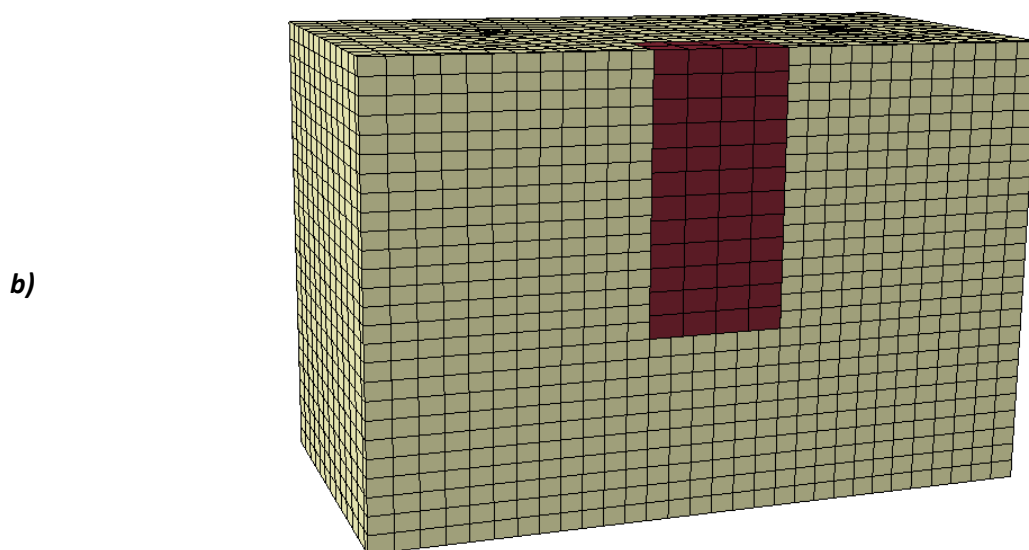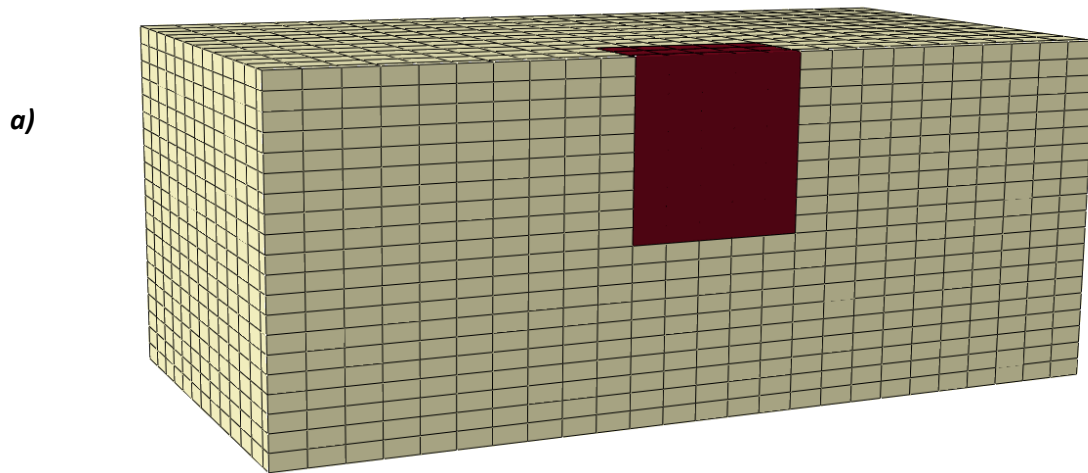
c)
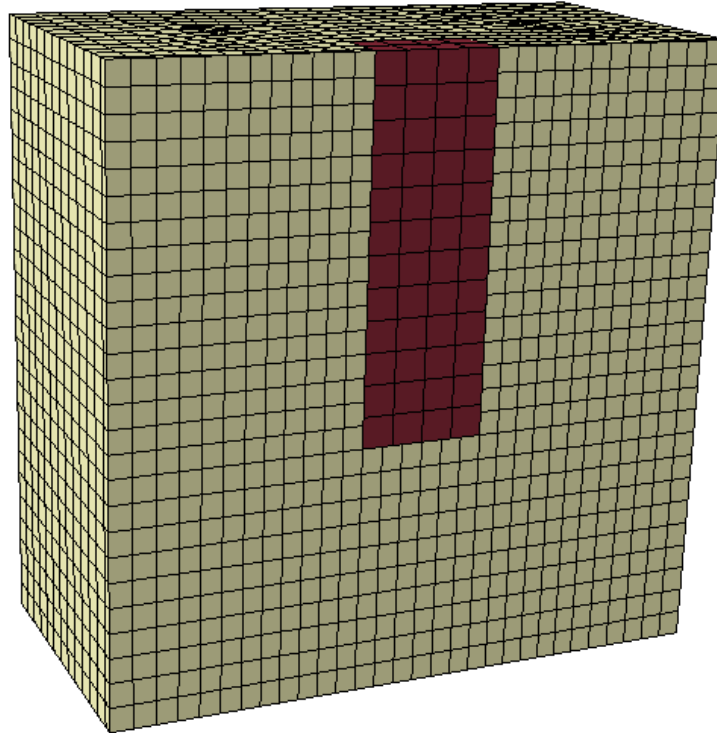
Figure 2.3 *3-D visualization of the FE models for the three embedment ratios considered. a) D/B = 1,*
*b) D/B = 2, c) D/B = 3*
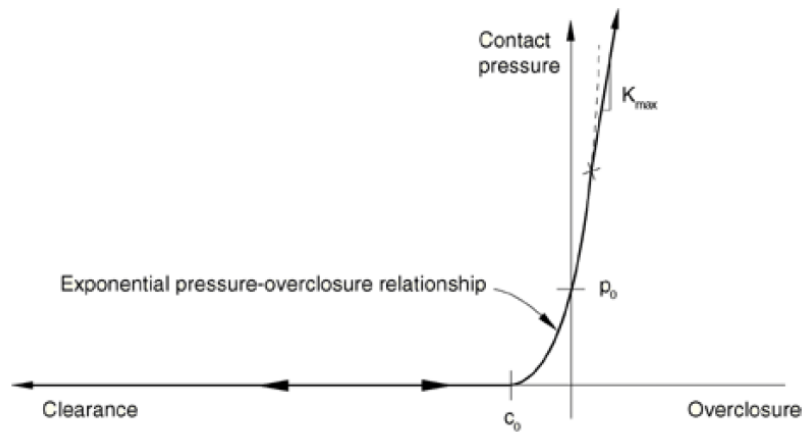
Figure 2.4 *The modified pressure-overclosure relationship for the nonlinear interface adopted in the*
model

a)

σ

σ_y

σ_0

σ_0

σ_0

σ_0

$\alpha^s + \sigma_0$

α

$\alpha^s = C/\gamma$

0

ε^{pl}

b)

σ'_1

$\sqrt{\dfrac{2}{3}}\,\sigma_y$

Triaxial Compression

Mohr-Coulomb Surface

$\sqrt{\dfrac{2}{3}}\dfrac{C}{\gamma}$

$\dfrac{\partial F}{\partial \sigma}$

$\sqrt{\dfrac{2}{3}}\,\sigma_0$

Triaxial Extension

α^{dev}

limit surface

σ'_2

limiting location of α

yield surface

σ'_3
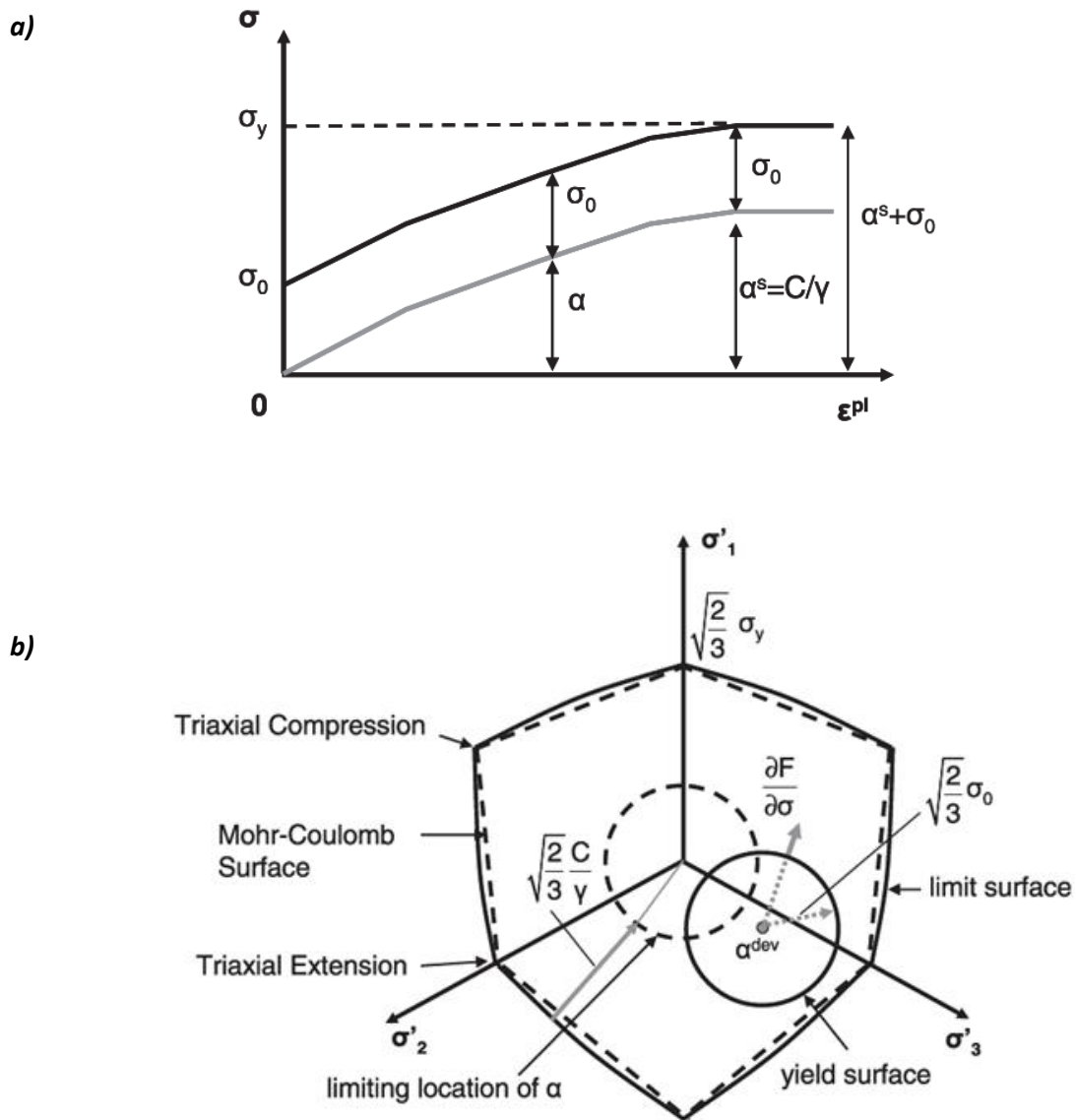
Figure 2.5 (a) *Simplified one-dimensional representation of the hardening* **(b)** *Three-dimensional representation of the hardening in the nonlinear isotropic/kinematic model*
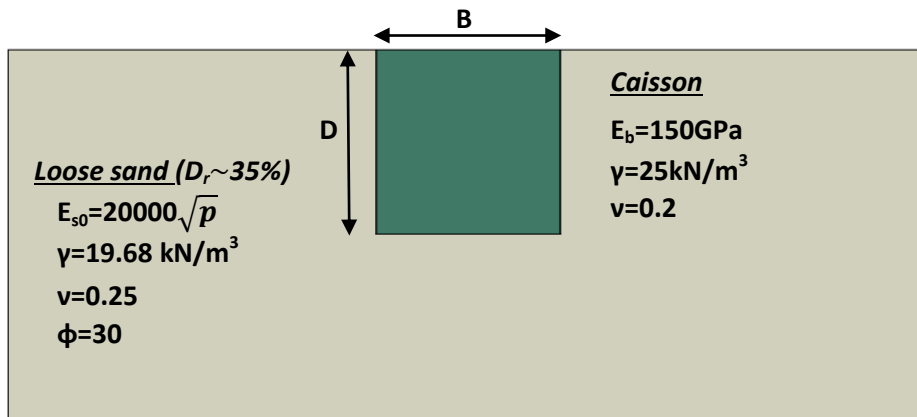
Figure 2.6 *The soil profile considered in the FE analyses. The enormous stiffness ratio renders the foundation absolutely rigid with respect to the caisson for the embedment ratios considered.*

CHAPTER 3

FAILURE ENVELOPES

3.1 _Introduction_

The primary goal of the three-dimensional analyses that are executed with the finite element modeling program ABAQUS is the production of deeply embedded foundations' - caissons - failure envelopes in cohesionless soil for different coefficients of friction and embedment ratios. Similar work has already been carried out for foundations embedded in cohesive soil for the cases of both "bonded interface" _[Gerolymos, Souliotis 2012]_ - and of "nonlinear interface" _[Gerolymos, Karapiperis 2012]._

The term "failure envelope" defines the locus of the points that represent failure of the foundation in _M-Q-N_ space. The relationship between two of the above – in other words a cross-section of the failure envelope – is conventionally termed an "interaction curve". However the term "failure envelope" is preferred over the term "interaction curve" to better describe the interdependent relationship of the three section forces (the vertical load N, the horizontal load Q and the moment load M) which is after all solely responsible for the soil-foundation system's failure. Besides, the loading of the caisson, being coplanar, only permits displacements along three "active" degrees of freedom at the load reference

point of the foundation: vertical displacement v, horizontal displacement u and rotation θ *(Figure 3.1)*. Therefore, since the 6-degree-of-freedom system is reduced to a 3-degree-of-freedom system we are able to graphically define the failure envelopes of a deeply embedded foundation by specifying in *M-Q-N* space every point that represents failure. *Figures 3.2 a* and *3.2 b* depict typical failure envelopes of surface foundations on sand [*Nova and Montrasio 1991; Gottardi and Butterfield 1995; Chatzigogos, Figini, Pecker, Salençon 2011*] and clay respectively [*Cremer, Pecker, Davenne 2001*]).

Literature provides us with many different methods of producing failure envelopes of embedded foundations, through an appropriate expansion of similar methods that pertain to surface foundations. The two most common methods are (a) static pushover tests and (b) swipe tests and they are distinguished by different loading paths leading to the failure of the soil-foundation system. In this thesis, static pushover tests are used to extract the failure envelopes. In the following section the impact of the foundation's load reference point on the shape of a failure envelope is examined.

3.2 *Load reference point*

The choice of the appropriate load reference point is of great importance, since it immediately affects the shape of a failure envelope. In *Figure 3.3* different failure envelopes of shallow foundations are presented and absolute symmetry can be observed. Furthermore, we do not detect an enhanced capacity for the system. Therefore, as far as surface foundations are concerned, the load reference point is of little significance to the failure envelopes' shape and the base of the foundation is chosen as such (*Figure 3.4*).

On the contrary, in embedded foundations (and especially in deeply embedded foundations that are examined in this thesis) the choice of the load or displacement reference point is of greater impact. In *Figure 3.5* a random example of a deeply embedded foundation's failure envelope [in terms of horizontal load-moment (Q-M)] is provided. In the specific example the embedment ratio D/B = 1, and the load reference point is the centre of the foundation's base. The branch of over-strength is specifically observed in the first quadrant , i.e. where the horizontal load and the moment are of same sign (positive). On the other hand, in *Figure 3.6* the corresponding failure envelope of the same embedded foundation is illustrated, for the same embedment ratio, also in terms of horizontal load-moment (Q-M) but with a different load of reference point: the centre of the foundation's head . As a result of this simple shift of the reference point, the over-strength is now observed in the fourth quadrant, for positive horizontal load and negative moment. Considering that the change of load reference point is the only difference between the two models, we can conclude that it is also the cause of the failure envelope's shape alteration.

This shape difference between the failure envelopes of the two embedded foundations can be attributed to the different ways in which the loading itself can cause the system soil-foundation to result in different deformations when imposed on another load reference point. In the first case, when the load is imposed on the centre of the foundation's base, the combination of positive horizontal load and positive moment guides the system to an enhanced capacity because the two same signed loads are competitive : each one attempts to balance the effect of the other resulting in a system of enhanced load-bearing capacity. On the contrary, when the load reference point concurs with the centre of the foundation's head, similar "competitive" behavior can be observed for the combination of positive horizontal load and negative moment. In *Figure 3.7* the deformation of the soil-foundation system for the two aforementioned occasions is illustrated with very similar results. Therefore, the load reference point only affects the

failure envelopes' shape and in this specific study the chosen point is the centre of the foundation's head.

3.3 _Static Pushover Tests_

3.3.1. Introduction

In this method, static pushover tests are conducted in the horizontal load-moment plane, Q-M. Having defined the system's failure criterion, it remains to determine the way in which the loading is imposed on the foundation, causing it to fail. In the herein thesis, a realistic approach of the embedded foundation's actual loading is attempted. Besides, if the construction that is founded on the caisson can be simulated with a 1 degree of freedom (1-Dof) oscillator (e.g. a bridge pier in dynamic problems) or generally with a cantilever (e.g. a bridge pier in pseudo-static analyses of seismic problems) then it follows that radial loading paths on the Q-M plane, under constant vertical load N, should be applied in the system _[Cremer, Pecker, Davenne 2001; Gouvernec 2004; Gajan, Kutter, Phalen, Hutchinson, Martin 2005]._ In **Figure 3.8** the radial loading paths in the loading plane Q-M are portrayed, as they were defined by Cremer, Pecker και Davenne [_2001_] for constructions characterized by one mode during dynamic problems' analyses. Considering that on the mass centre of the superstructure an inertial force $F = ma$ is imposed, in h_i distance from the foundation level, then a moment of $M = Fh_i = mah_i$ is transferred to the foundation, as well as a horizontal load equal to the inertial force ($Q=F=ma$). At the same time, the vertical load imposed on the foundation is maintained constant and equal to the self-weight of the superstructure $N = W = mg$.

3.3.2. Designing the numerical analyses

In the present thesis, we initially chose as a load reference point the centre of the caisson's head. The steps followed in our numerical experiments represent the actual conditions in the field. The soil undergoes geostatic loading and then a part of the soil is replaced by the foundation, on which a vertical load N is imposed on the load reference point increasingly till a specified value of $\chi = N/Nu$ is reached. Afterwards, the vertical load is kept constant, and a combination of horizontal force and moment is imposed on the head of the caisson till the complete failure of the system. As state of failure we consider the point at which the change in the section forces is equal to zero : the soil-foundation system is incapable of undertaking any more load. Our aim is to extract the ultimate capacities under moment M_u and horizontal force Q_u, and then sweep the M-Q plane so that a cross-section of the failure envelope is revealed.

More specifically, for a given embedment ratio D/B (i.e. for a given foundation geometry), we calculate the soil-foundation system's bearing capacity against vertical loading (N_u). Then, nine different static safety factors are examined : FS_v=1.11; 1.25; 1.43; 1.66; 2; 2.5; 3.33; 5; 10 και ∞ (for vertical load equal to zero). In this study, however, instead of presenting the results with respect to the safety factor FS_V, we adopt the inverse of the static safety factor, namely $\chi = 1/FS_v = N/N_u$ with values χ = 0.9; 0.8; 0.7; 0.6; 0.5; 0.4;0.3; 0.2; 0.1 και 0 respectively. Subsequently, while maintaining a constant vertical load, we initially calculate the pure capacities in horizontal load and moment (Q_u and M_u respectively) for each factor of safety FS_v. As pure horizontal load capacity (or moment) we define the maximum horizontal load (or moment) that can be undertaken by the foundation's system (imposed on the load reference point, aka the head of the caisson) under zero moment (or horizontal load respectively) , as shown in *Figure 3.9*. We then perform a satisfactory number of static pushover tests for every factor of safety separately,

applying radial loading paths on the Q-M plane at the system. As a result, we can determine the section forces at the moment of failure and for their better presentation through failure envelopes, we normalize these results with their corresponding ultimate capacities (Q/Q_u and M/M_u), according to the suggestions of researchers concerning the behavior of deeply embedded foundations [*Bransby and Randolph 1999a; Gourvenec and Randolph 2003*]. Thus, by following the above procedure of static pushover tests we can produce the desired failure envelopes of the soil-caisson system in Q-M plane.

3.3.3. Results

Figures 3.10(a), (b) and **(c)** illustrate the change in ultimate horizontal and moment capacity of caisson foundations of three distinct embedment ratios *1, 2* and *3* with respect to the inverse factor of safety *χ,* for coefficient of friction μ=1. Those capacities M_u and Q_u are normalized by their respective ultimate pure capacities for zero vertical load and a specific value of embedment ratio D/B and coefficient of friction, M_u* and Q_u*. **Figures 3.12(a), (b), 3.14(a), (b)** and **3.16(a), (b)** illustrate the ultimate horizontal and moment capacities of caisson foundations of embedment ratios *1, 2* and *3* respectively, for coefficients of friction μ=0.5 and μ=0.3 , as we wish to examine the system's behavior transitioning from a smooth interface where slippage is likely to occur (μ=0.3) to a rough interface of μ=1. Finally, in **Figures 3.11(a)** and **(b)** we contrast the results for different embedment ratios while in **Figures 3.13(a), (b), 3.15(a), (b)** and **3.17(a),(b)** we attempt to illustrate the influence of the coefficient of friction on ultimate moment and horizontal capacities, for embedment ratios 1, 2 and 3 respectively.

In **Figures 3.19 - 3.31** we present the aforementioned failure envelopes, each for a given static safety factor FS_v, a given coefficient of friction μ and of course a given

embedment ratio D/B. It should be noted that we have normalized the quantities Q and M by their ultimate capacities Q_u and M_u respectively and then used the results to produce the failure envelopes in terms of Q/Q_u and M/M_u. Bransby και Randolph *[1999]* studied the shape of failure envelopes for shallow foundations and noticed that the shape remains the same when the quantities are normalized by their ultimate capacities. However, their research was limited only to one embedment ratio (and a small one for that matter) , D/B = 0.167 , constituting their result in need of confirmation. For this reason, we choose to present failure envelopes where the results are normalized by their ultimate capacities, for each embedment ratio D/B, safety factor FS_v and coefficient of friction μ. In addition, (assuming the accuracy of Bransby and Randolf's observation) the benefit of this method lies in the fact that, to define the system's response, we are only required to know the system's ultimate capacities along with its bearing capacity of vertical load. This particular benefit of the normalized failure envelopes can help us mathematically describe the caissons' behavior, especially in order to model the soil-foundation system using an appropriate mathematical tool ("macro-element modeling"). In ***Figures 3.19 - 3.20*** the normalized failure envelopes for D/B=1 and μ=1 are illustrated for every examined static safety factor. Then, in ***Figures 3.21 - 3.22*** and ***Figures 3.23 - 3.24*** we depict the failure envelopes for D/B=2 and μ=1 and for D/B=3 and μ=1 respectively. All in all, the shape of the failure envelopes can be approximated by an oblique ellipse in M-Q space, whose eccentricity grows accordingly to the embedment ratio D/B [*Yun and Bransby 2007a*].

3.3.4. Analyzing the results

3.3.4.1. Comparing Ultimate Capacities for different embedment ratios and coefficients of friction

Figure 3.10(a) shows the normalized horizontal and moment capacities for the embedment ratio D/B=1 and for a coefficient of friction μ =1. As the vertical load increases, the ultimate lateral capacities increase until they reach a peak at $\chi \approx 0.5$. However, as the vertical loading becomes more considerable, the trend is reversed and a decrease is evident, with the lateral capacities approaching their $\chi=0$ values. Finally, as the vertical load approaches the foundation's vertical capacity, the lateral capacities decline sharply until they are nullified for $\chi = 1$.

Two antagonistic mechanisms are observed, the interplay between which leads to the parabolic shape displayed. For $\chi < 0.5$ the interface enjoys an increase in the total normal force applied both on the sidewalls and the base, while the plastification around the caisson is still limited. Taking into account the nature of the Coulomb law, the interface's shear strength and hence the foundation's overall lateral capacity is increased. Above that limit value of χ, however, the plastification taking place in the soil immediately surrounding the caisson becomes considerable and the lateral capacity starts to decline. Apparently, until $\chi = 1$, plastification governs the overall response in the last branch of the curve.

In *Figure 3.10(b)* and *(c)* we examine the behavior of the foundation's lateral capacities for embedment ratios 2 and 3. In general, embedment increases vertical, horizontal and moment capacity as failure mechanisms are forced deeper within the soil

mass. However, in the herein study we are more interested in emphasizing the effect of embedment in the shape of the normalized M-N curve. Apparently, as the embedment ratio increases, the maximum of the normalized lateral capacity no longer manifests itself for χ=0.5 but rather "moves" towards larger values of χ while at the same time the maximum value itself decreases. More specifically, while for D/B=1 the maximum of the lateral capacities is observed for χ=0.5, for D/B=3 it is not manifested until χ=0.7 or even χ=0.8, its value decreasing from $2.2M_u^*$ ($2.2Q_u^*$) for D/B=1 to $1.4M_u^*$ ($1.4Q_u^*$) for D/B=3. The maximum's shift to greater values of χ can be attributed to the fact that for larger embedment ratios the plastification of the soil surrounding the caisson is less considerable and therefore does not cause the lateral capacity to decline. As for the decrease in the value of the normalized lateral capacity, it can be attributed to the weakening influence of the caisson's base: for a small embedment ratio the foundation's base enhances the system, but as the embedment ratio increases, the base no longer affects the system's overall behavior.

In *Figure 3.13* we compare the system's lateral capacities for different coefficients of friction and for embedment ratio D/B=1 and we can notice that for a smoother soil-caisson interface (μ=0.5 and μ=0.3) the caisson lateral capacity is considerably smaller than that for a rougher interface (μ=1), since as the coefficient of friction decreases so does the soil's shear strength according to Coulomb's law thus resulting in smaller values for lateral capacities.

In *Figures 3.15* and *3.17* we observe the foundation's lateral capacities for different coefficients of friction and for embedment ratios D/B=2 and D/B=3 respectively. In this case, it is evident that by decreasing the coefficient of friction the lateral capacity curves- with respect to the inverse factor of safety χ- tend to coincide, leading us to deduce that as the embedment ratio increases, friction is no longer a determining factor. However, in

these figures it is also evident that, when dealing with a smoother soil-foundation interface (i.e. μ=0.5-0.3), for values of the inverse safety factor χ>0.7 (where for a rough interface the plastification is prevalent thus causing the lateral capacity to decline), the lateral capacity continues to ascend until χ ≈ 1, when it is abruptly nullified. To better understand this particular behavior, we employ snapshots of plastic strain magnitude contours both at the moment of failure and at the moment before imposing the lateral load, for safety factors FS_v=2 and FS_v=1.11 and for a rough (μ=1) and a smoother (μ=0.5) interface (**Figure 3.18)**. It is evident that as the coefficient of friction decreases, the shear strains caused by the vertical load are minimized and the lateral capacity reaches its maximum for χ≈1 as there is no significant plastification to cause the decline of the curve, except for the plastification of the base which is irrelevant for embedment ratio greater than 2. Furthermore, since for a smoother interface the vertical load no longer greatly affects the surrounding soil, the mechanisms that govern the lateral and vertical behavior of the foundation become independent, thus causing the abrupt nullification of the lateral capacity for inverse safety factor χ=1.

3.3.4.2. Comparing Failure Envelopes for different embedment ratios and coefficients of friction

Bransby and Randolph observed that the shape of shallow foundations' normalized failure envelopes remains the same regardless of the static safety factor FS_v and the embedment ratio D/B, as did Gerolymos and Souliotis *[2012]* and Gerolymos and Karapiperis *[2012]* for deeply embedded foundations in cohesive soil for bonded and non-linear interface respectively. However, in this study, as can be depicted in **Figures 3.20, 3.22** and **3.24** (where all the failure envelopes are illustrated at the same time for embedment ratios D/B=1, 2 and 3 respectively) it is obvious that we cannot disregard the

impact of the static safety factor FS_v. For embedment ratios less than D/B=3, the failure envelopes develop a rather distinct variability with FS_v, specifically in the branch of overstrength. That is to be expected, as it is in agreement with our results concerning the foundation's ultimate lateral capacities that we analyzed above. For larger embedment ratios such as D/B=3 we can observe that failure envelopes coincide for different vertical safety factors. Furthermore, in *Figure 3.25* we examine the failure envelopes for three different embedment ratios (D/B=1, 2, 3) and the same static safety factor (FS_v =2.5) and observe that as the embedment ratio increases the failure envelopes expand (or according to Yun and Bransby *[2007]* become increasingly eccentric) along the major axis of the oblique ellipse (a.k.a. for positive horizontal load and negative moment). It is worth mentioning that this expansion is more noticeable for the transition from embedment ratio D/B=1 to D/B=2 and weakens when transitioning from D/B=2 to D/B=3.

In *Figures 3.26* through *3.31* we attempt to examine the failure envelopes of deeply embedded foundations under different coefficients of friction, for embedment ratios D/B=1, 2 and 3. More specifically, in *Figures 3.26, 3.27* we depict the failure envelopes for embedment ratio D/B=1 and for static safety factors FS_v=2 and FS_v=1.11 respectively. The reason we chose to examine these particular safety factors lies in the fact that when observing the failure envelopes for a coefficient of friction equal to 1 (μ=1), we notice that

- for FS_v=2 the foundation's enhanced horizontal capacity reaches a minimum, thus constituting it worthwhile examining.
- for FS_v=1.11 the vertical load approaches the foundation's ultimate load-bearing capacity, while at the same time the system's enhanced horizontal capacity is reaching close to a maximum.

Therefore, we conduct numerical analyses for D/B=1, for the aforementioned safety factors and for 2 coefficients of friction: μ=0.5 and μ=0.3, transitioning from conditions where slippage is considerably limited (μ=1) to a smoother soil-caisson interface where slippage is

likely to occur at the very early stages of loading. From **Figures 3.26, 3.27** we can remark a significant increase in the branch of over-strength as the coefficient of friction is reduced and slippage is permitted.

In **Figures 3.28** and **3.29** the failure envelopes for a foundation with an embedment ratio of D/B=2 are illustrated, for the coefficients of friction μ=1, μ=0.5 and μ=0.3. It is worth noting that as the embedment ratio increases from D/B=1 to D/B=2 the failure envelopes tend to coincide for different coefficients of friction. Therefore, for embedment ratio D/B=3 we choose to examine and contrast only the failure envelopes of the two extreme cases of μ=1 (limited slippage) and μ=0.3 (smoother surface), as depicted in **Figures 3.30** and **3.31.** Considering the results, we reach the conclusion that as the embedment ratio increases the dependency of the failure envelope on the coefficient of friction weakens. It is also worth indicating that this weakening is more noticeable for the transition from D/B=1 to D/B=2 than from D/B=2 to D/B=3. In fact, we could claim that for an embedment ratio greater than 2 friction no longer influences the foundation's failure envelopes.

3.3.4.3. Load-displacement curves

In **Figures 3.33** we illustrate load- horizontal displacement curves (Q-u) as well as moment- rotation curves (M-θ) at the centre of the foundation's head, in respect to the embedment ratio D/B. More specifically, **Figures 3.33** correspond to the safety factor FS_v=10 and concern three different point of the failure envelope as depicted in **Figure 3.32**. The influence of the embedment ratio is evident both in terms of ultimate capacity and in terms of stiffness , therefore we do not need to further analyze the results.

3.3.4.4. *The advantage of normalizing Failure Envelopes with their ultimate capacities.*

Figures 3.34 through *3.36* depict the foundation's *dimensionless* failure envelopes for coefficient of friction μ=1 and different embedment ratios and safety factors. In contrast to the aforementioned failure envelopes, we choose to normalize quantities M and Q with the geometrical characteristics of the foundation (width **B** and embedment depth **D**) , as well as with the soil's unit weight **γ** and the constant k_p= $\tan^2$(45+φ/2). More specifically, the moment axis is normalized by the quantity $\mathbf{k_p \gamma DB^3}$ and the horizontal load axis is normalized by the quantity $\mathbf{k_p \gamma DB^2}$. It is evident for every embedment ratio that the safety factor FS_v affects the failure envelopes' shape; in fact the opposite trend observed for envelopes normalized by their ultimate capacities is noticed here: for D/B=1 as the safety factor decreases from FS_v=10 to FS_v=2 (where the maximum ultimate capacity is achieved) the failure envelopes expand and then from FS_v=2 to FS_v=1.11 they shrink back. Accordingly, the same trend can be observed for embedment ratios D/B=2 and D/=3 ,where the maximum expansion is achieved for FS_v=1.43 and FS_v=1.25 respectively. Furthermore, comparing failure envelopes for the same safety factor FS_v, one can notice a striking rotation as the embedment ratio increases. This rotation is obvious in *Figures 3.37* , for several safety factors and embedment ratios 1,2 and 3.

All in all, based on the aforementioned observations, we can conclude that normalizing failure envelopes by their geometrical characteristics deprives us from certain advantages: failure envelopes experience a significant rotation in respect to the embedment ratio and additionally, the expansive behavior is not as clear as it was for envelopes normalized by their ultimate capacities. Therefore, it is significantly more

convenient for us to mathematically express the response of deeply embedded foundations utilizing envelopes that are normalized by their ultimate capacities and that is why we choose in the herein thesis to only present failure envelopes in this form.

3.3.4.5. The "shape" of Failure Envelopes

All the failure envelopes produced through the numerical analyses we conducted appear to have the shape of an oblique ellipse, regardless of their static safety factor FS_v, the foundation's embedment ratio or the soil's coefficient of friction. More specifically, in the first quadrant the relationship between the horizontal load Q and the moment M appears to be linear, while in the fourth quadrant we can observe a branch of over-strength. It is worth noting at this point that in this study we present one half of the failure envelopes, due to the symmetry that describes them (the first quadrant is symmetrical to the third quadrant and the fourth quadrant to the second one, as shown in *Figure 3.38*).

The linear relationship between the horizontal load and the moment that is observed in the first quadrant of a failure envelope suggests that the two quantities tend to "draw" resistance from similar mechanisms. In the part of the failure envelopes that is located in the first quadrant (as well as the third one due to the aforementioned symmetry) the ratios Q/Q_u and M/M_u are both less than or equal to 1 ($Q/Q_u \leq 1$ and $M/M_u \leq 1$), since the horizontal load and the overturning moment act in the same direction, mobilizing similar mechanisms. Therefore, in this part, the simultaneous presence of the two "same-signed" effects of action deteriorates the foundation's response. As a result, the maximum horizontal load that can be undertaken by the

foundation (as well as the maximum moment) concurs with the system's ultimate capacity (for the points $Q/Q_u =1$ and $M/M_u=0$ and $Q/Q_u =0$ and $M/M_u=1$).

In the fourth quadrant however, this linear relationship is negated. In conflict with the failure envelopes of surface foundation (where the symmetry in the system's response is striking), in deeply embedded foundations we observe a branch of over-strength. More specifically, the branch of over-strength is the locus of points of a failure envelope where we have $Q/Qu \geq 1$ and/or $M/Mu \geq 1$ (i.e. in the fourth and second quadrant of the plane), as the overturning moment becomes counterbalancing to the horizontal force and the system exhibits an enhanced capacity derived from its embedment. However, as we have already specified, the quadrant where the branch of over-strength can be located depends on the position of the load reference point.

At this point, it would be useful to define two more distinctive quantities, the maximum horizontal load Q_{max} and the maximum moment M_{max} assumed by the foundation. Those two quantities differ from their respective ultimate capacities Q_u and M_u that we mentioned above, in that they occur under the simultaneous presence of the other section force and in that there is also an obvious difference in magnitude.

To achieve a more thorough understanding of this specific behavior of deeply embedded foundations (demonstrated through the branch of over-strength and in conflict with the symmetry observed in surface foundations), we should first analyze and comprehend the mechanisms that are developed due to lateral loading, both in surface foundations and caissons.

3.3.4.6. Soil Deformation Mechanisms

The lateral loading of a foundation can be the result either of a seismic excitation (dynamic loading) or of environmental loadings (cyclic loading), especially in the case of offshore structures. For a typical surface foundation we can detect the mechanisms that are mobilized in order to undertake the lateral loading, which in this case are (a) the soil's non-linear response and (b) the geometrical non-linearity of the surface foundation's basis (slippage). On the other hand, in *Figure 3.39* a deeply embedded foundation (caisson) of square plan shape is illustrated, under lateral loading. Furthermore, the distribution of stresses is schematically illustrated along the soil-caisson interface. Although in surface foundations only the base is mobilized to assume the lateral loading, developing normal and shear stresses, that is not the case for deeply embedded foundations, since it is the lateral surfaces that determine the caisson's response.

The following stress distributions are developed along the soil-caisson interfaces : (a) σ_x normal stresses at the transverse planes (lying perpendicular to the lateral loading plane), (b) τ_{xy} shear stresses at the planes lying parallel to the loading plane, (c) τ_{xz} and τ_{yz} shear stresses at the planes lying perpendicular and parallel , respectively, to the loading plane (d) σ_z normal stresses at the base of the foundation. It is worth noting that for caisson foundations the shear stresses that are developed at the caisson's circumference have a predominant role the system's response, providing a considerable resistance to loading.

It is therefore obvious that the response of surface foundations to lateral loading is governed by far less mechanisms compared to those that govern deeply embedded foundations' response and are in fact only a part of caissons' behavior.

FIGURES
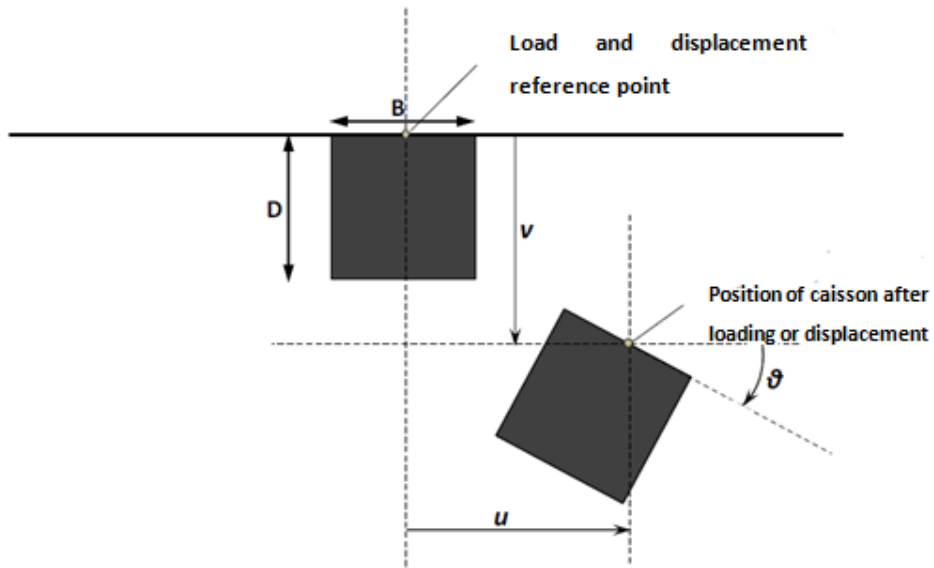
Figure 3.1 *The three "active" degrees of freedom at the load reference point of the caisson:*
a)vertical displacement v b) horizontal displacement u and c) rotation ϑ. The sign convention is
according to Butterfield, Houlsby και Gottardi [1997].
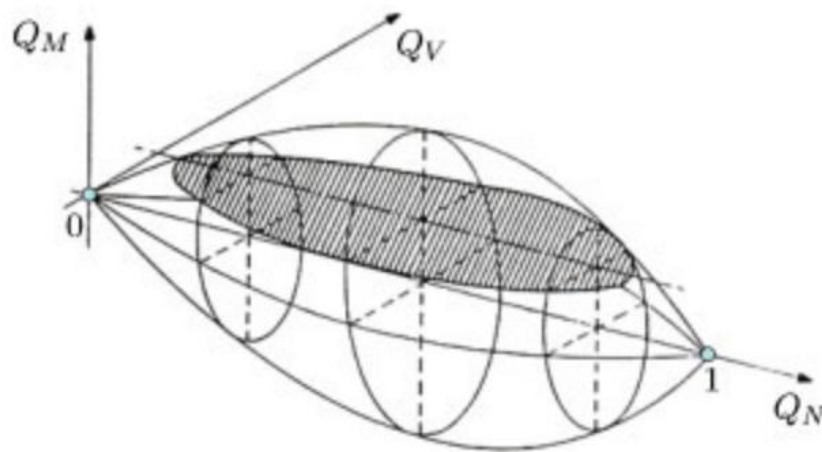
Figure 3.2.a *Rugby-ball shaped yield surface for surface foundations in cohesionless soil*
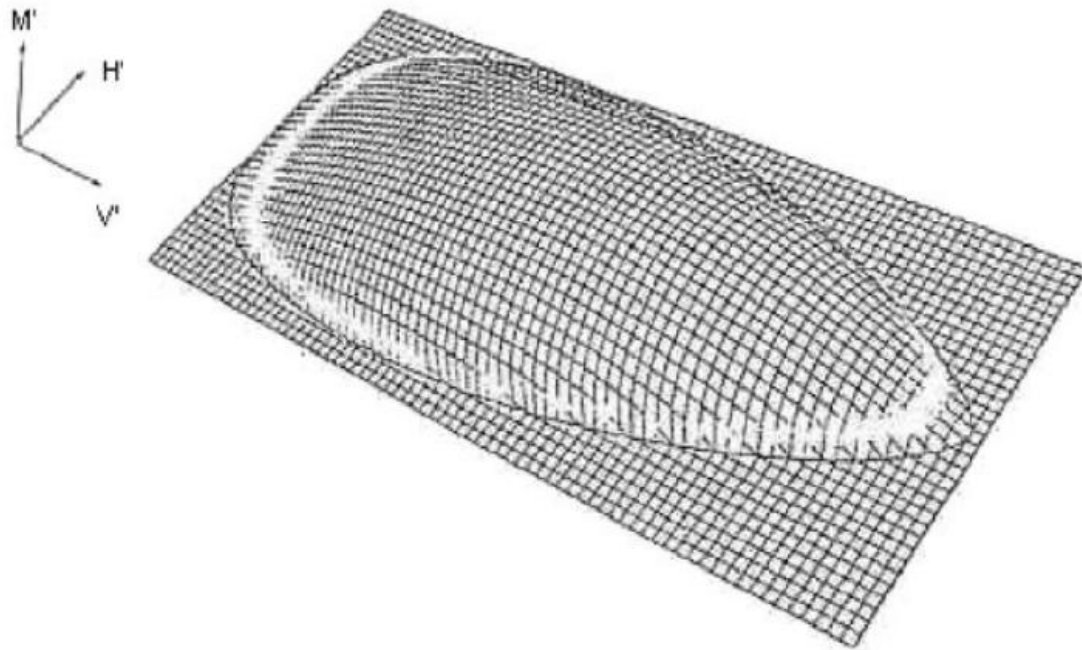
Figure 3.2.b *Yield surface for surface foundations on cohesive soil.*

(a)

(b)

(c)
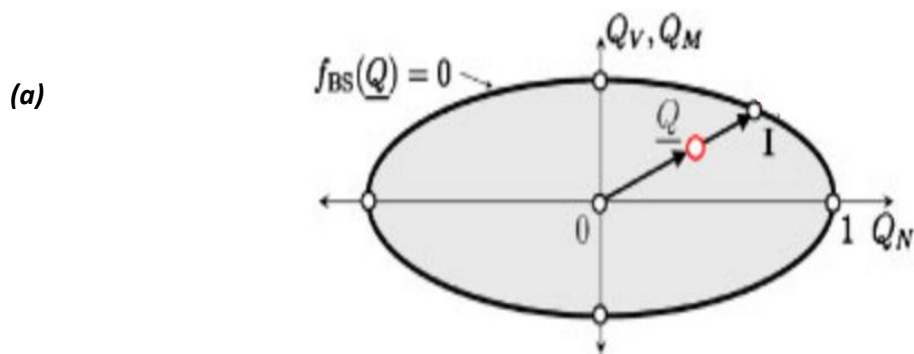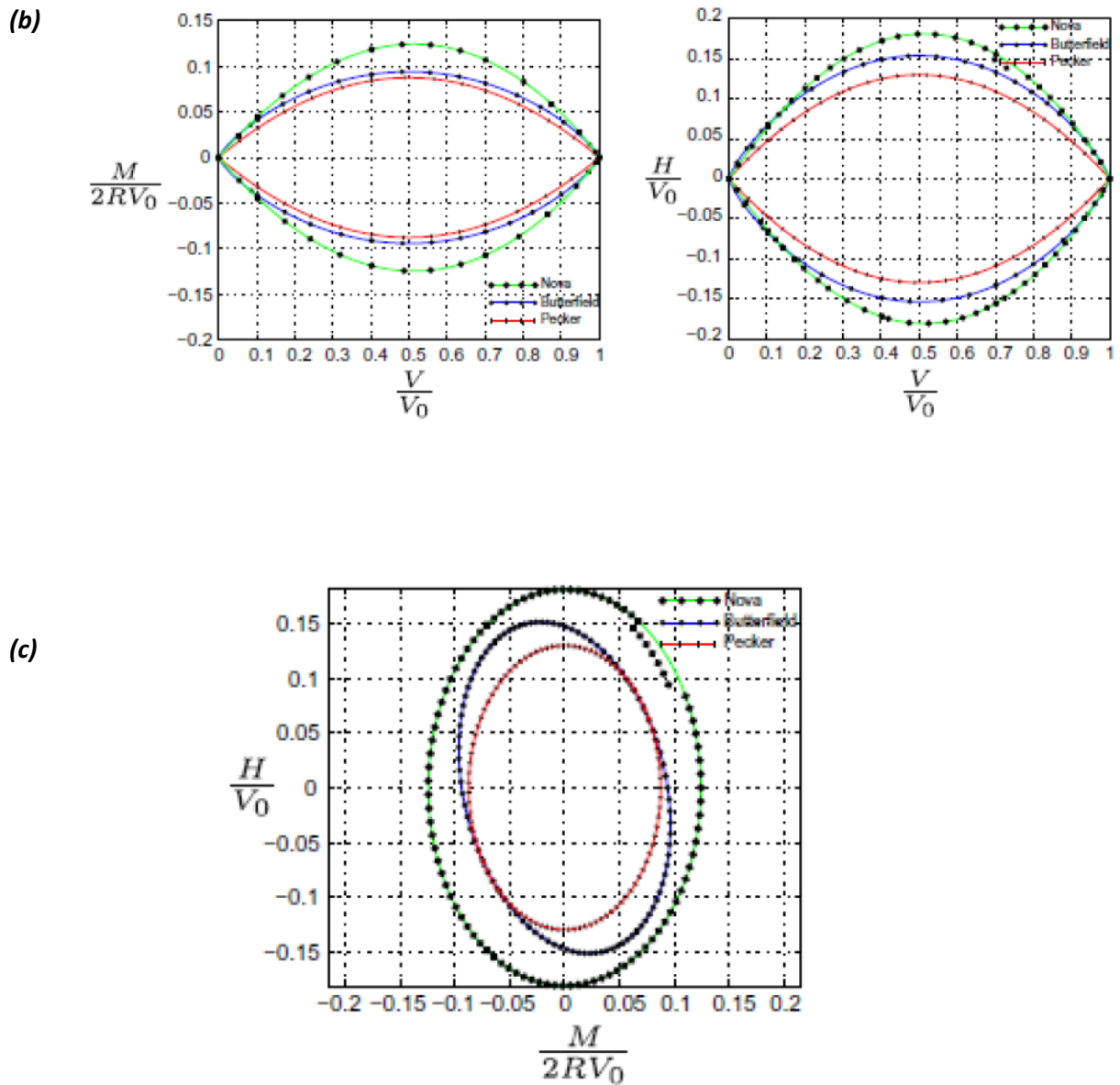
Figure 3.3 *Failure envelopes for surface foundations for three different loading planes : Q-N loading plane , M-N loading plane, Q-M loading plane. Figure **(a)** concerns cohesive soils [Chatzigogos, Figini, Pecker and Salençon 2011] while figures **(b)** and **(c)** concern cohesionless soils [Nova and Montrasio 1991]. In all cases symmetry is observed.*
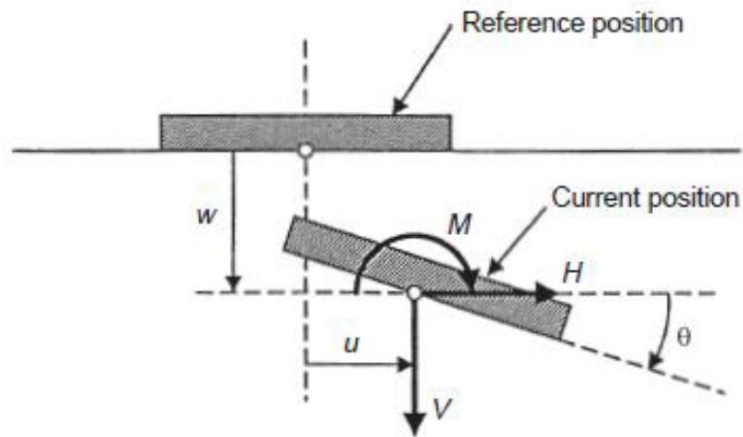
Figure 3.4 *Load-displacement reference point for surface foundations (centre of foundation's base)*
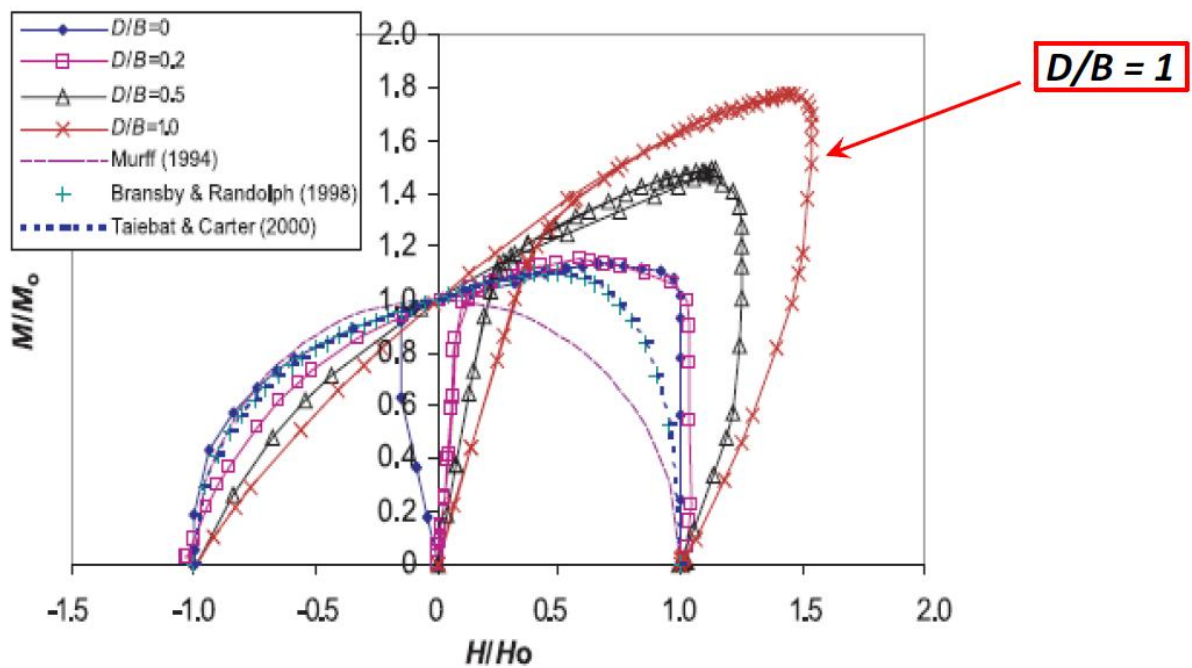
Figure 3.5 *Failure envelopes of deeply embedded foundations in the Q-M plane, where the load-displacement reference point is the centre of the foundation base.*
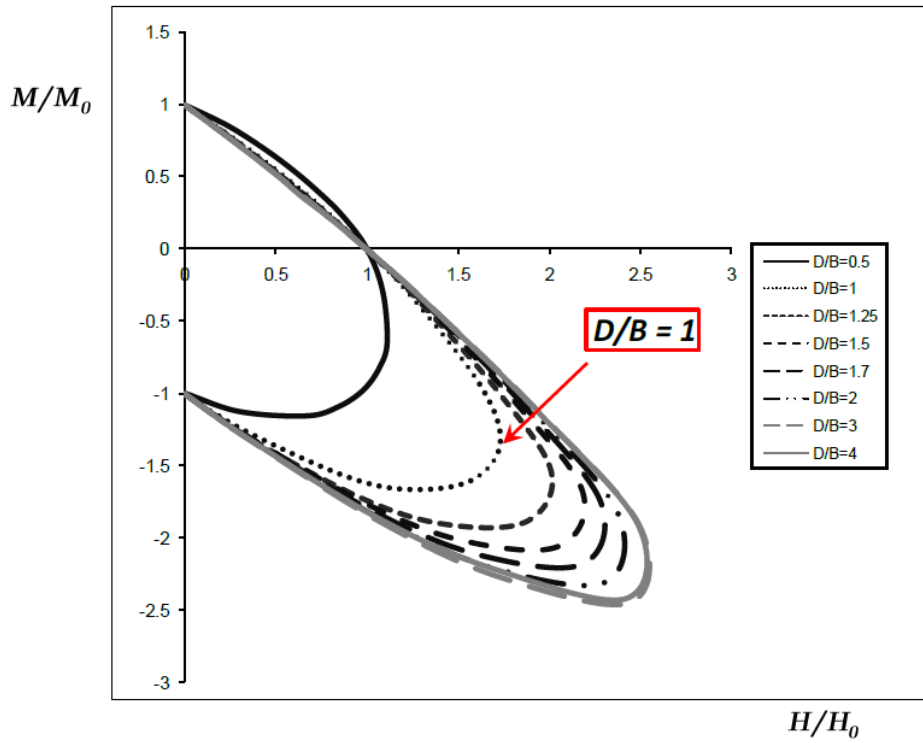
Figure 3.6 *Failure envelopes of deeply embedded foundations in the Q-M plane, where the load-displacement reference point is the centre of the foundation head.*

(a)

(b)
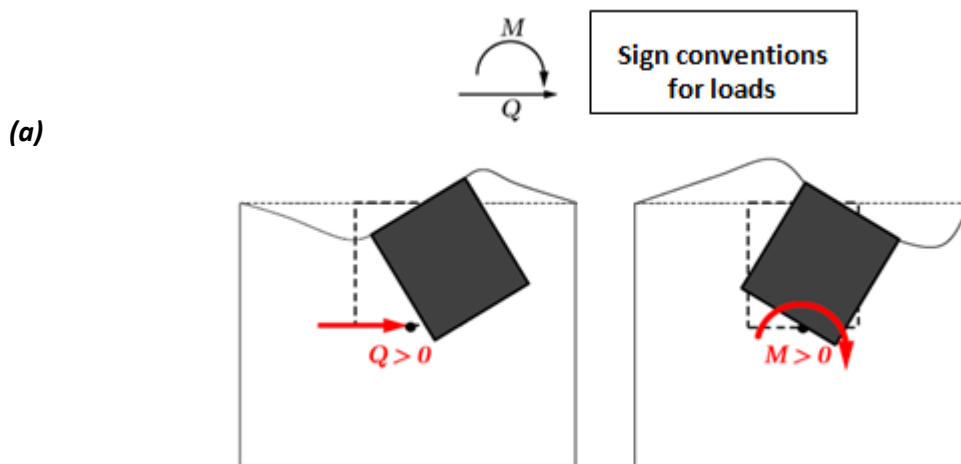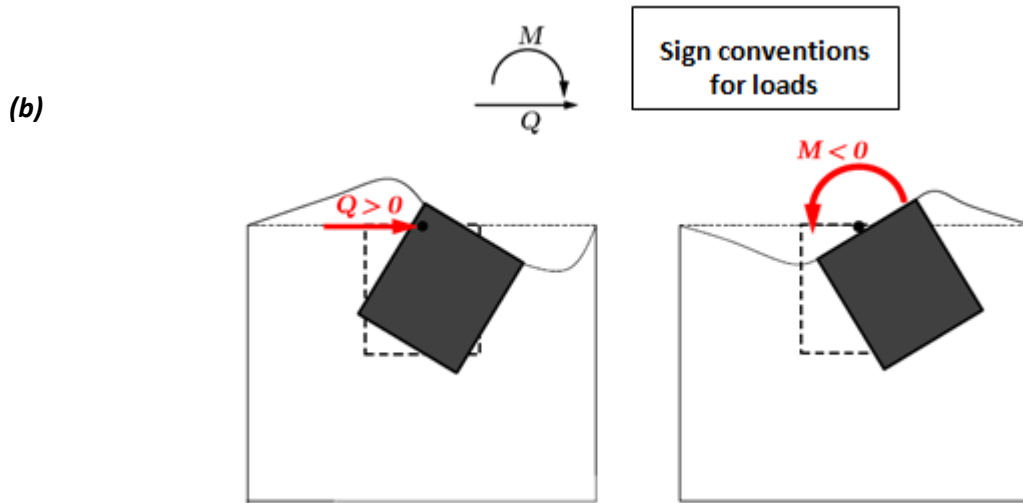
Figure 3.7 *Rough presentation of the soil-caisson system's deformation for loading imposed upon* **(a)** *the caisson's base and* **(b)** *the caisson's head.*
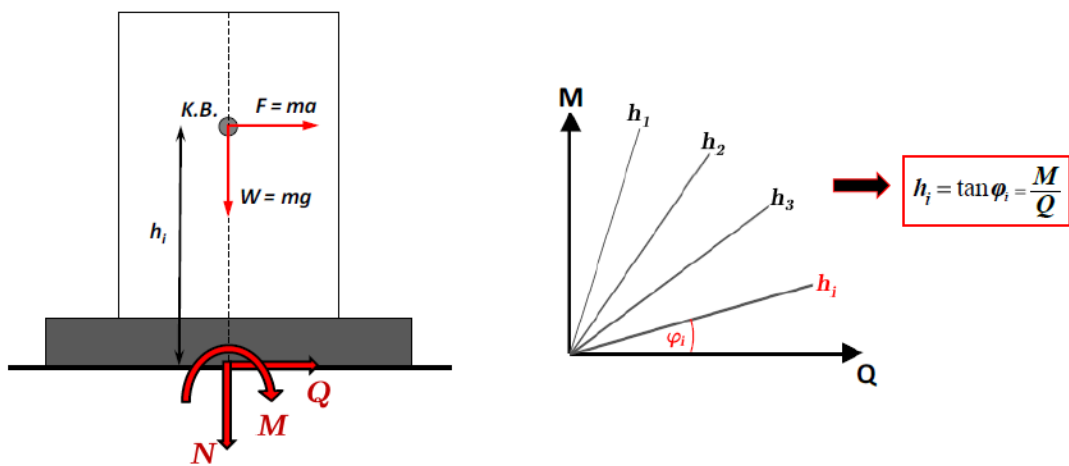
Figure 3.8 *Portrayal of radial loading paths in the loading plane Q-M, as they were defined by Cremer, Pecker και Davenne [2001].*
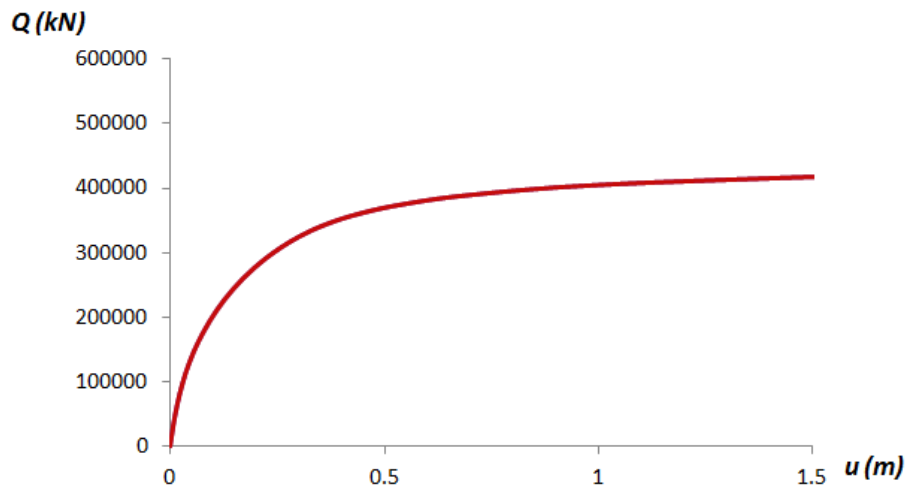
Figure 3.9 *Load-displacement curve-the maximum horizontal load that can be undertaken by the caisson*

(a)

M_u/M_u*

$\chi = 1/FS_v = N/N_u$

(b)

Q_u/Q_u*

$\chi = 1/FS_v = N/N_u$

(c)

M_u/M_u*

$\chi = 1/FS_v = N/N_u$

Q_u/Q_u^*

$\chi = 1/FS_v = N/N_u$
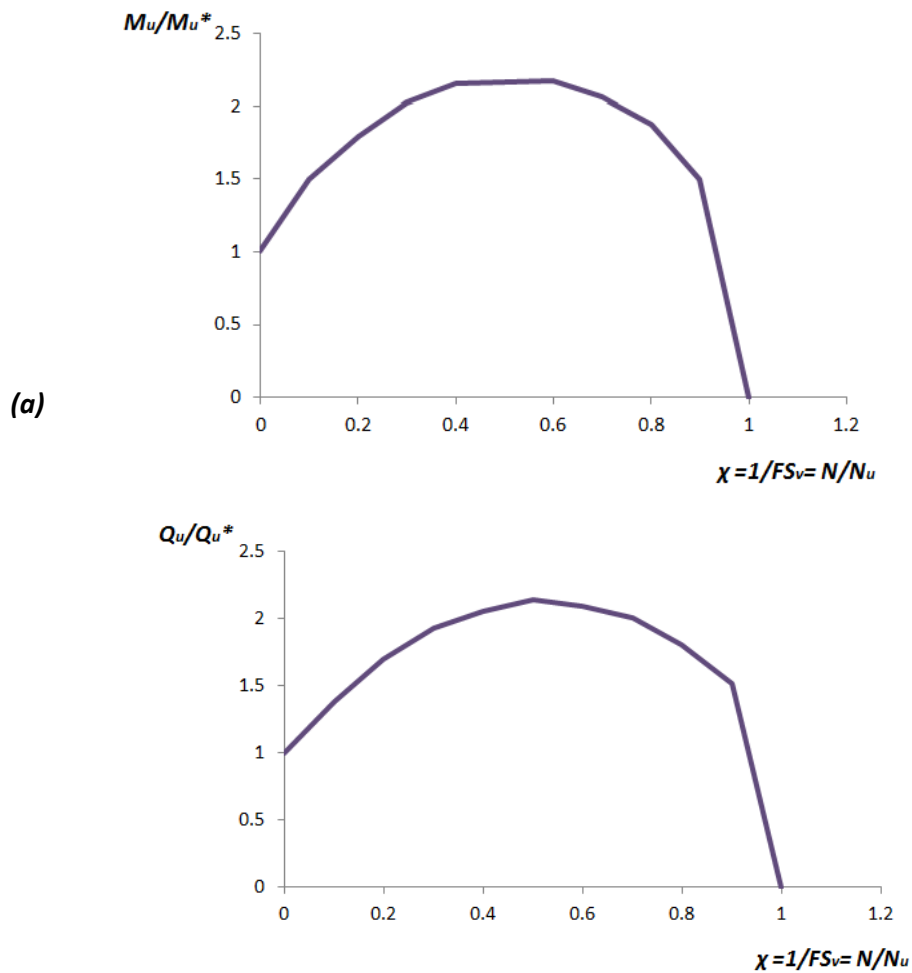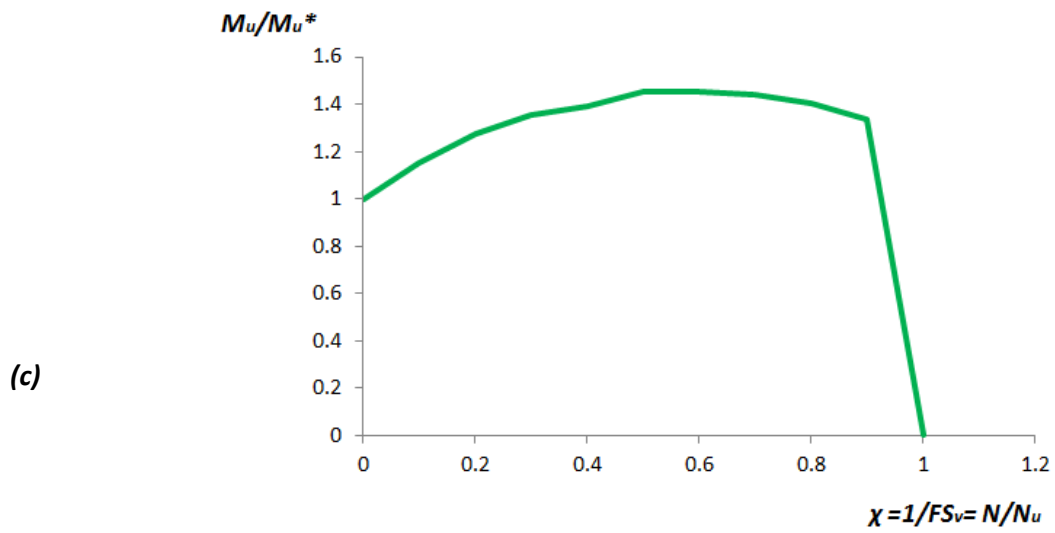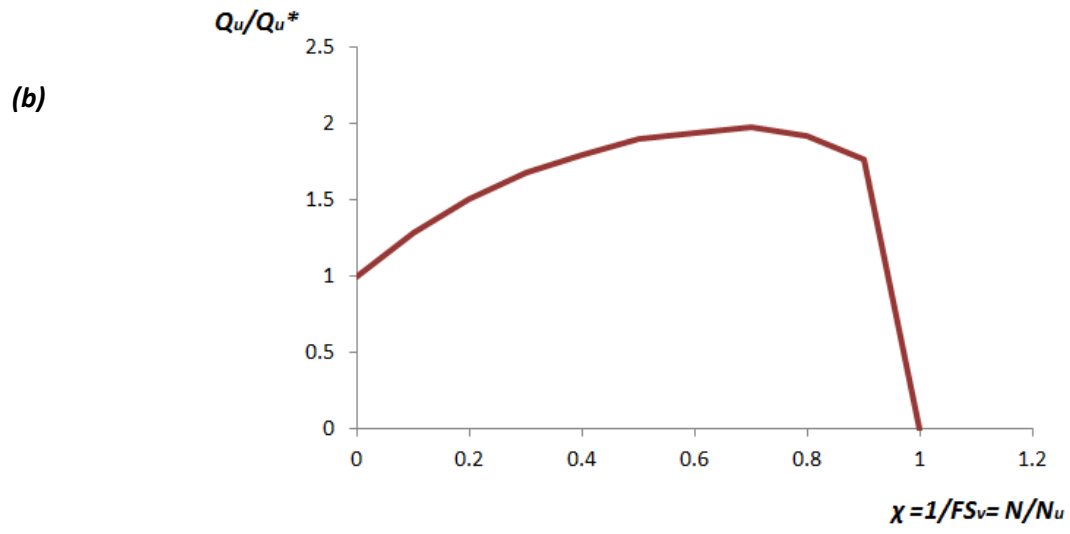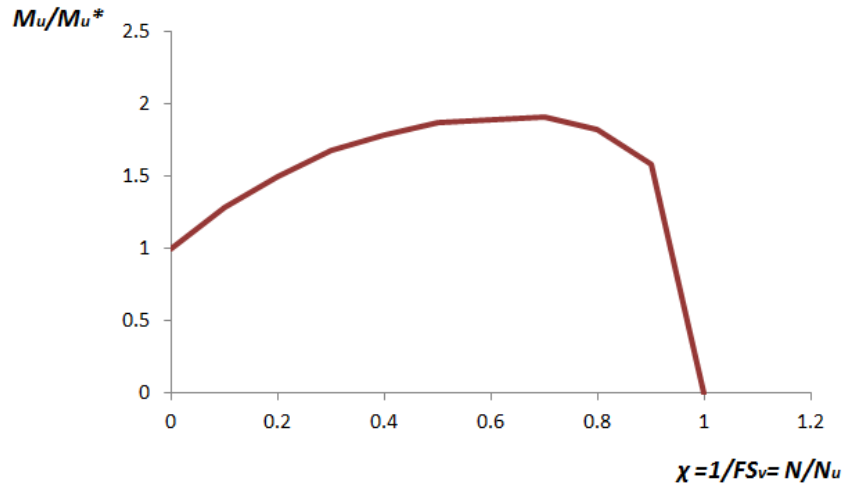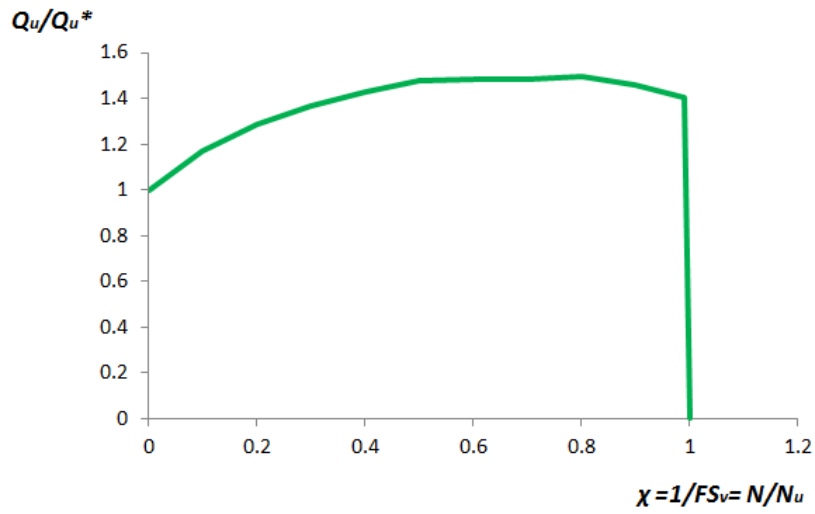
Figure 3.10 *The normalized ultimate horizontal and moment capacities derived from the FE analyses for μ=1 and* **(a)** *D/B=1* **(b)** *D/B=2* **(c)** *D/B=2*

(a)

M_u/M_u^*

D/B=1
D/B=2
D/B=3

$\chi = 1/FS_v = N/N_u$

(b)

Q_u/Q_u^*

Legend: D/B=1, D/B=2, D/B=3

$\chi = 1/FS_v = N/N_u$
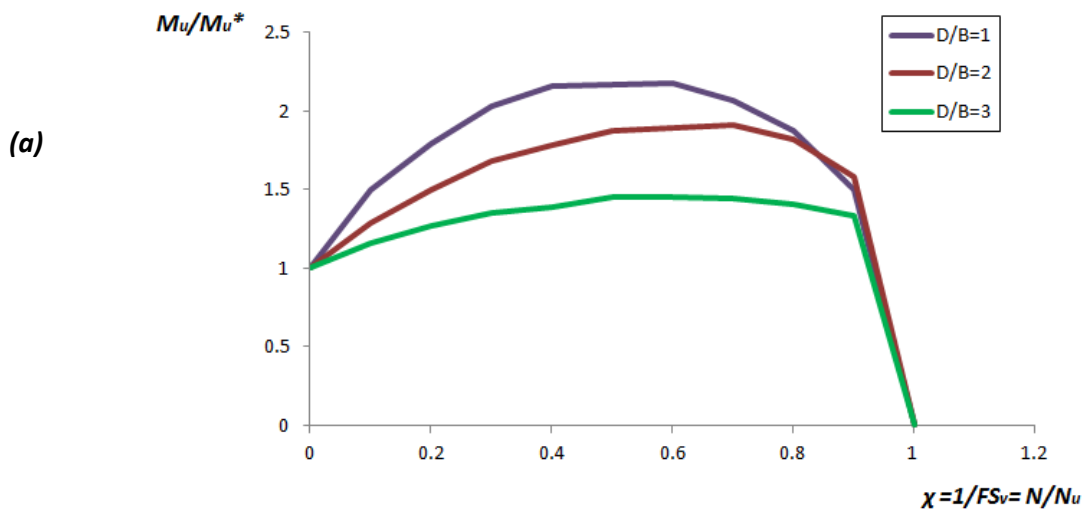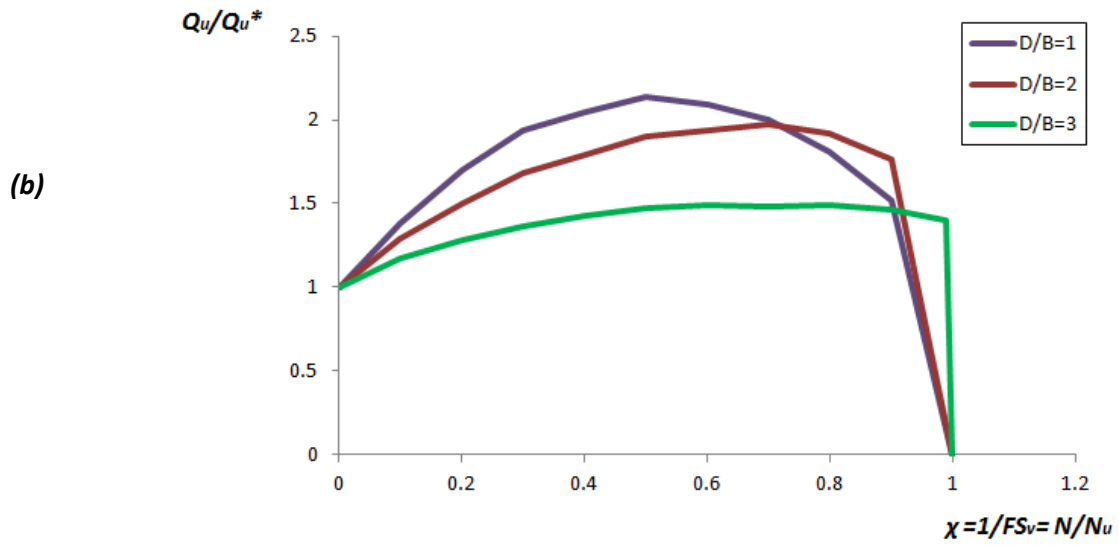
Figure 3.11 *Comparison of the normalized ultimate (α) moment and (b) horizontal capacities for μ=1 and D/B=1, 2 and 3.*

(a)

M_u/M_u^*

$\chi = 1/FS_v = N/N_u$

(b)
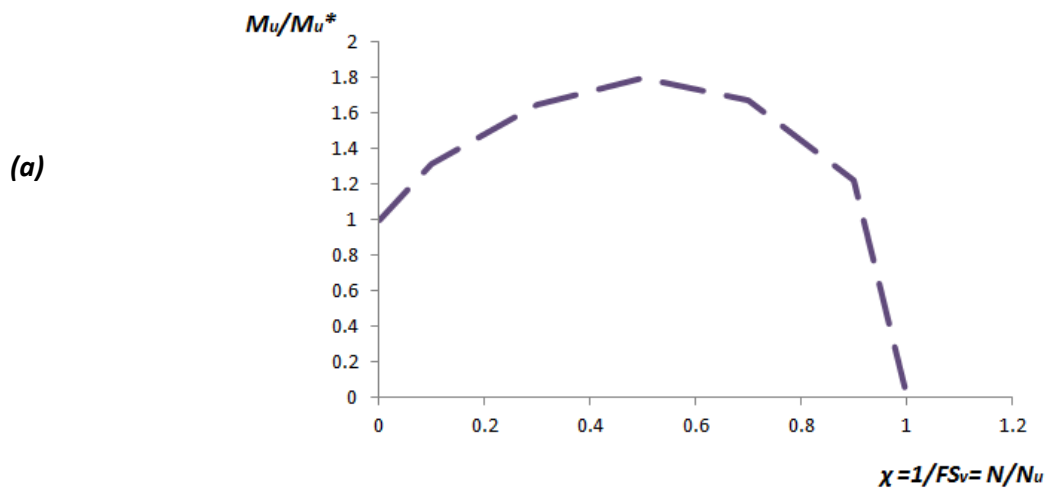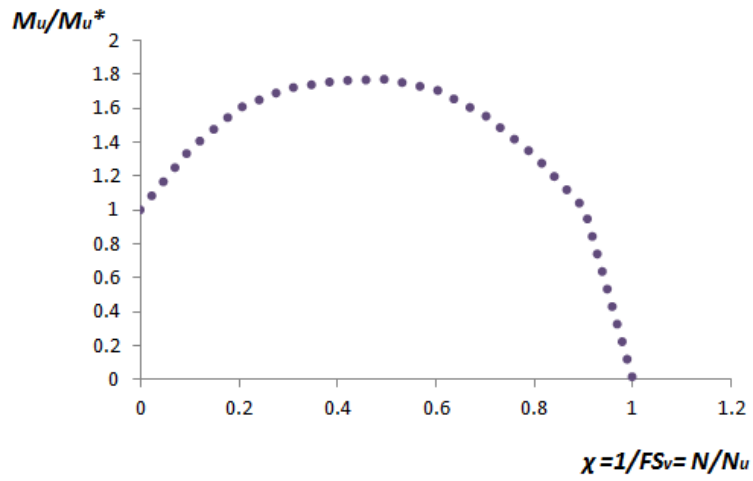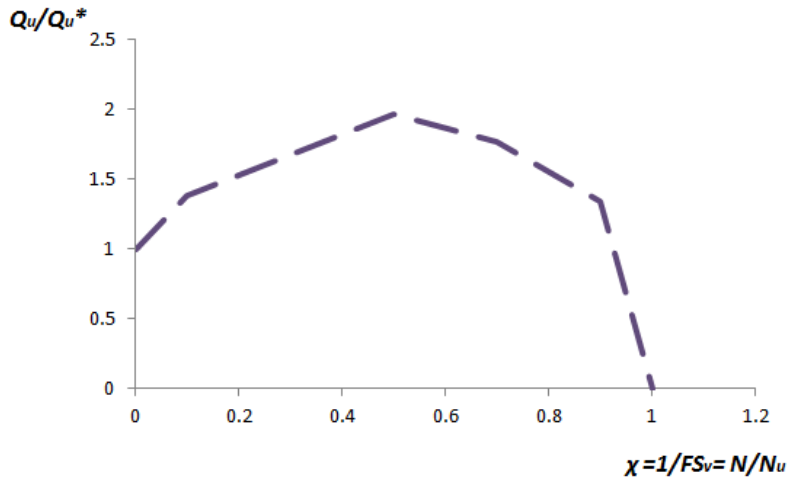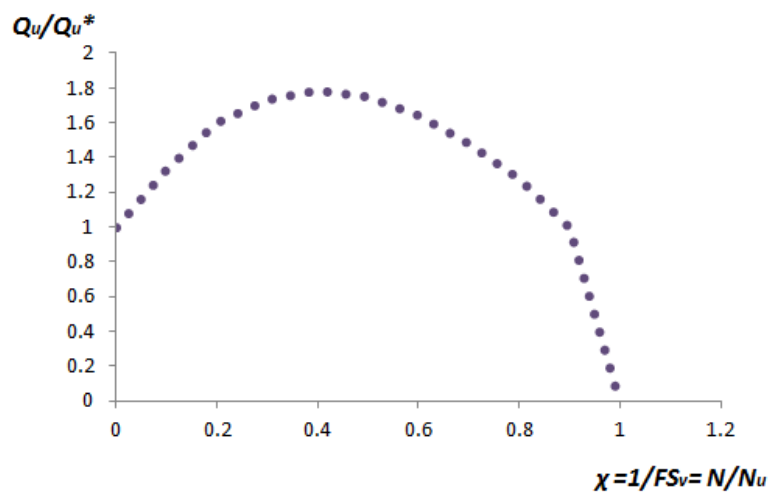
Figure 3.12 *The normalized ultimate horizontal and moment capacities derived from the FE analyses for D/B=1 and* **(a)** *μ=0.5* **(b)** *μ=0.3*
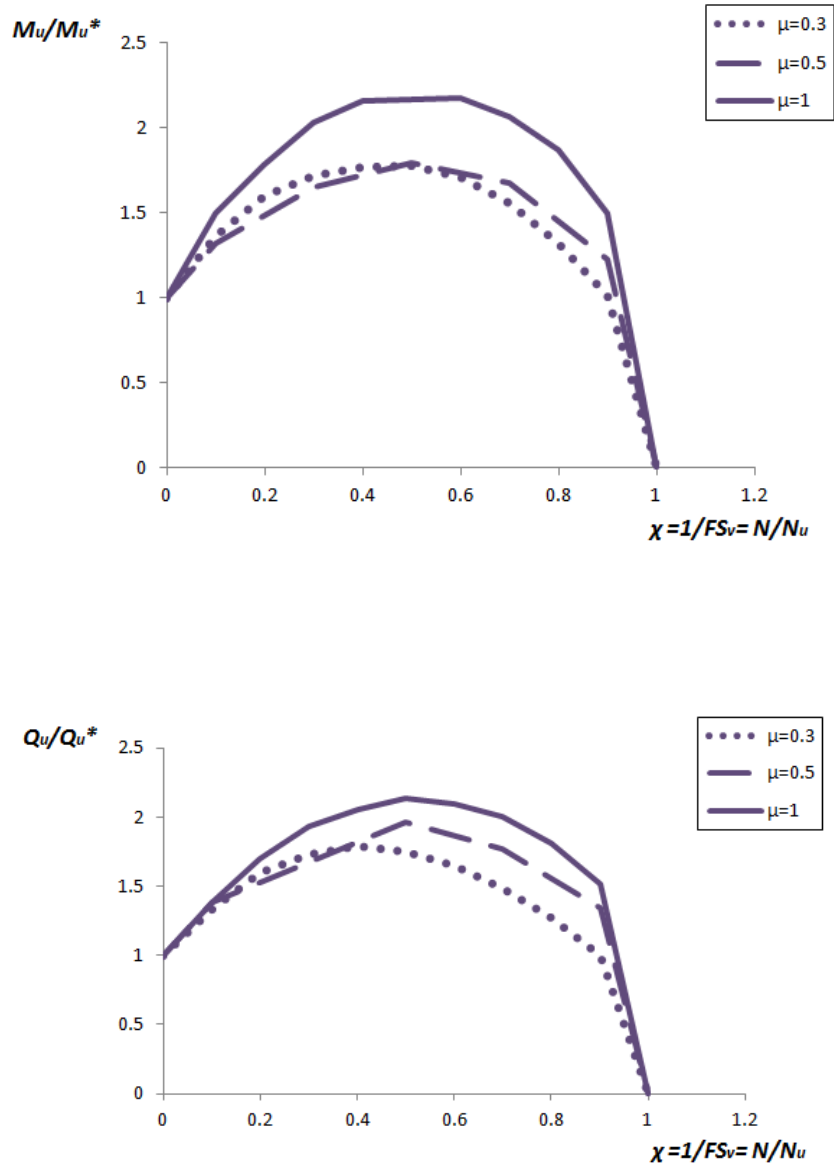
Figure 3.13 *Comparison of the normalized ultimate* **(α)** *moment and* **(b)** *horizontal capacities for D/B=1 and μ=1, 0.5 and 0.3.*

(a)

(b)

$Q_u/Q_u{*}$

$\chi = 1/FS_v = N/N_u$
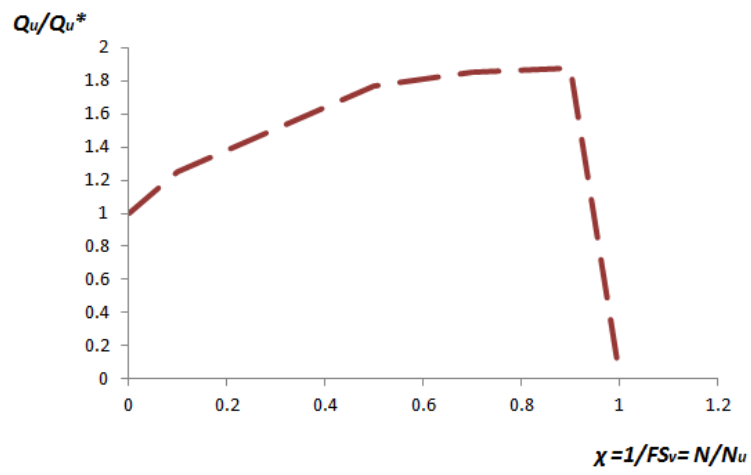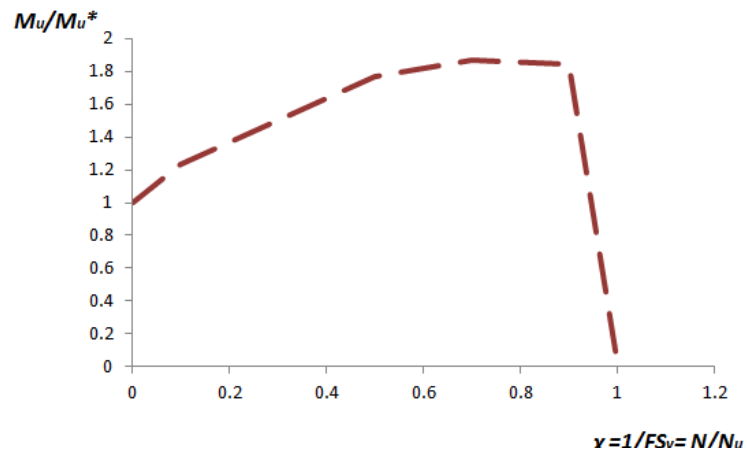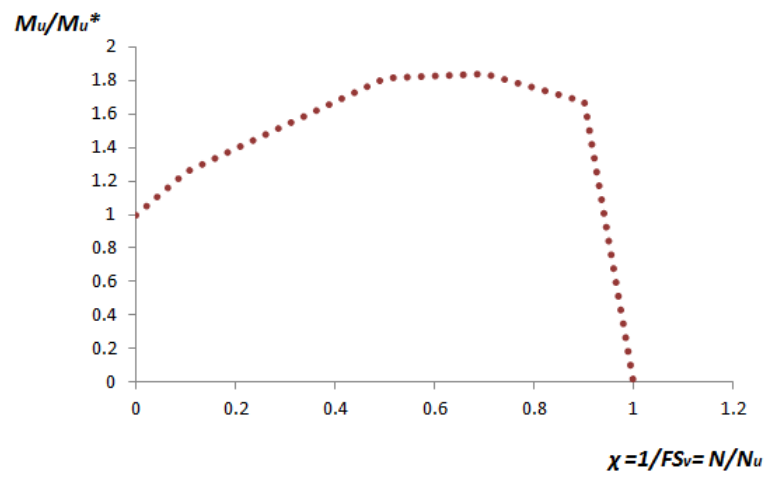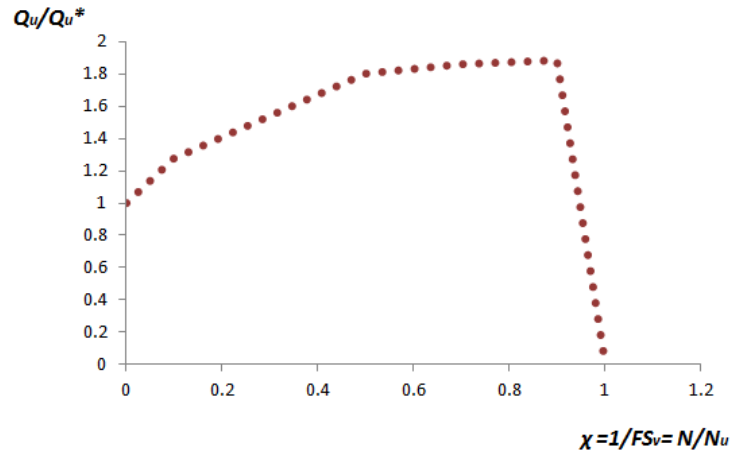
Figure 3.14 *The normalized ultimate horizontal and moment capacities derived from the FE analyses for D/B=2 and **(a)** μ=0.5 **(b)** μ=0.3*

(a)

$M_u/M_u{*}$

μ=0.3
μ=0.5
μ=1

$\chi = 1/FS_v = N/N_u$

(b)

$Q_u/Q_u{*}$

μ=0.3
μ=0.5
μ=1

$\chi = 1/FS_v = N/N_u$
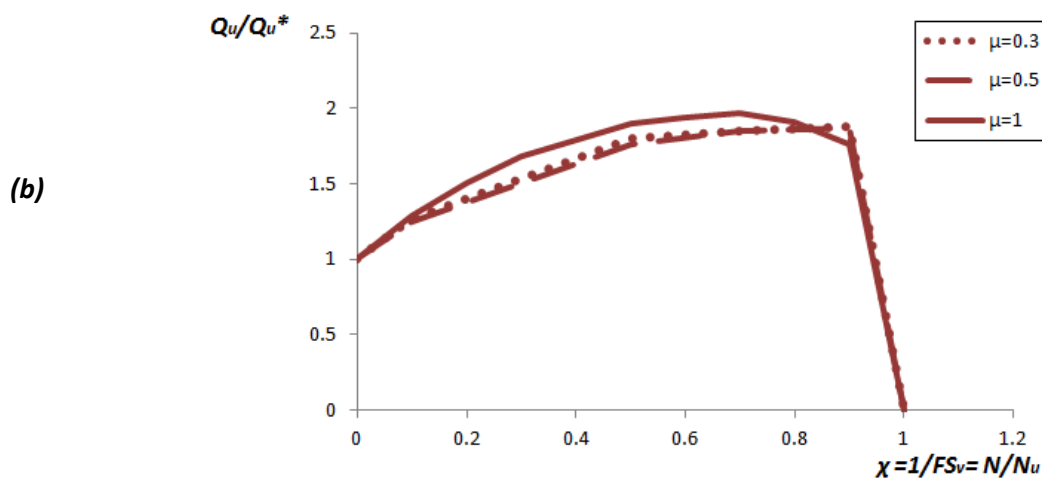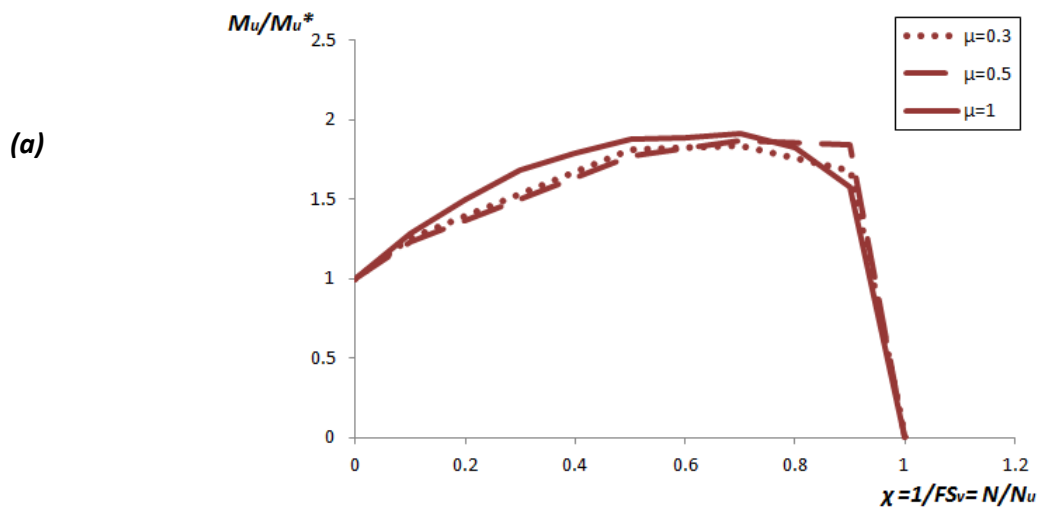
Figure 3.15 *Comparison of the normalized ultimate* **(α)** *moment and* **(b)** *horizontal capacities for D/B=2 and μ=1, 0.5 and 0.3.*

(a)

(b)
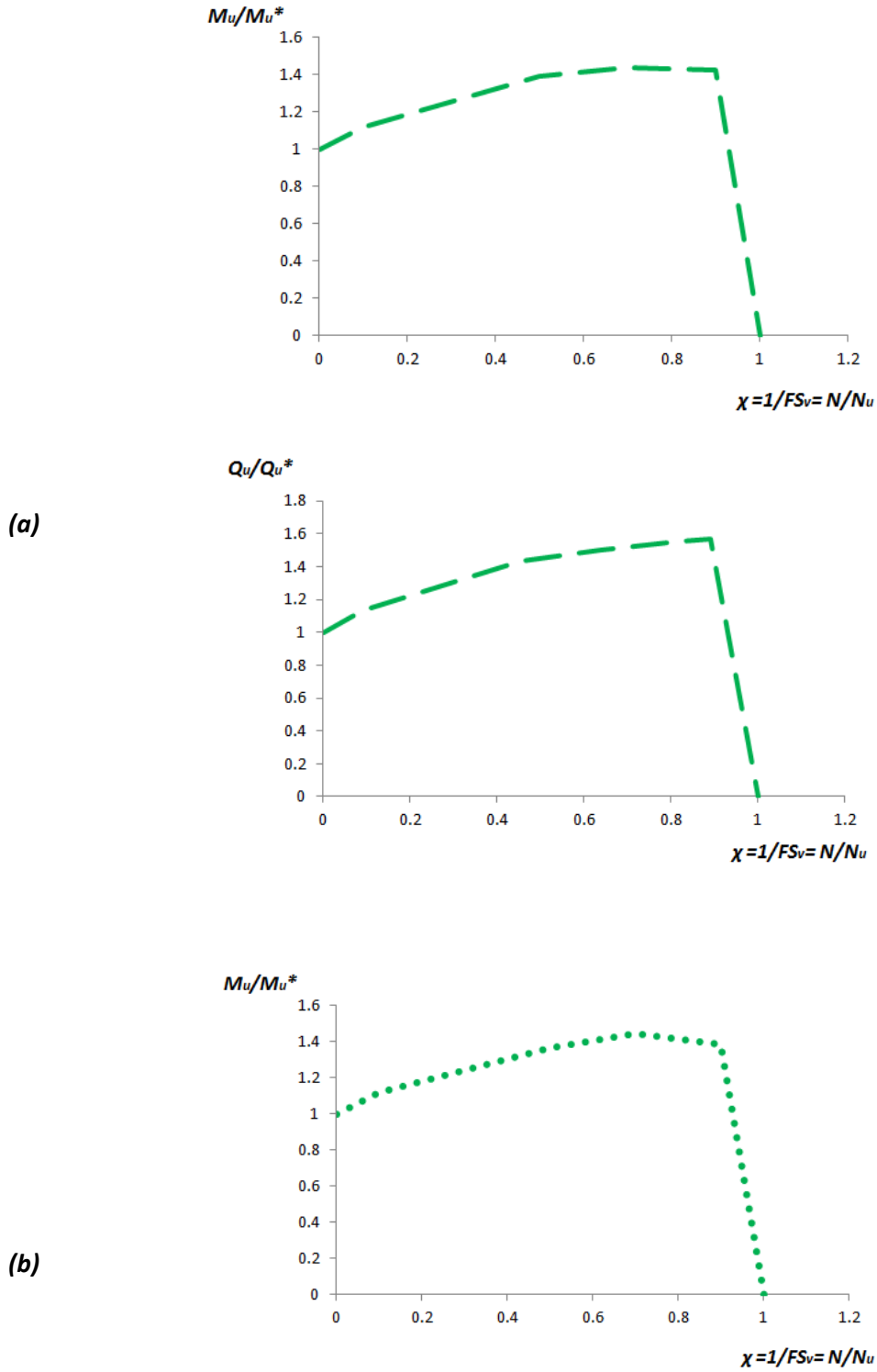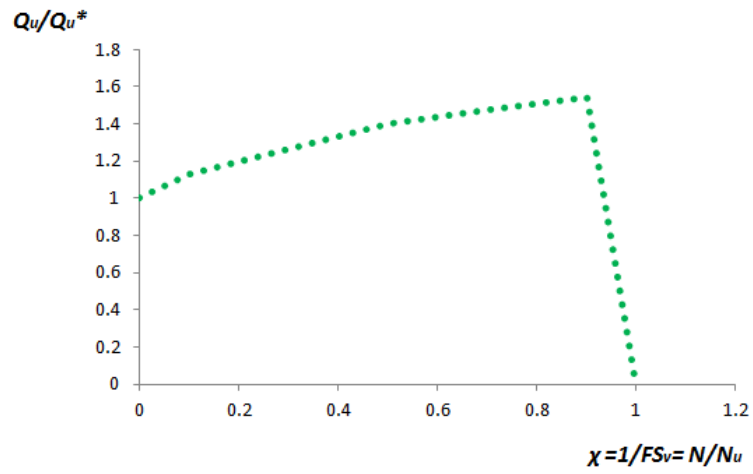
Figure 3.16 *The normalized ultimate horizontal and moment capacities derived from the FE analyses for D/B=3 and* **(a)** *μ=0.5* **(b)** *μ=0.3*

(a)

(b)
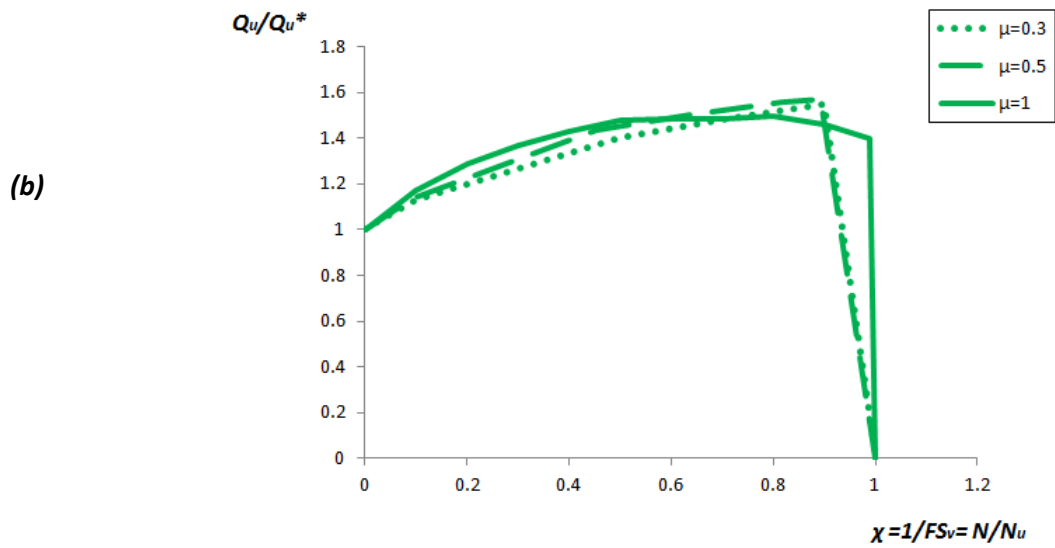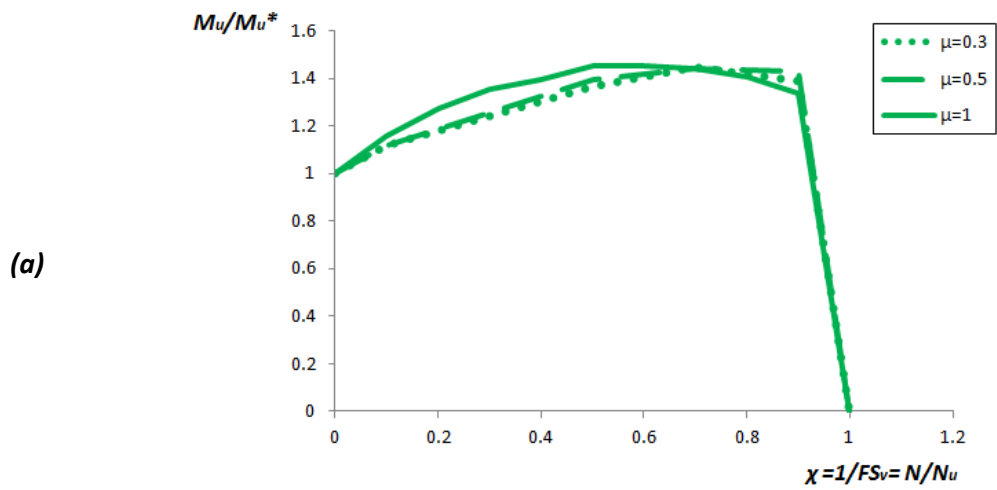
Figure 3.17 *Comparison of the normalized ultimate (**α**) moment and (**b**) horizontal capacities for D/B=3 and μ=1, 0.5 and 0.3.*
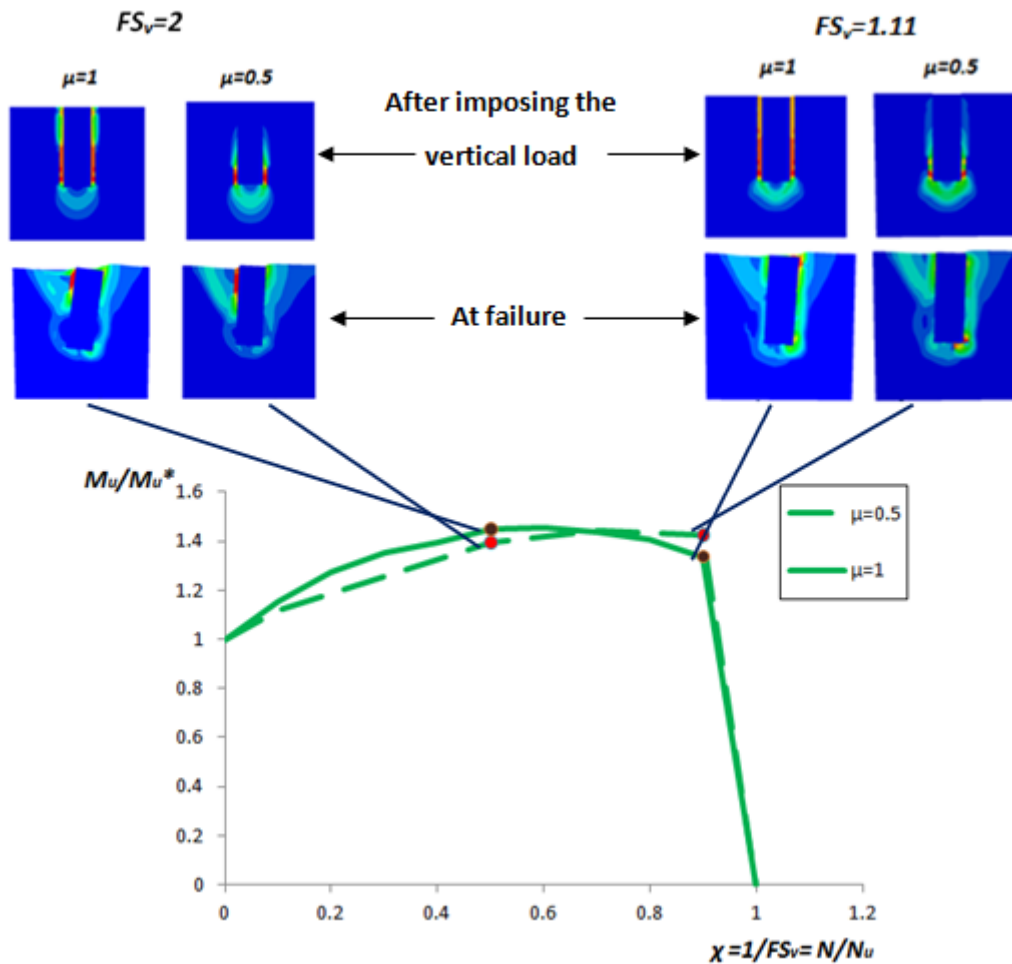
Figure 3.18 *Comparison of snapshots of plastic strain magnitude contours both at the moment of failure and at the moment after imposing the vertical load, for safety factors $FS_v=2$ and $FS_v=1.11$ and for a rough (μ=1) and a smooth (μ=0.5) interface*

(a)

(b)

(c)

(d)

(e)

(f)

(g)

(h)

(i)
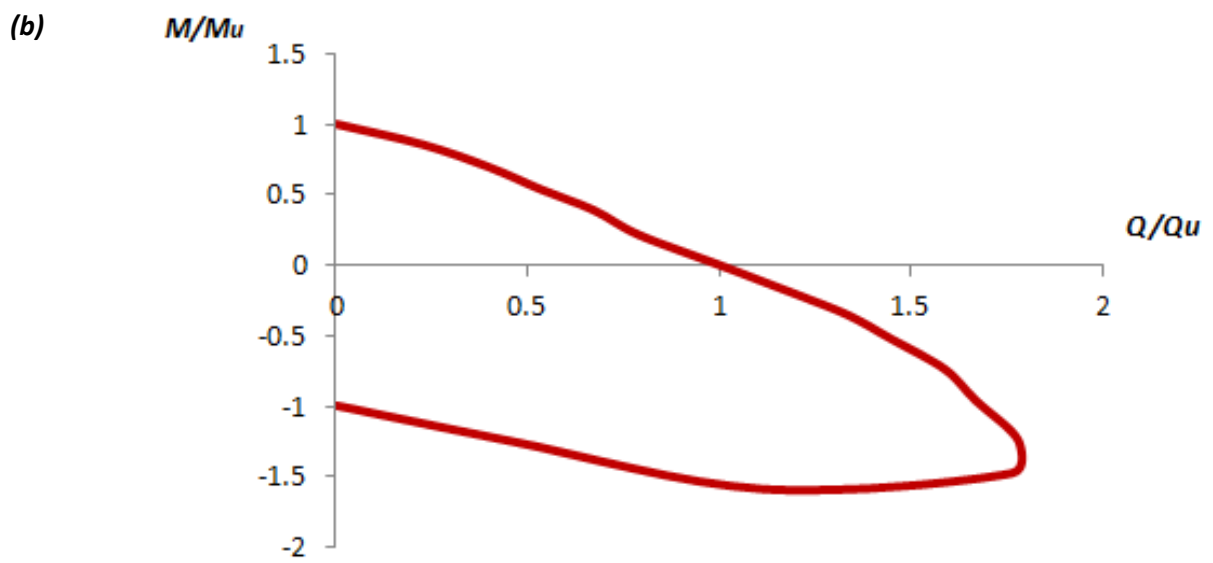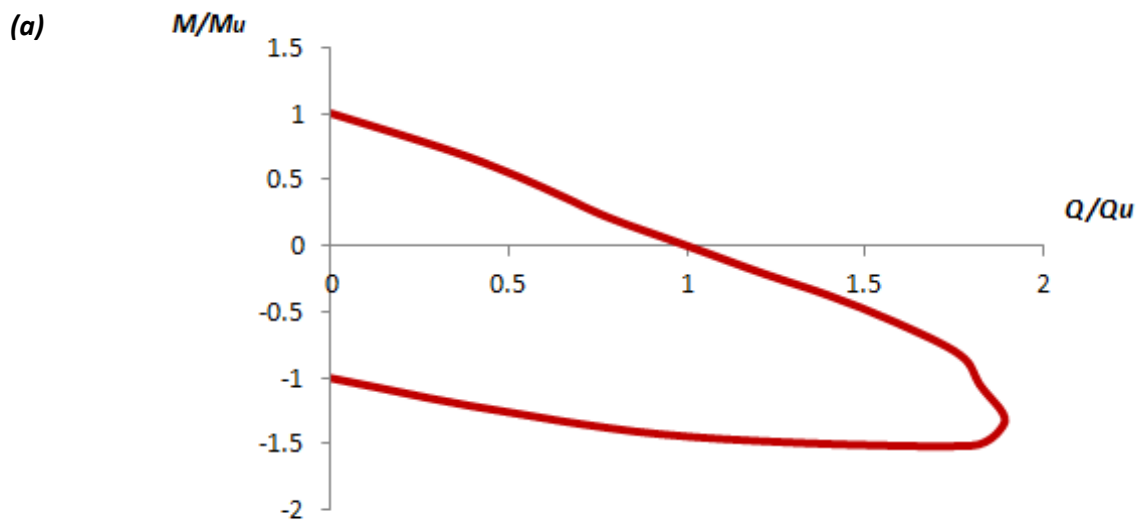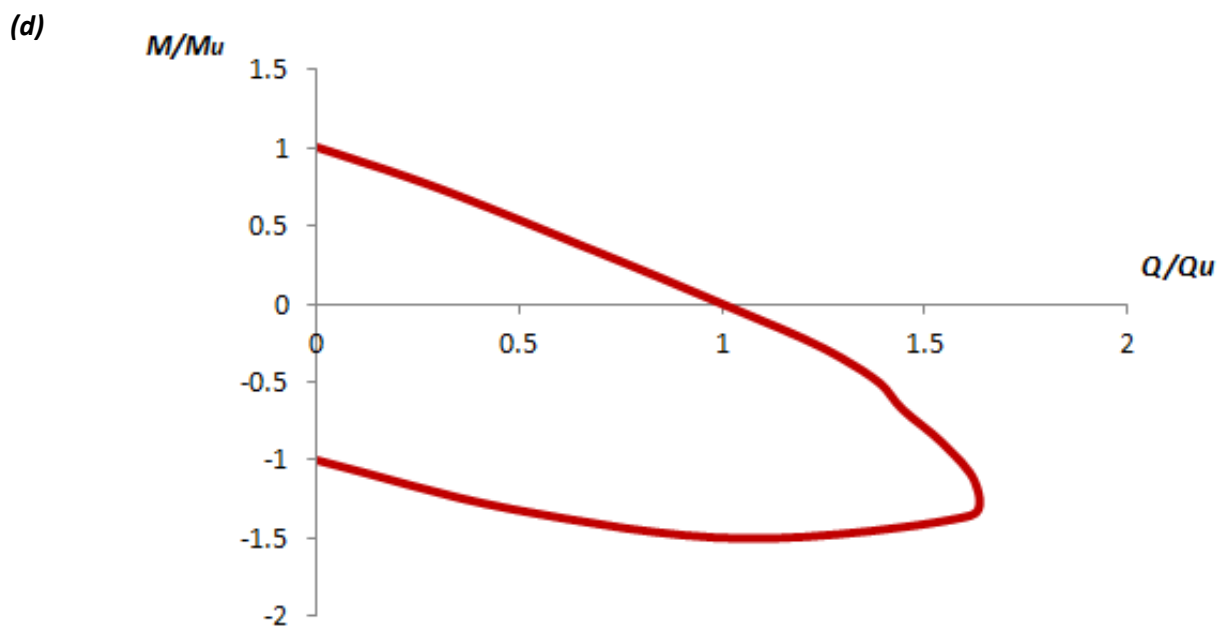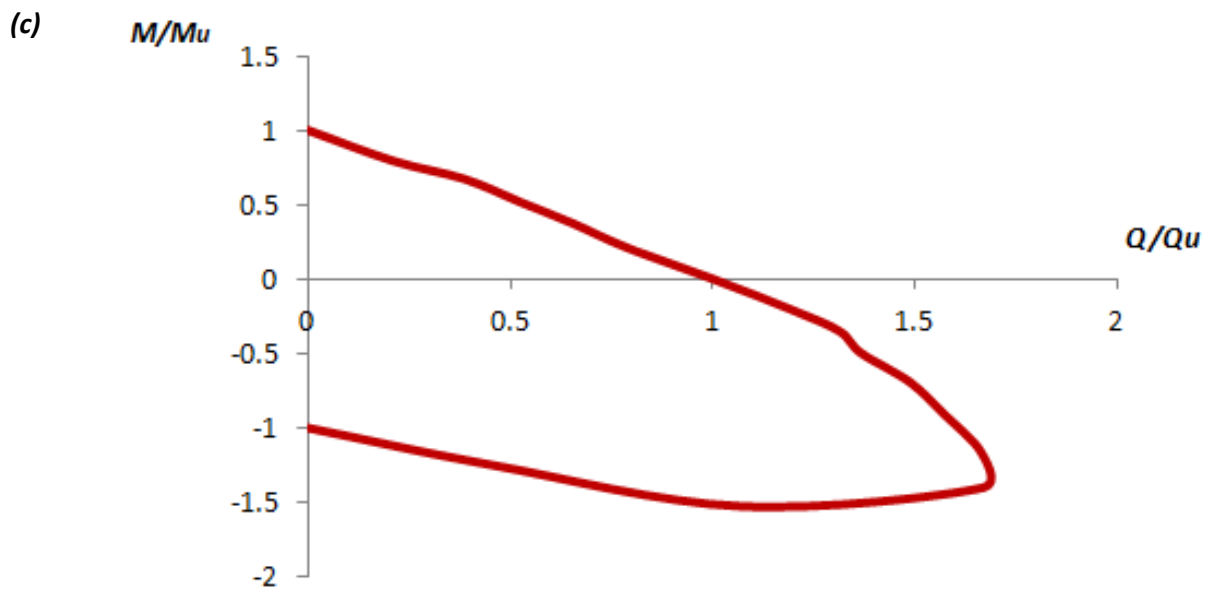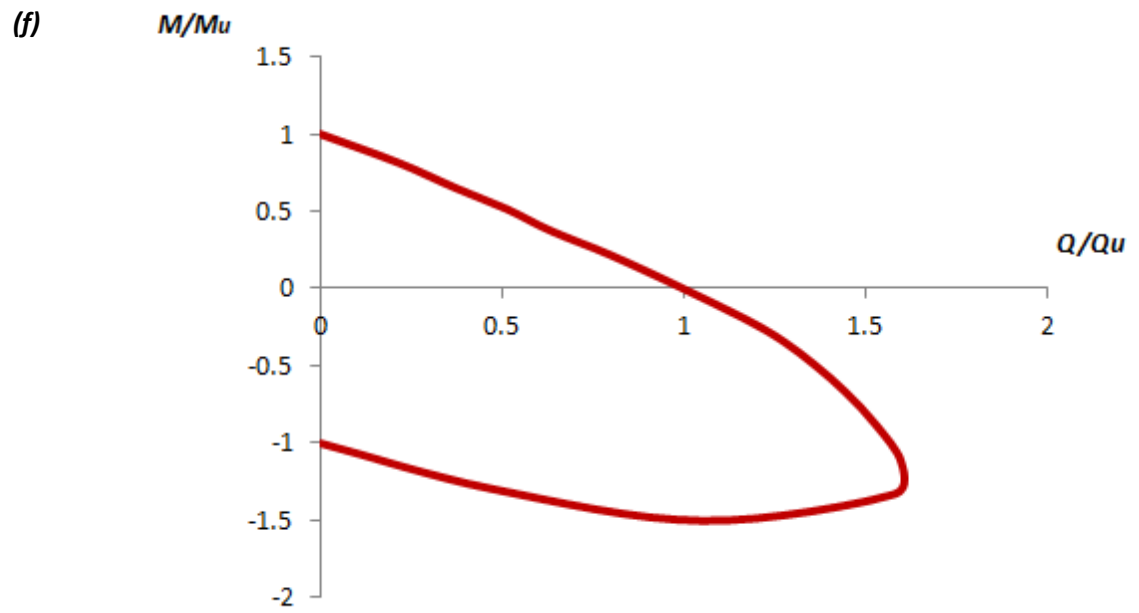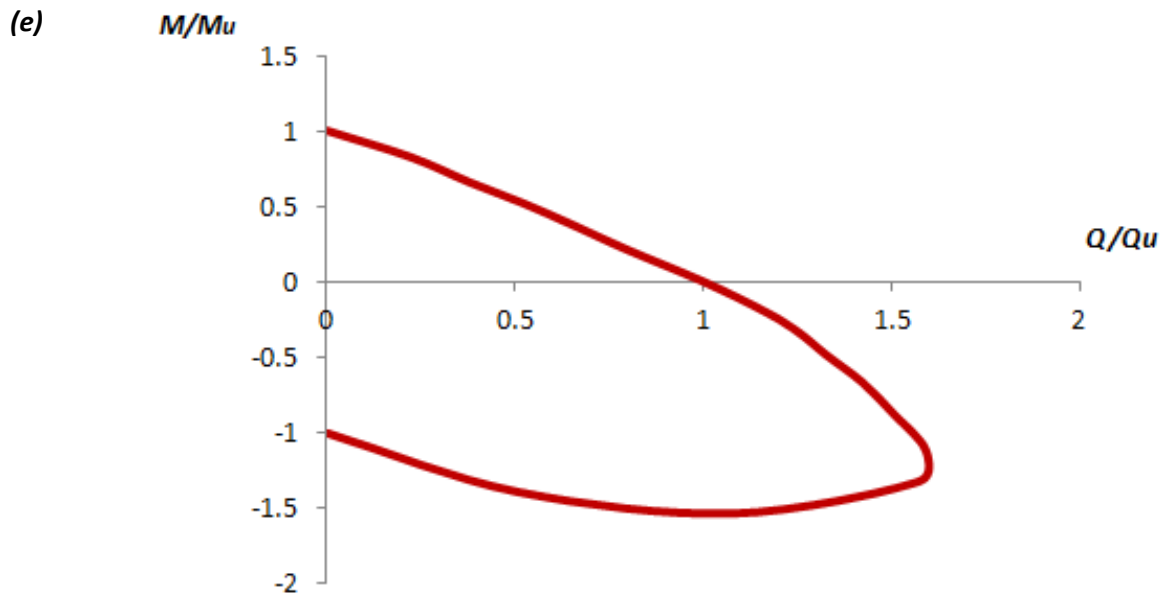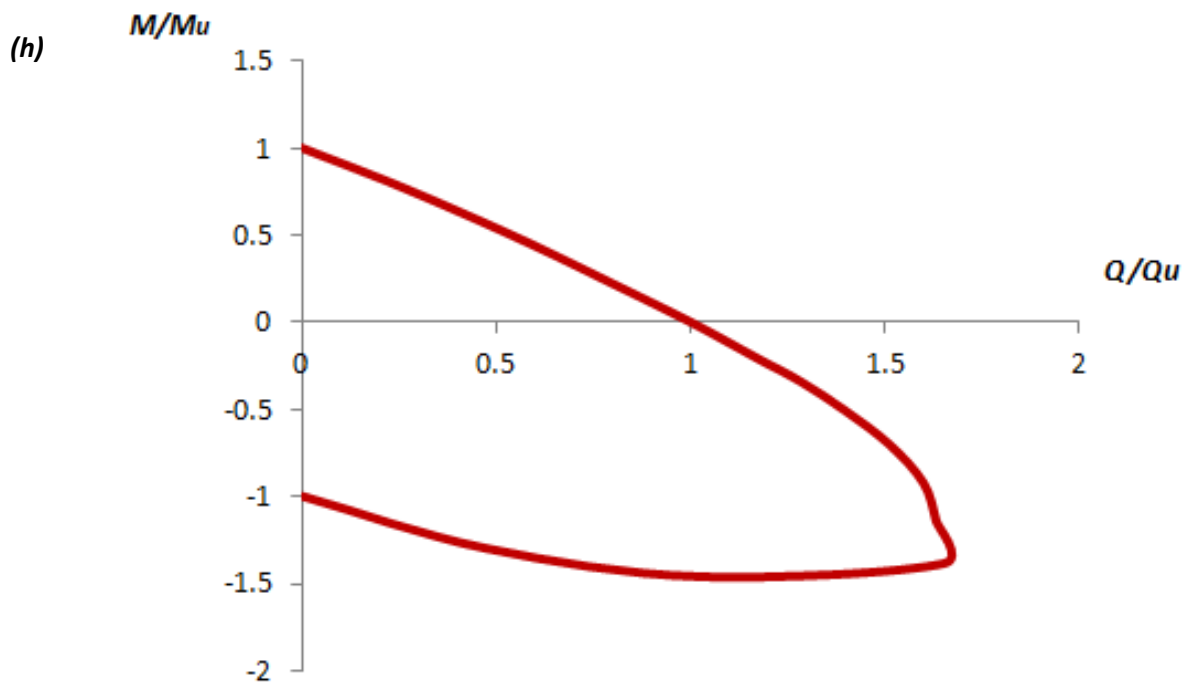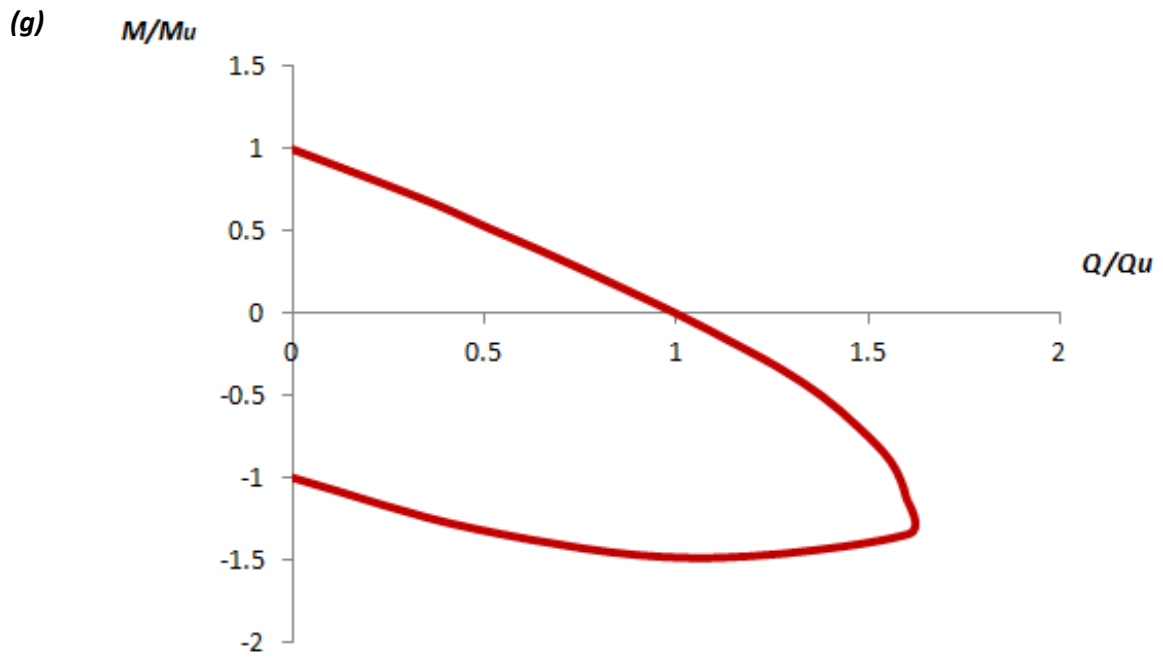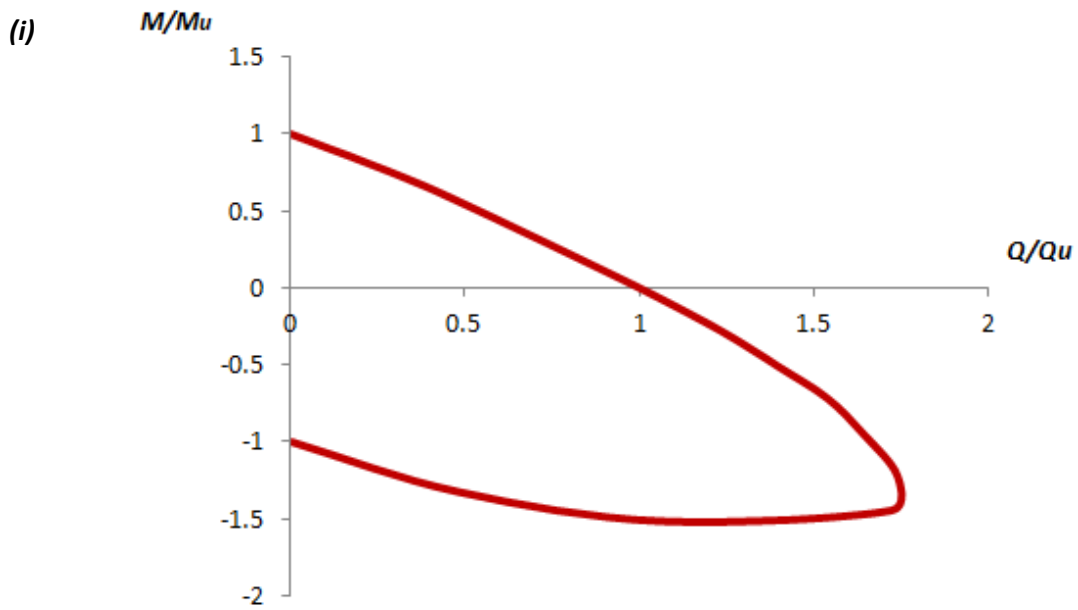

Figure 3.19 *Failure Envelopes of deeply embedded foundations for coefficient of friction μ=1 , embedment ratio D/B=1 and factors of safety **(a)** FS$_v$=10 **(b)** FS$_v$=5 **(c)** FS$_v$=3.33 **(d)** FS$_v$=2.5 **(e)** FS$_v$=5 **(f)** FS$_v$=1.67 **(g)** FS$_v$=1.43 **(h)** FS$_v$=1.25 and **(i)** FS$_v$=1.11*
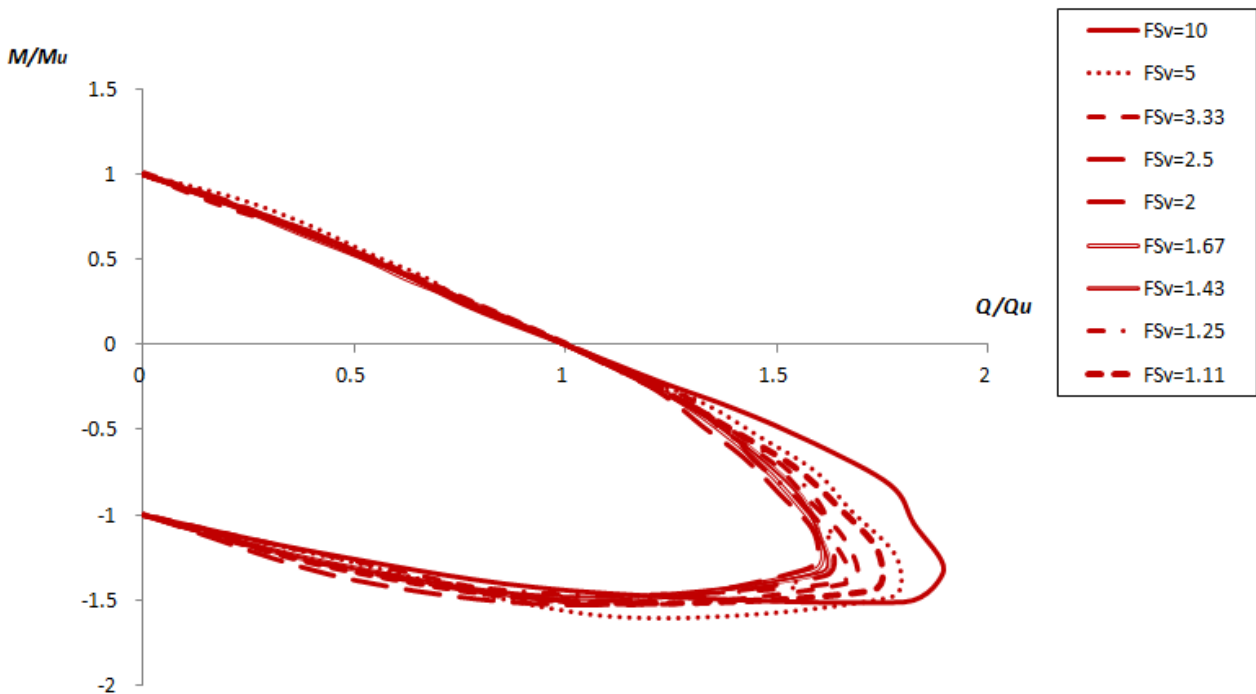
Figure 3.20 Comparison of failure envelopes of deeply embedded foundations for coefficient of friction μ=1 , embedment ratio D/B=1 and every examined factor of safety

(a)


(b)

(c)

(d)

(e)

(f)
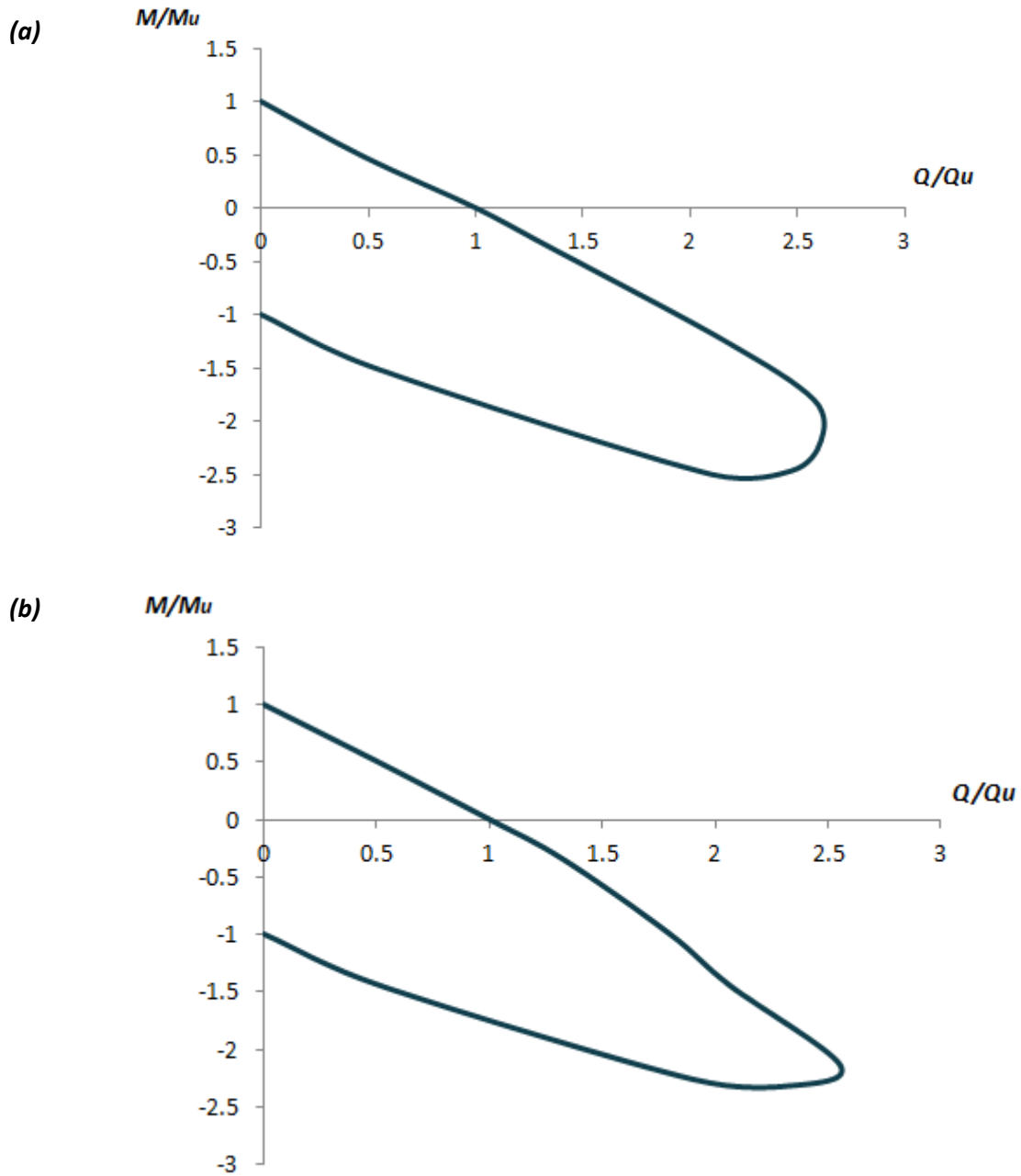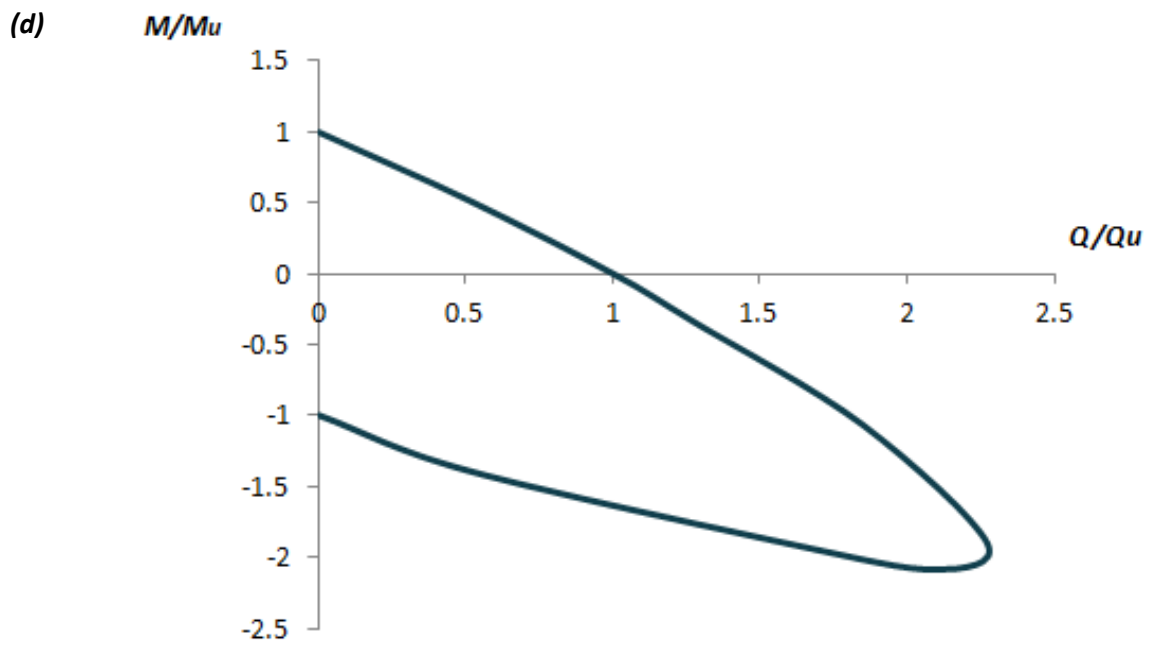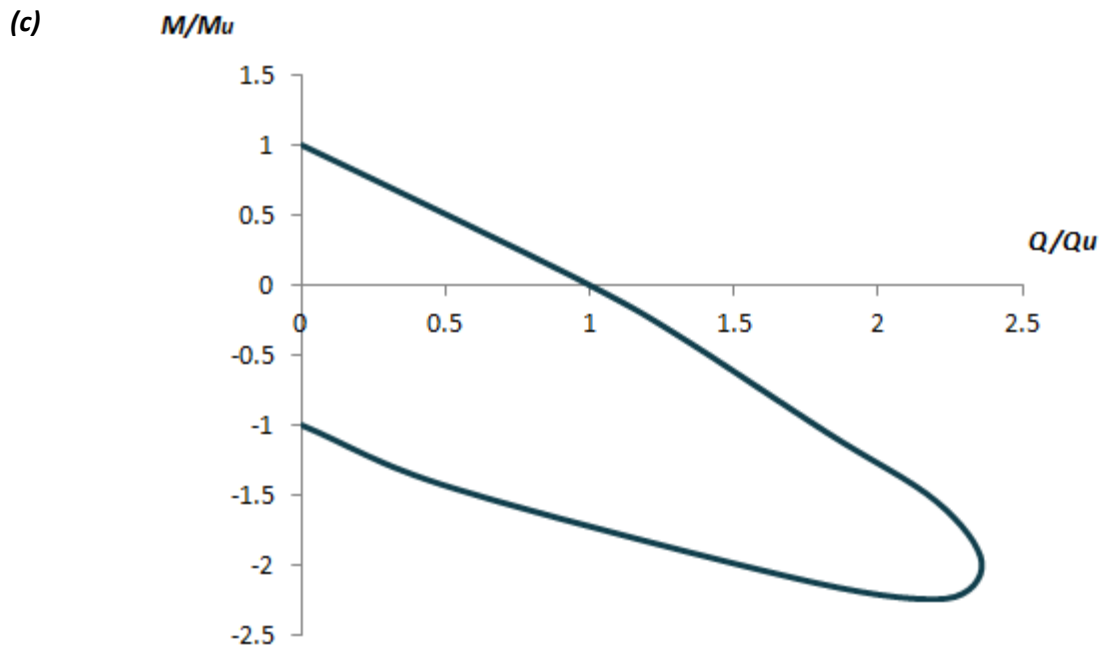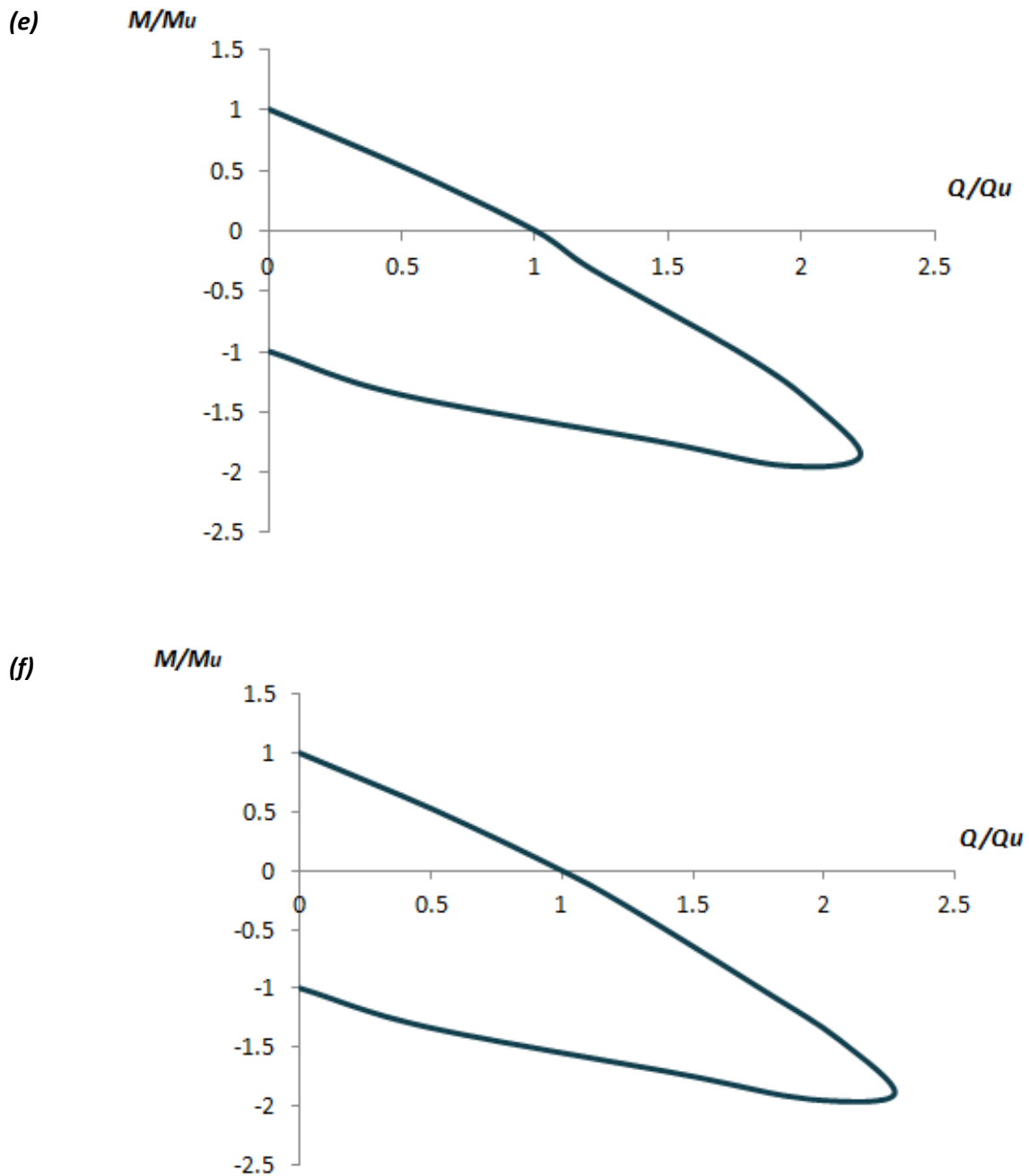
Figure 3.21 *Failure Envelopes of deeply embedded foundations for coefficient of friction μ=1 , embedment ratio D/B=1 and factors of safety (a) FS_v=10 (b) FS_v=3.33 (c) FS_v=5 (d FS_v=1.43 (e) FS_v=1.25 and (f) FS_v=1.11*
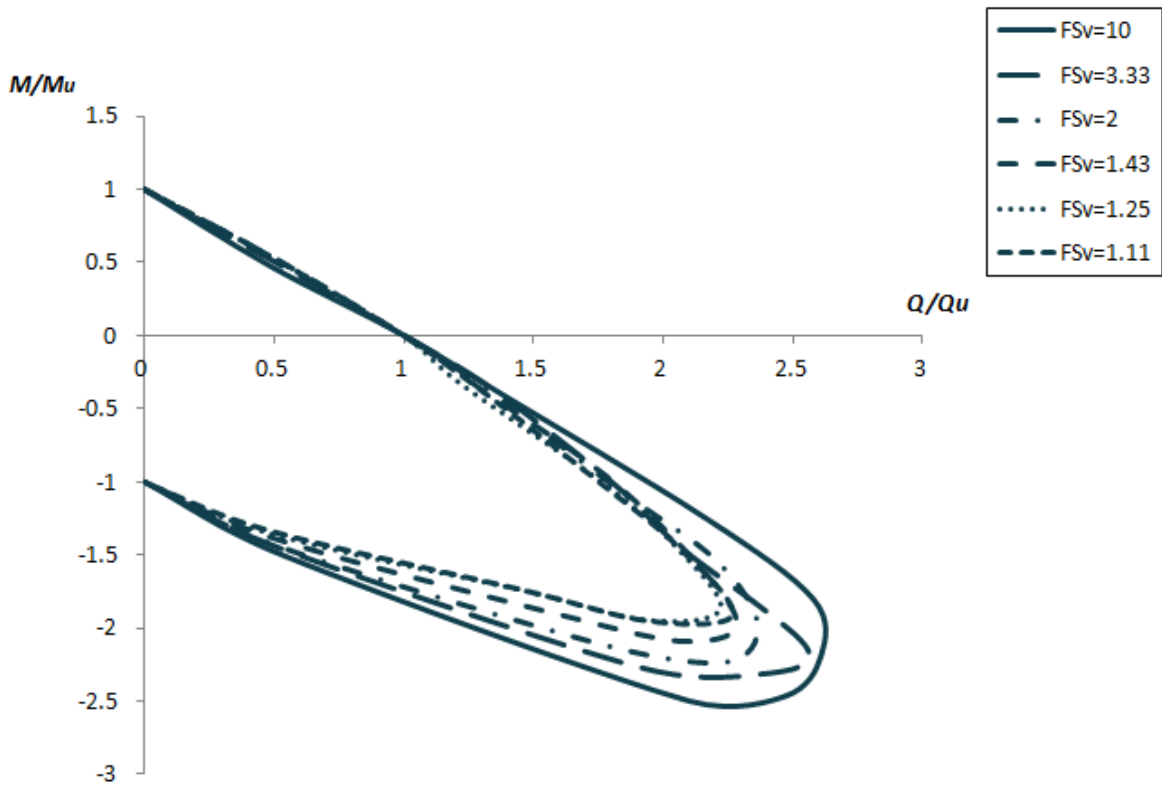
Figure 3.22 *Comparison of failure envelopes of deeply embedded foundations for coefficient of friction μ=1 , embedment ratio D/B=2 and every examined factor of safety*

(a)

(b)

(c)

(d)

(e)

(f)

(g)

(h)

(i)
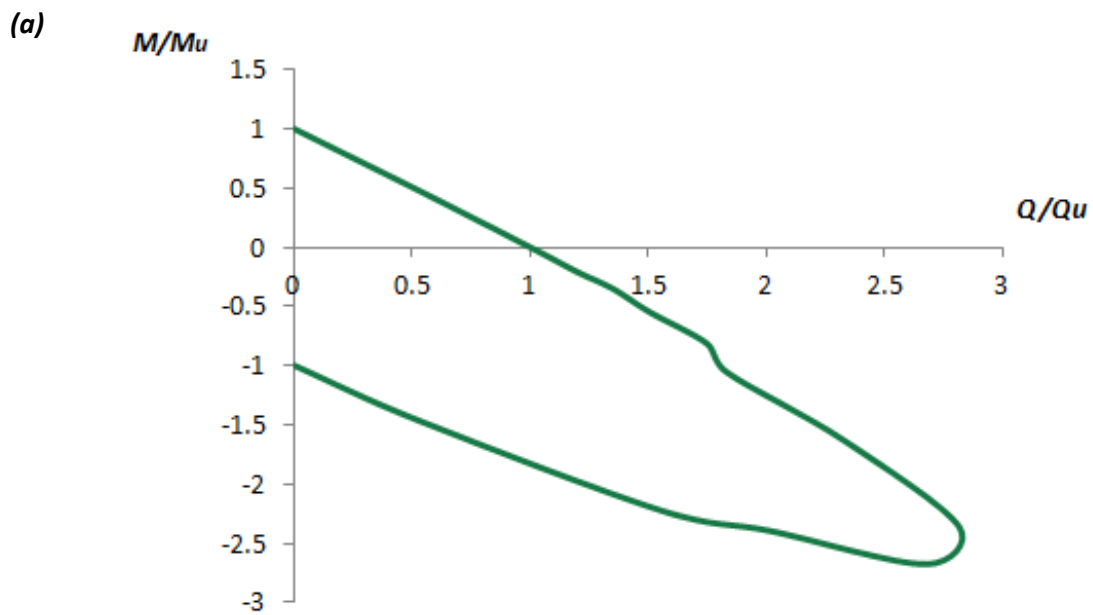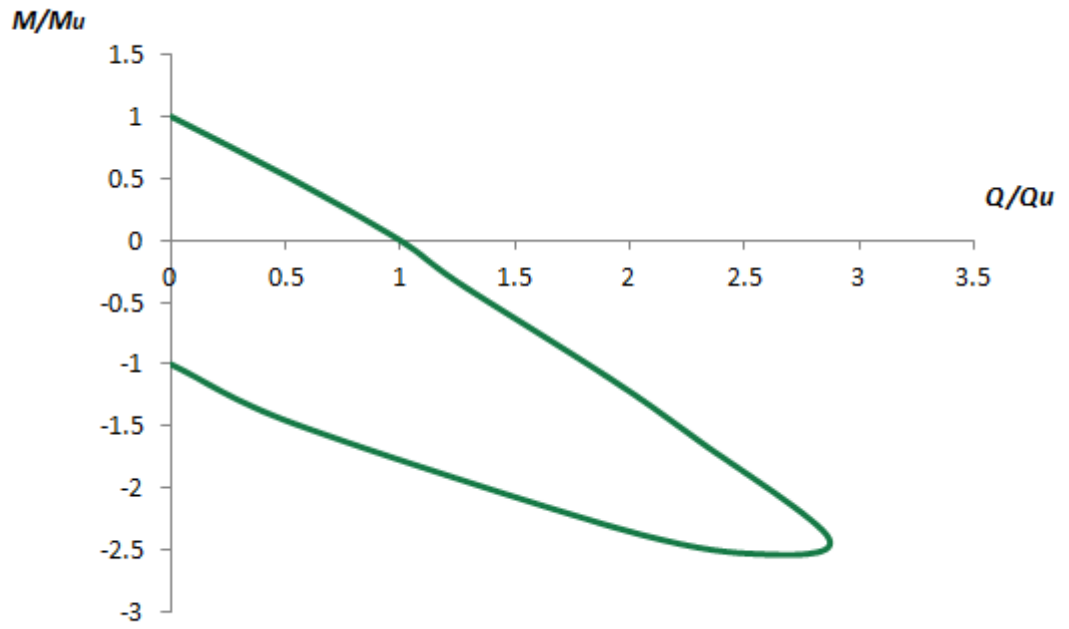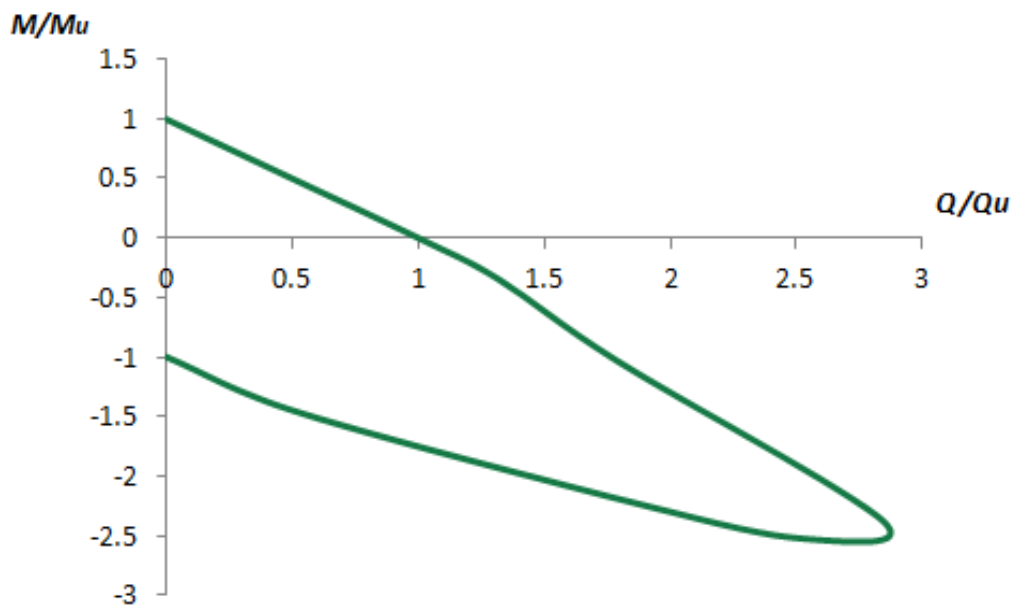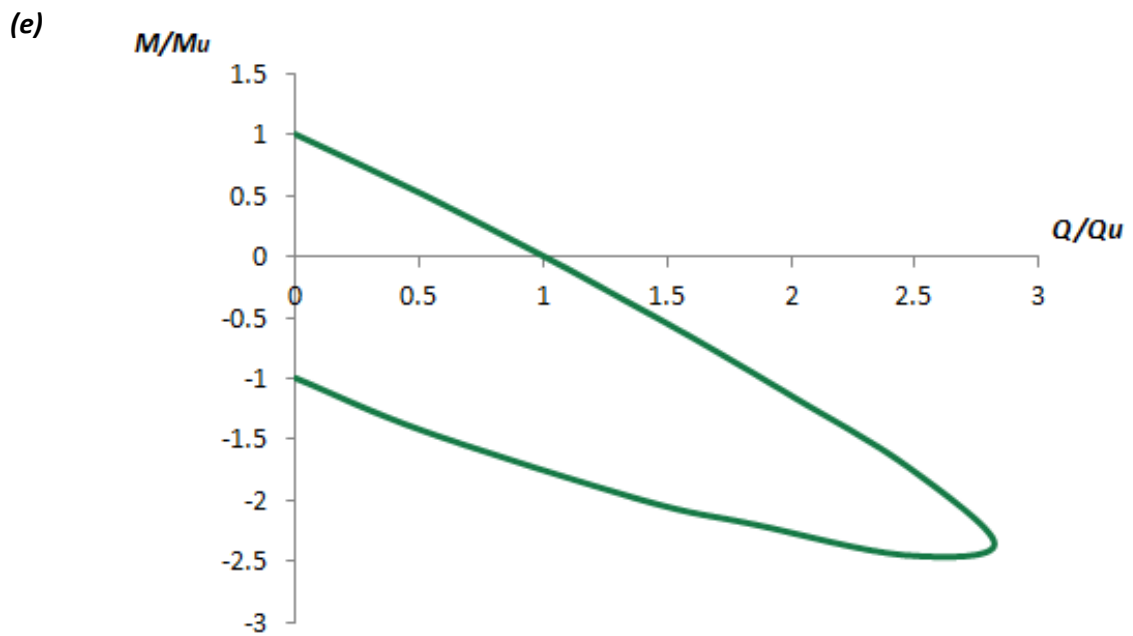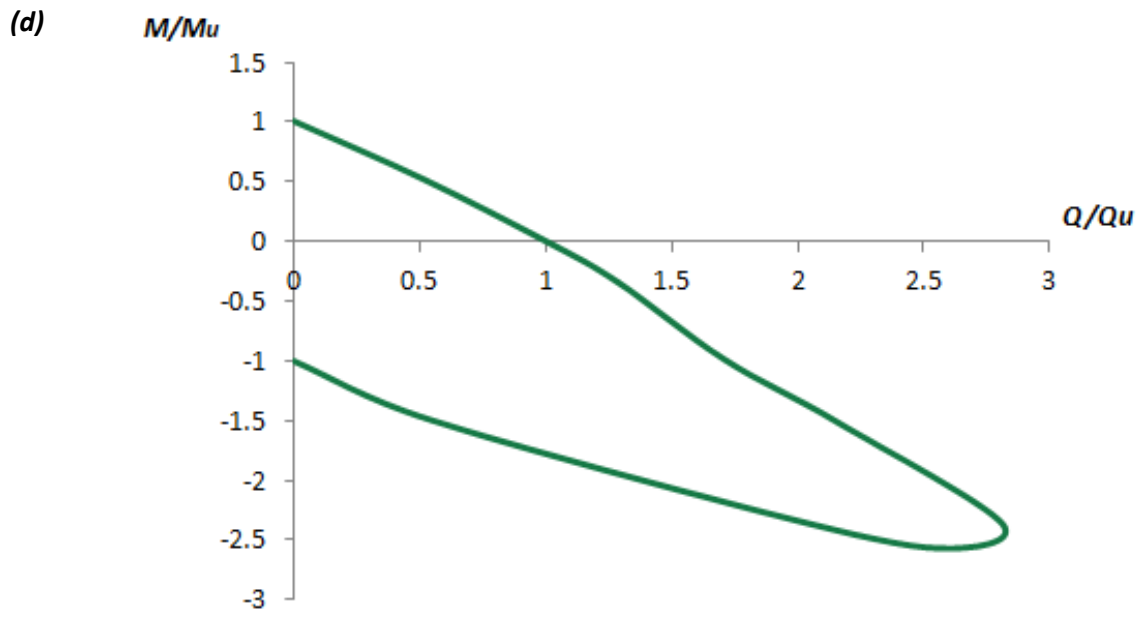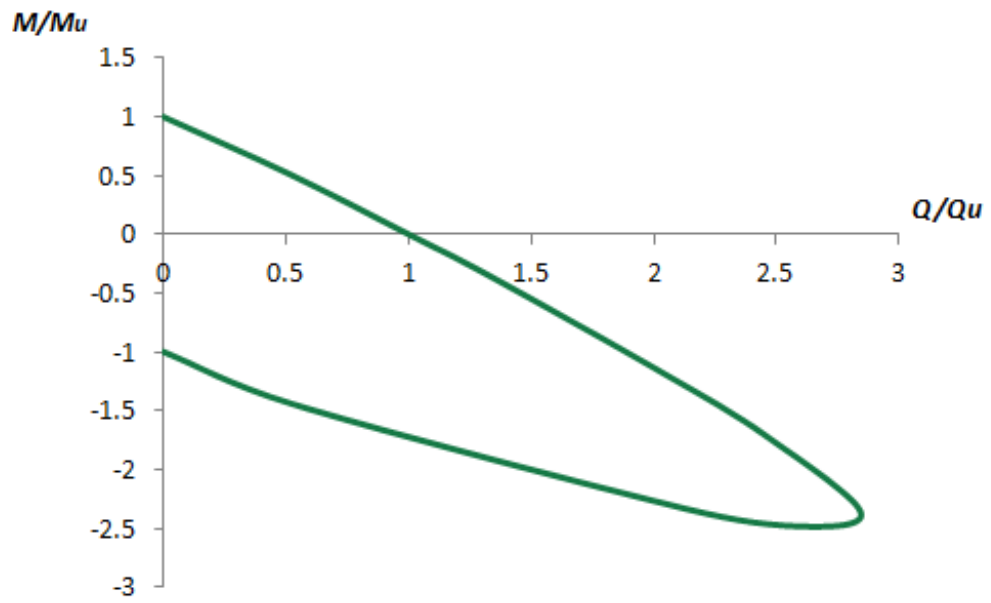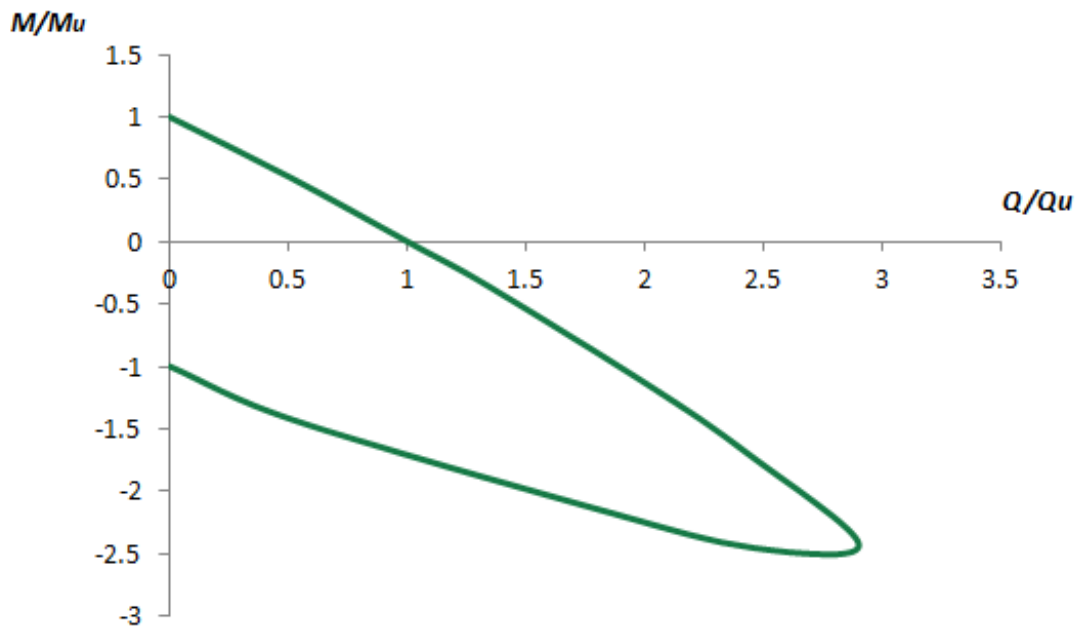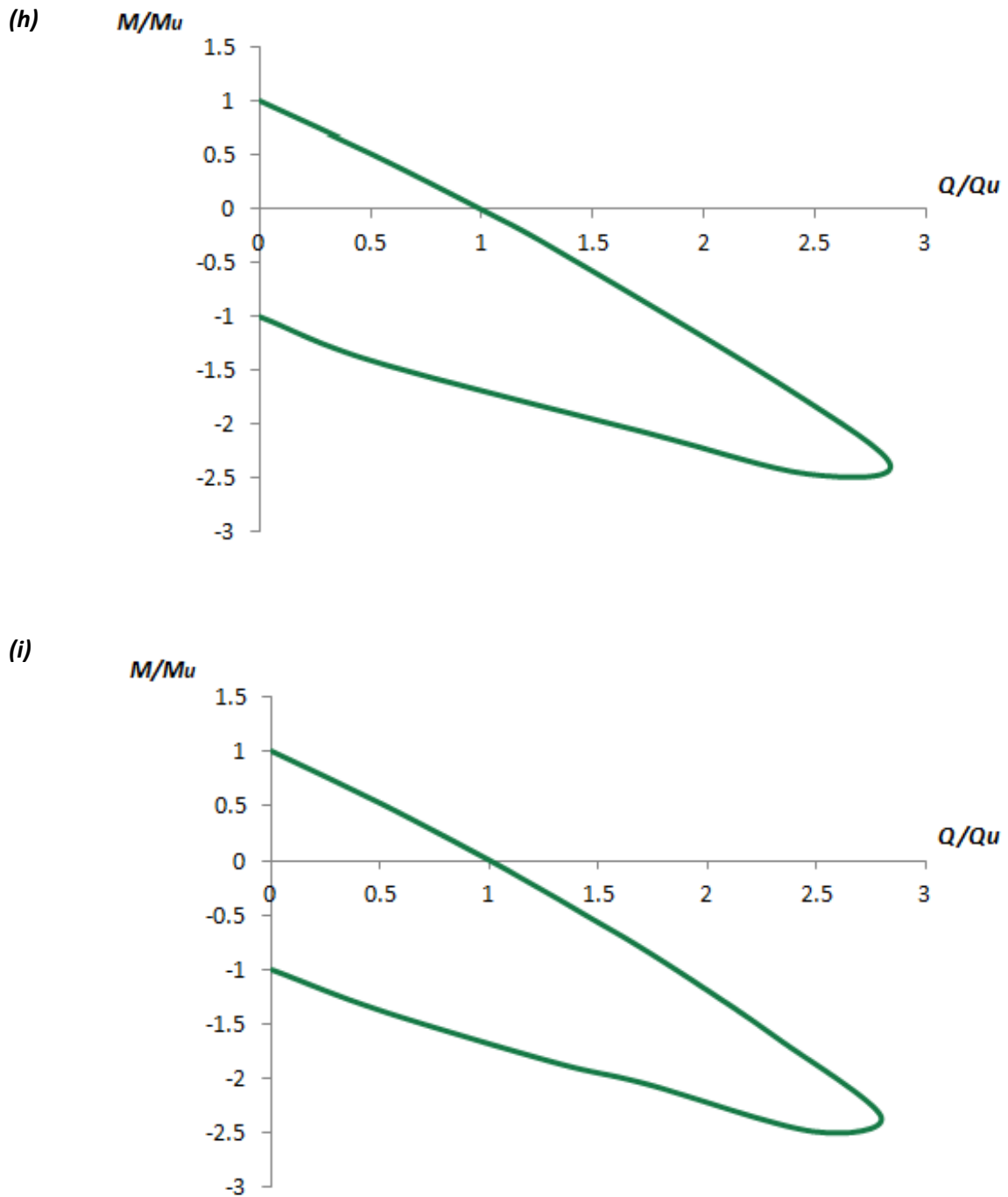
Figure 3.23 *Failure Envelopes of deeply embedded foundations for coefficient of friction μ=1, embedment ratio D/B=3 and factors of safety* **(a)** *FS$_v$=10* **(b)** *FS$_v$=5* **(c)** *FS$_v$=3.33* **(d)** *FS$_v$=2.5* **(e)** *FS$_v$=5* **(f)** *FS$_v$=1.67* **(g)** *FS$_v$=1.43* **(h)** *FS$_v$=1.25 and* **(i)** *FS$_v$=1.11*
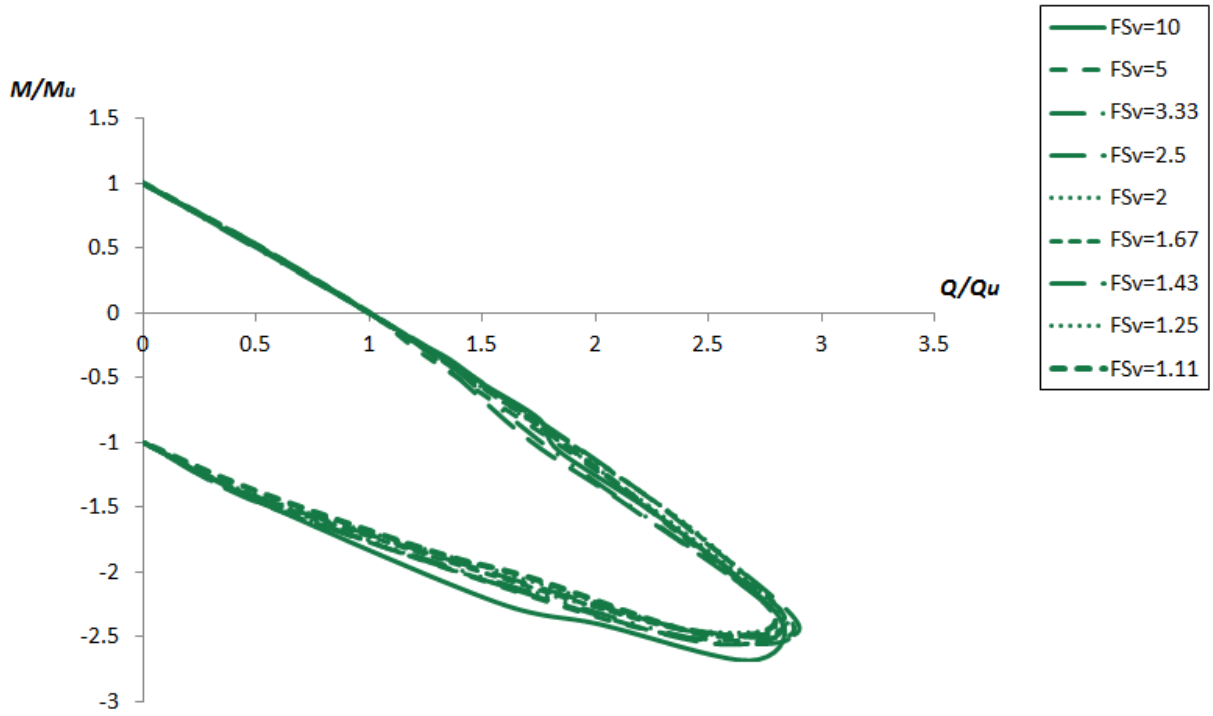
Figure 3.24 *Comparison of failure envelopes of deeply embedded foundations for coefficient of friction μ=1 , embedment ratio D/B=3 and every examined factor of safety*
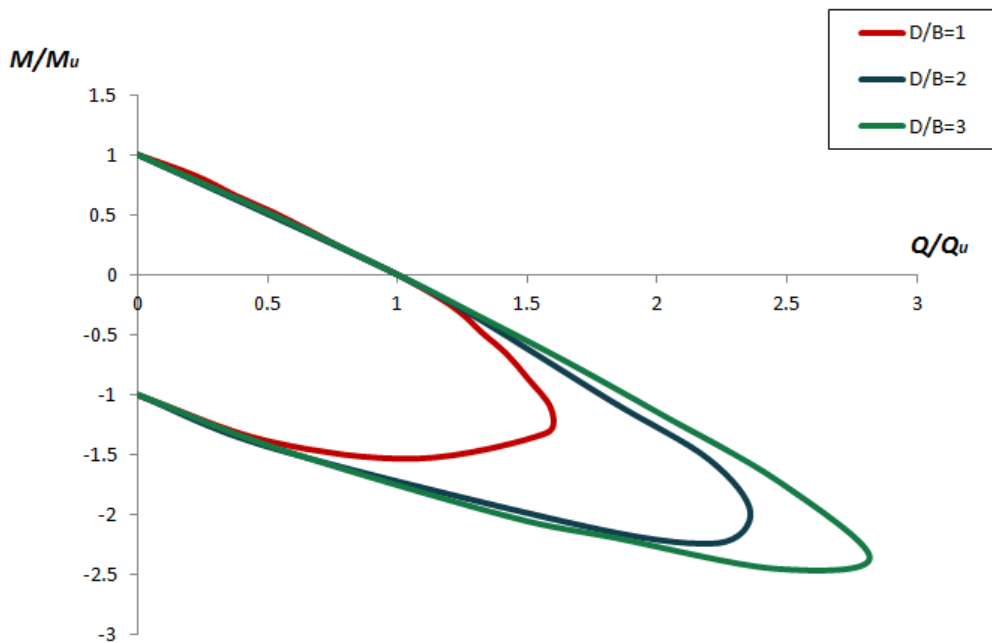
Figure 3.25 *Failure envelopes for three different embedment ratios (D/B=1, 2, 3) and the same static safety factor (FS$_v$ =2.5) . We observe that as the embedment ratio increases the failure envelopes expand.*
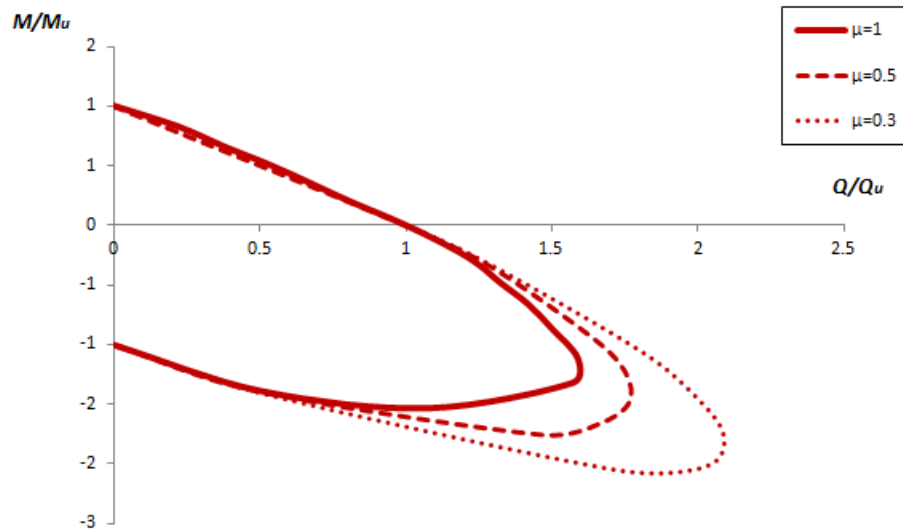

Figure 3.26 *Failure envelopes for embedment ratio D/B=1, static safety factor FS$_v$ =2 and different coefficients of friction μ=1, 0.5, 0.3*
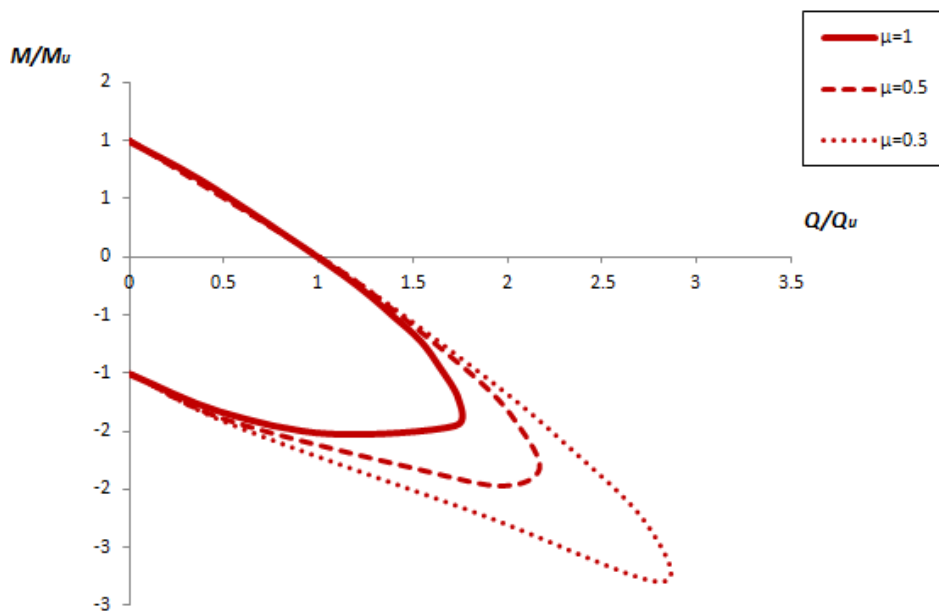
Figure 3.27 *Failure envelopes for embedment ratio D/B=1, static safety factor FS$_v$ =1.11 and different coefficients of friction μ=1, 0.5, 0.3*
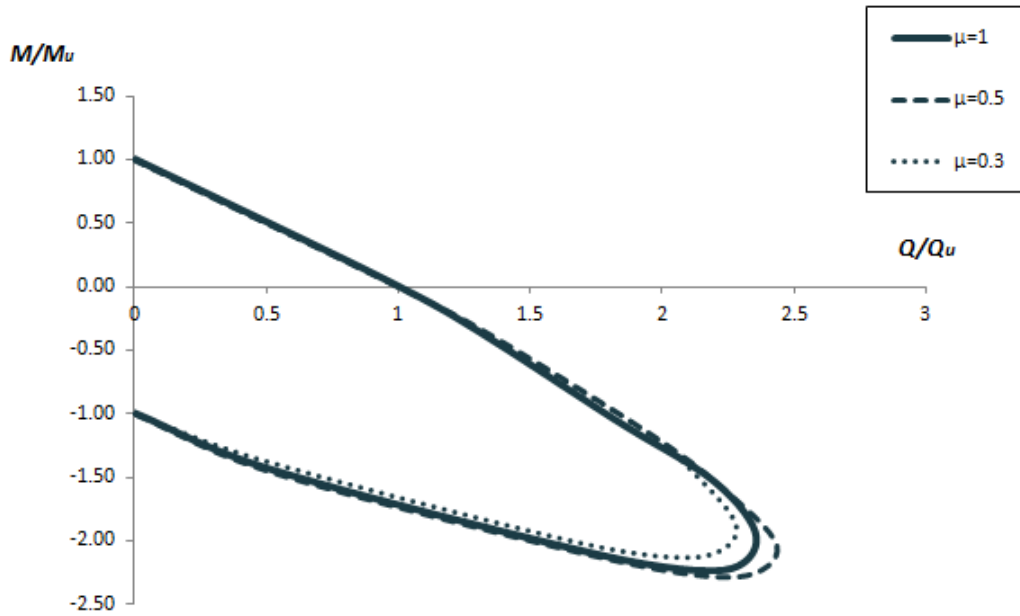
Figure 3.28 *Failure envelopes for embedment ratio D/B=2, static safety factor FS$_v$ =2 and different coefficients of friction μ=1, 0.5, 0.3*
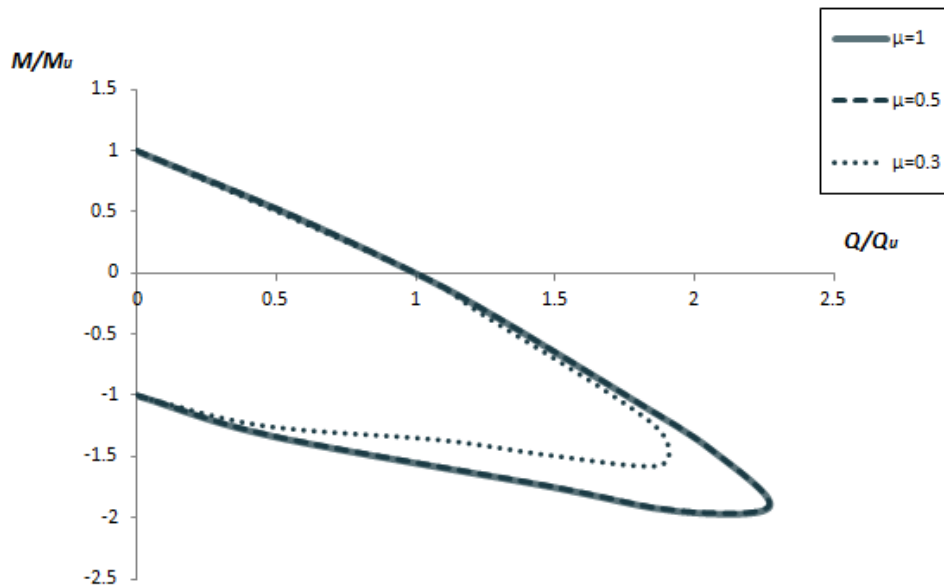
Figure 3.29 *Failure envelopes for embedment ratio D/B=2, static safety factor FS$_v$ =1.11 and different coefficients of friction µ=1, 0.5, 0.3*
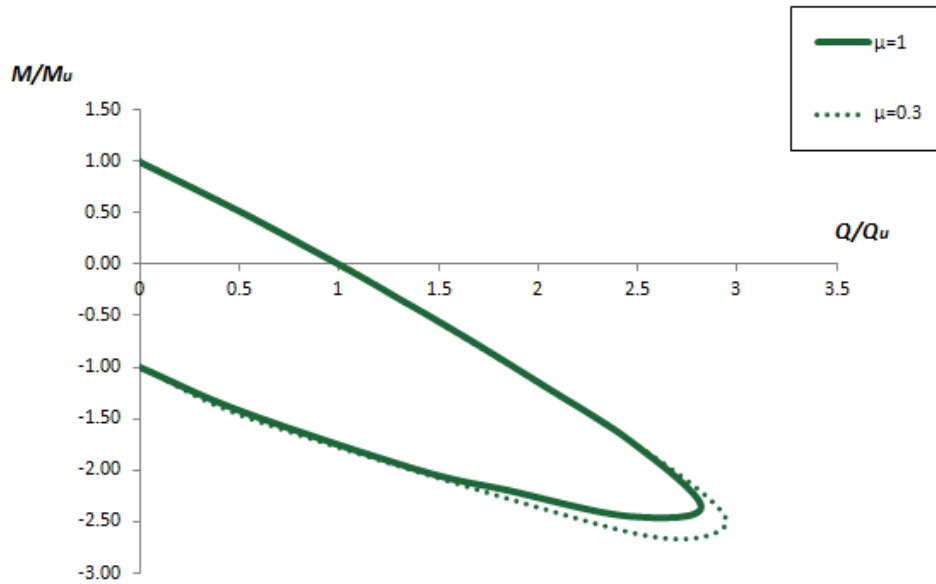
Figure 3.30 *Failure envelopes for embedment ratio D/B=3, static safety factor FS$_v$ =2 and different coefficients of friction µ=1, 0.3*
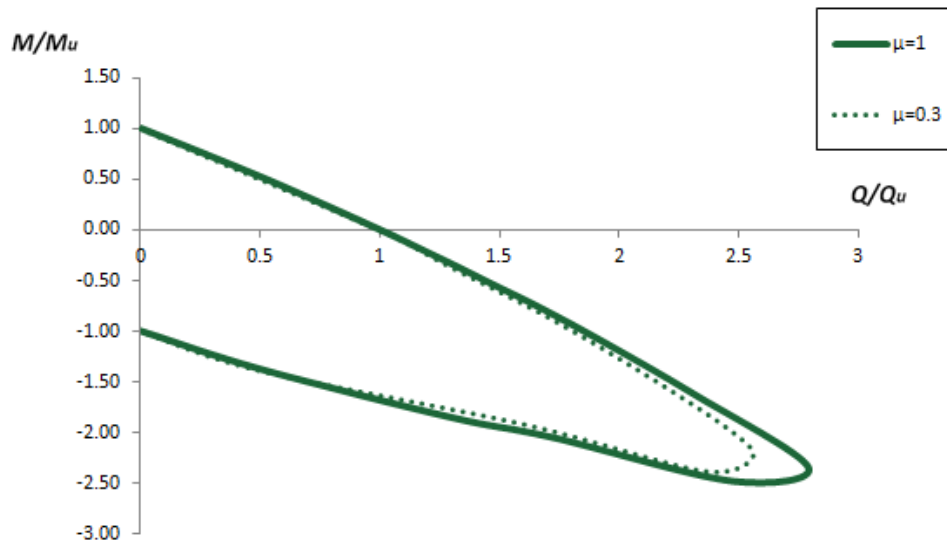
Figure 3.31 *Failure envelopes for embedment ratio D/B=3, static safety factor FS$_v$ =1.11 and different coefficients of friction μ=1, 0.3*
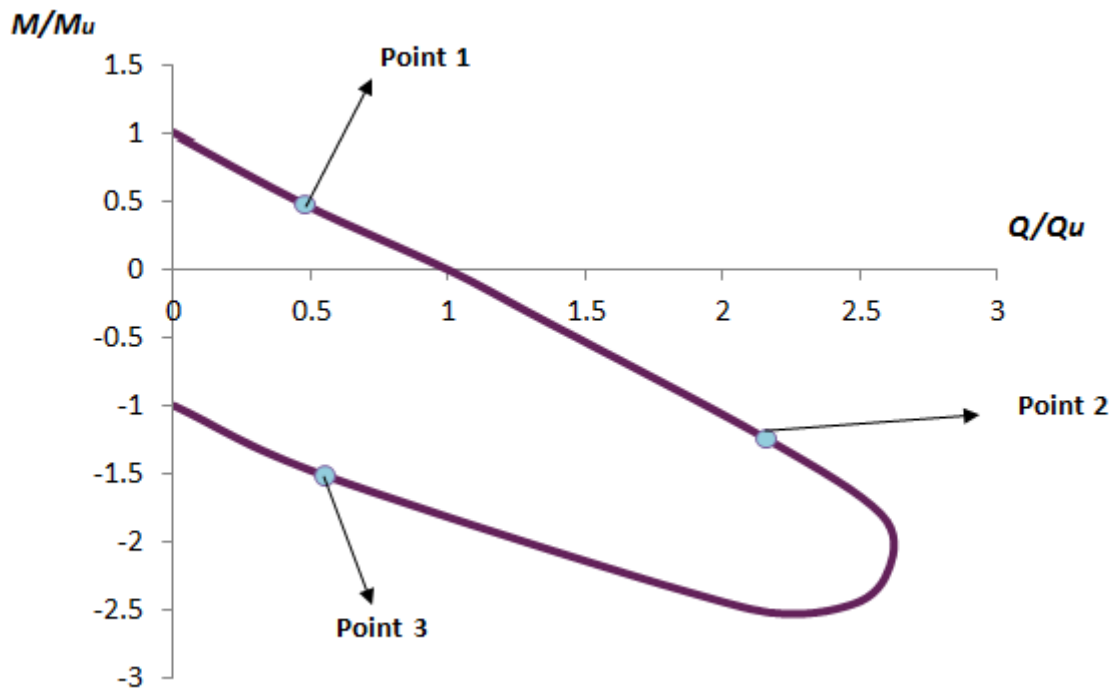
**Figure 3.32** *Points that are chosen from a failure envelope to produce the load-displacement curves which are presented in the next figures.*

Point 1
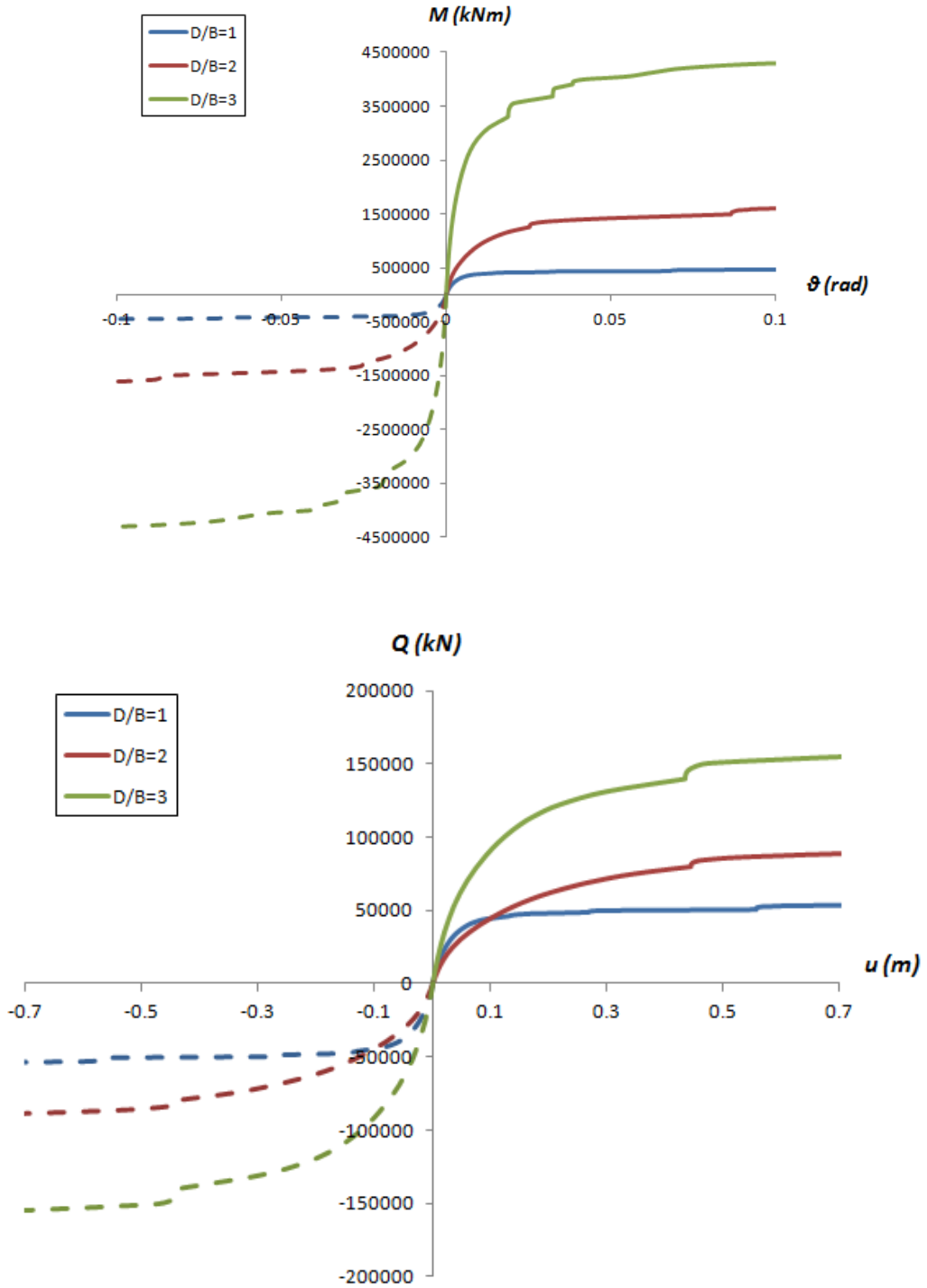
Point 2
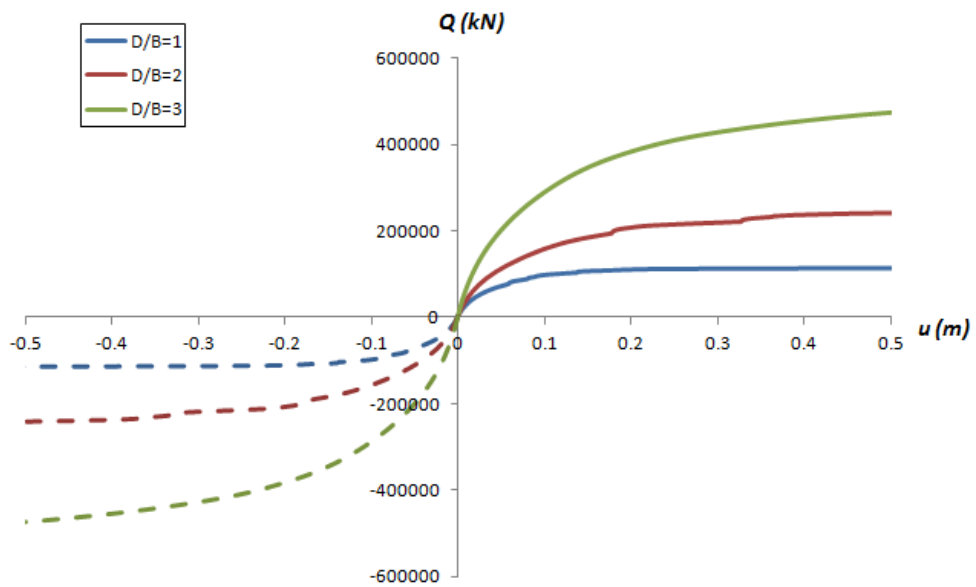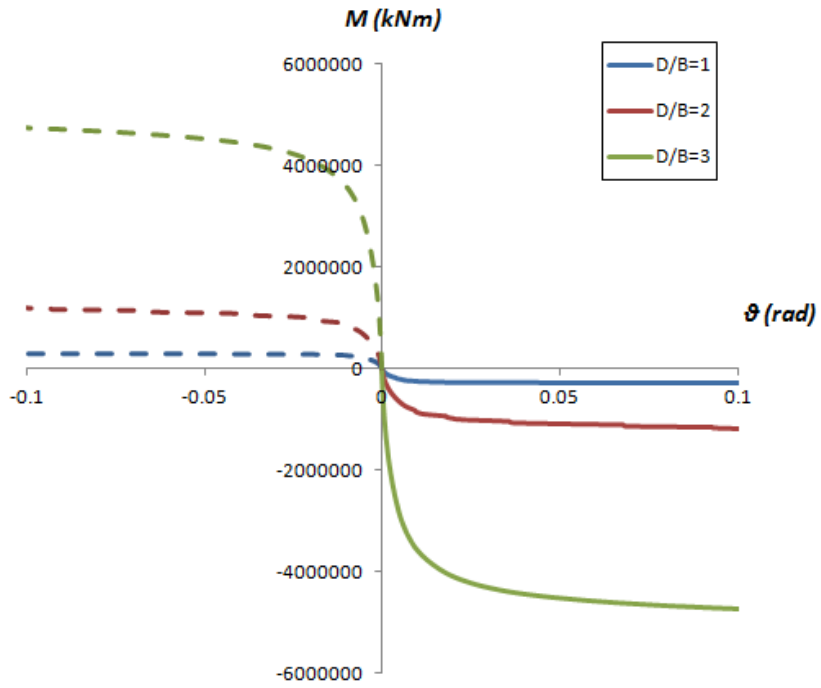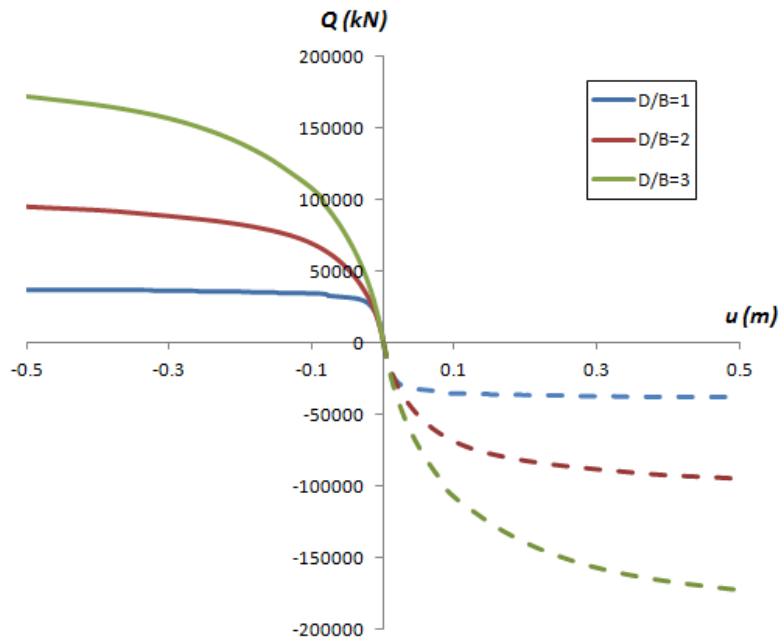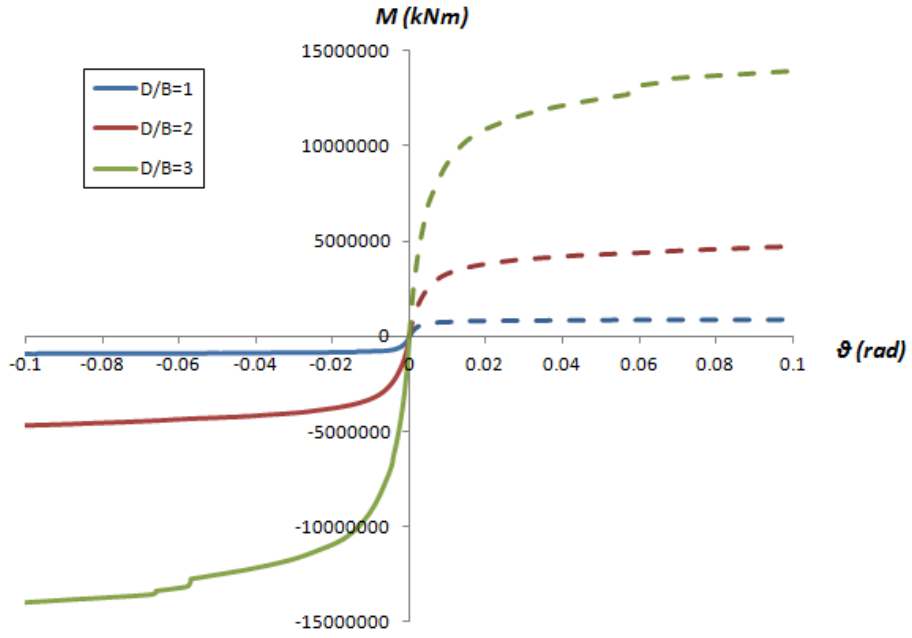
Point 3

Figure 3.33 *Moment-rotation and horizontal load-displacement curves for points 1, 2 and 3, for embedment ratios D/B=1,2,3 , coefficient of friction μ=1 and safety factor FS$_v$=10.*
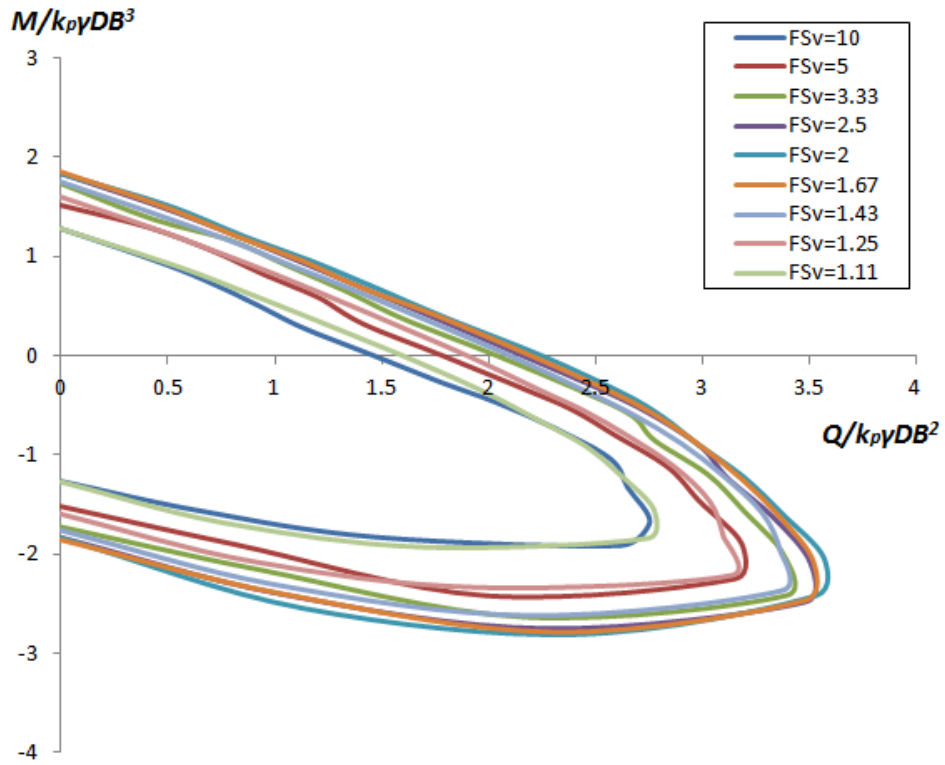
Figure 3.34 *Dimensionless failure envelopes for D/B=1 , μ=1 and safety factors FS$_v$=10, FS$_v$=5, FS$_v$=3.33, FS$_v$=2.5, FS$_v$=2, FS$_v$=1.67, FS$_v$=1.43, FS$_v$=1.25 and FS$_v$=1.11*
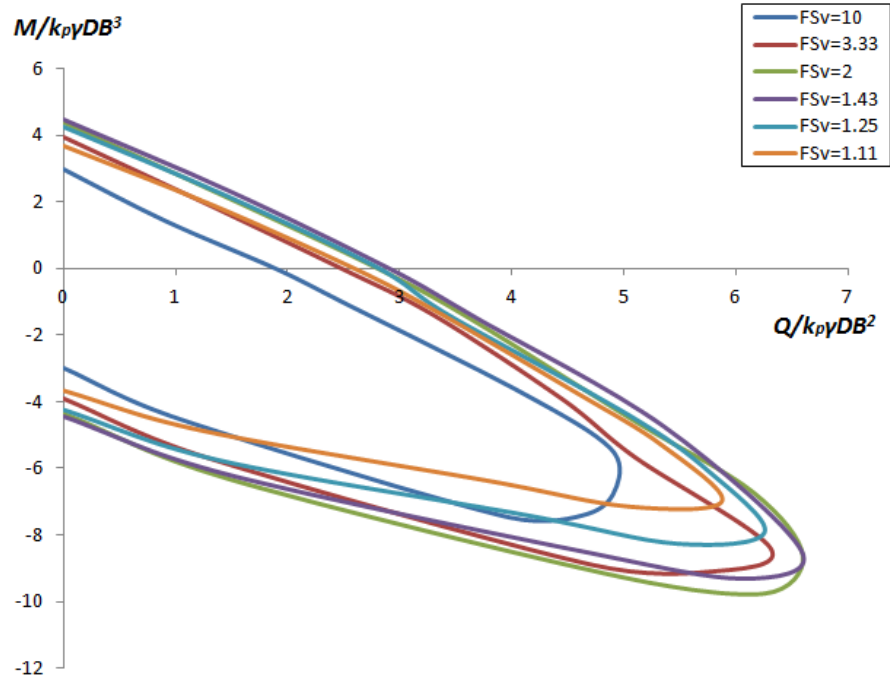
Figure 3.35 *Dimensionless failure envelopes for D/B=2 , μ=1 and safety factors FS$_v$=10, FS$_v$=3.33, FS$_v$=2, FS$_v$=1.43, FS$_v$=1.25 and FS$_v$=1.11*
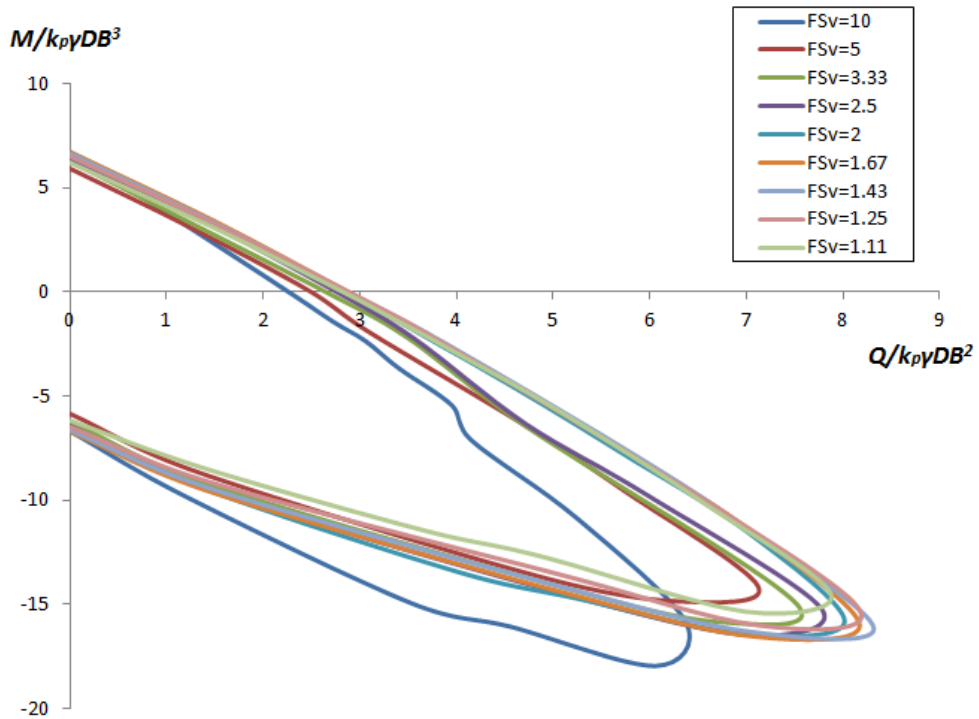
Figure 3.36 *Dimensionless failure envelopes for D/B=3 , μ=1 and safety factors FS_v=10, FS_v=5, FS_v=3.33, FS_v=2.5, FS_v=2, FS_v=1.67, FS_v=1.43, FS_v=1.25 and FS_v=1.11*

(a)

(b)

(c)

(d)

(e)

(f)
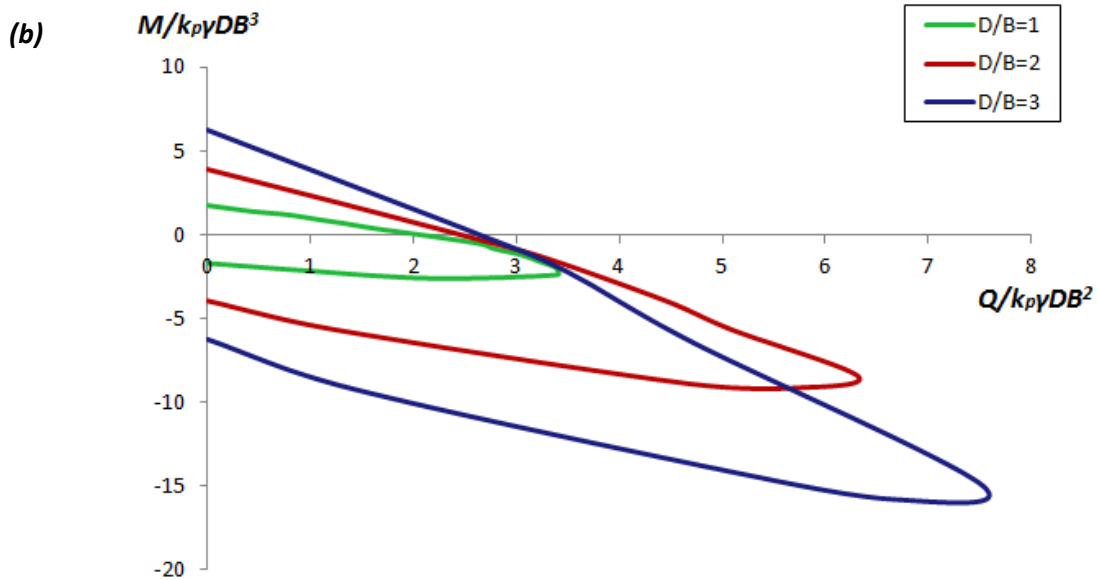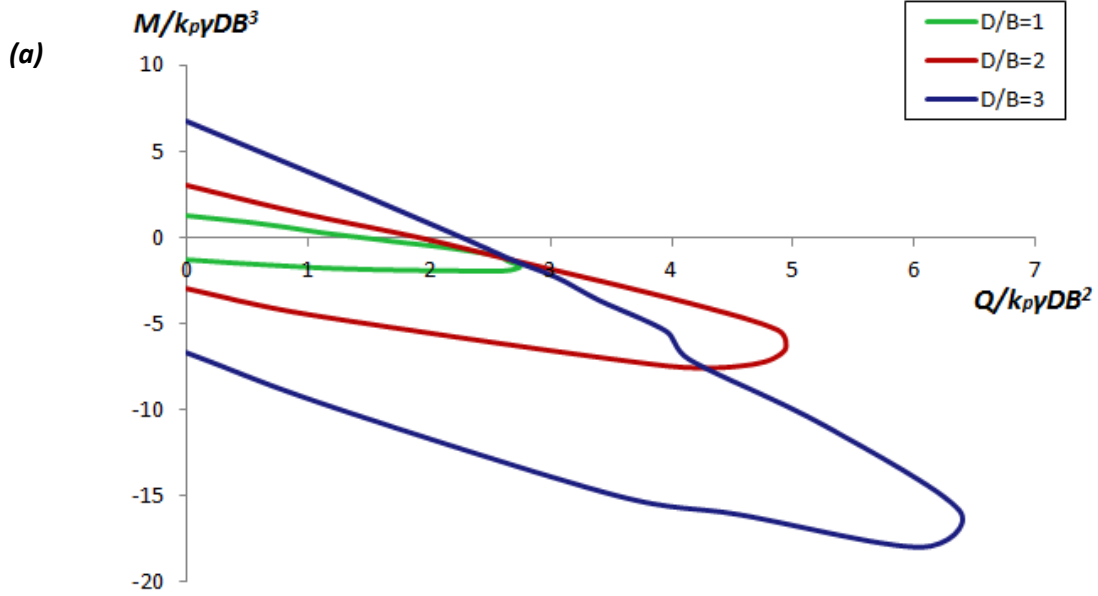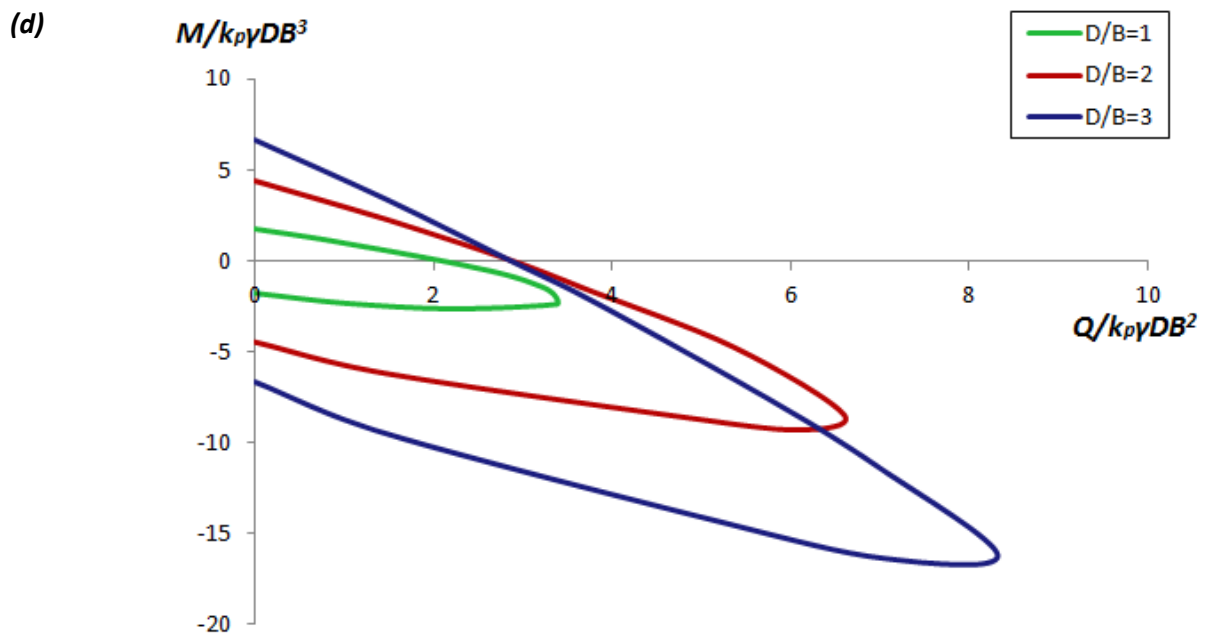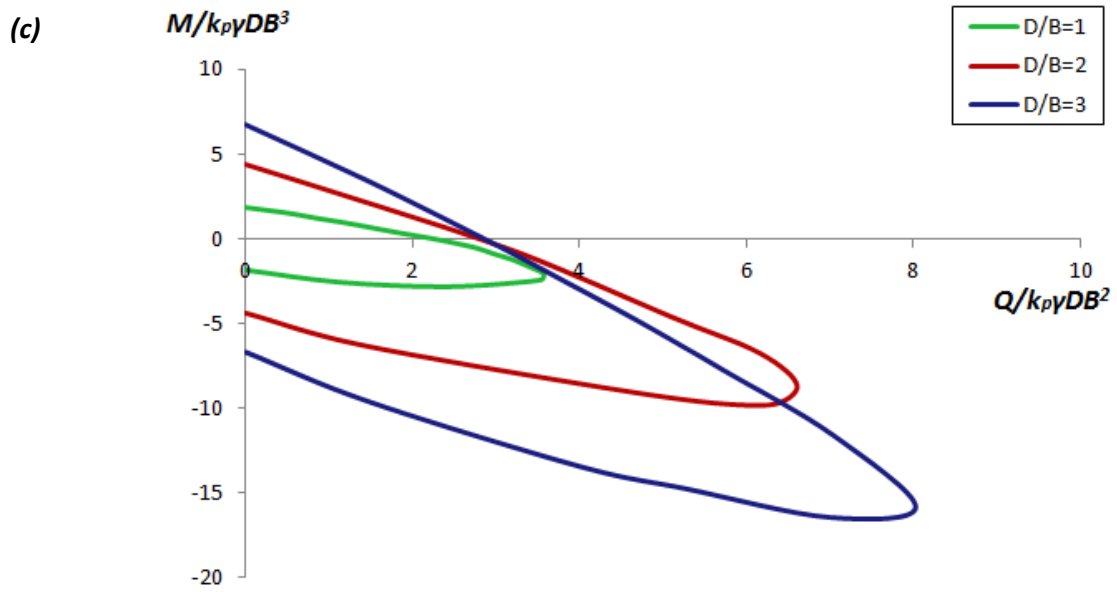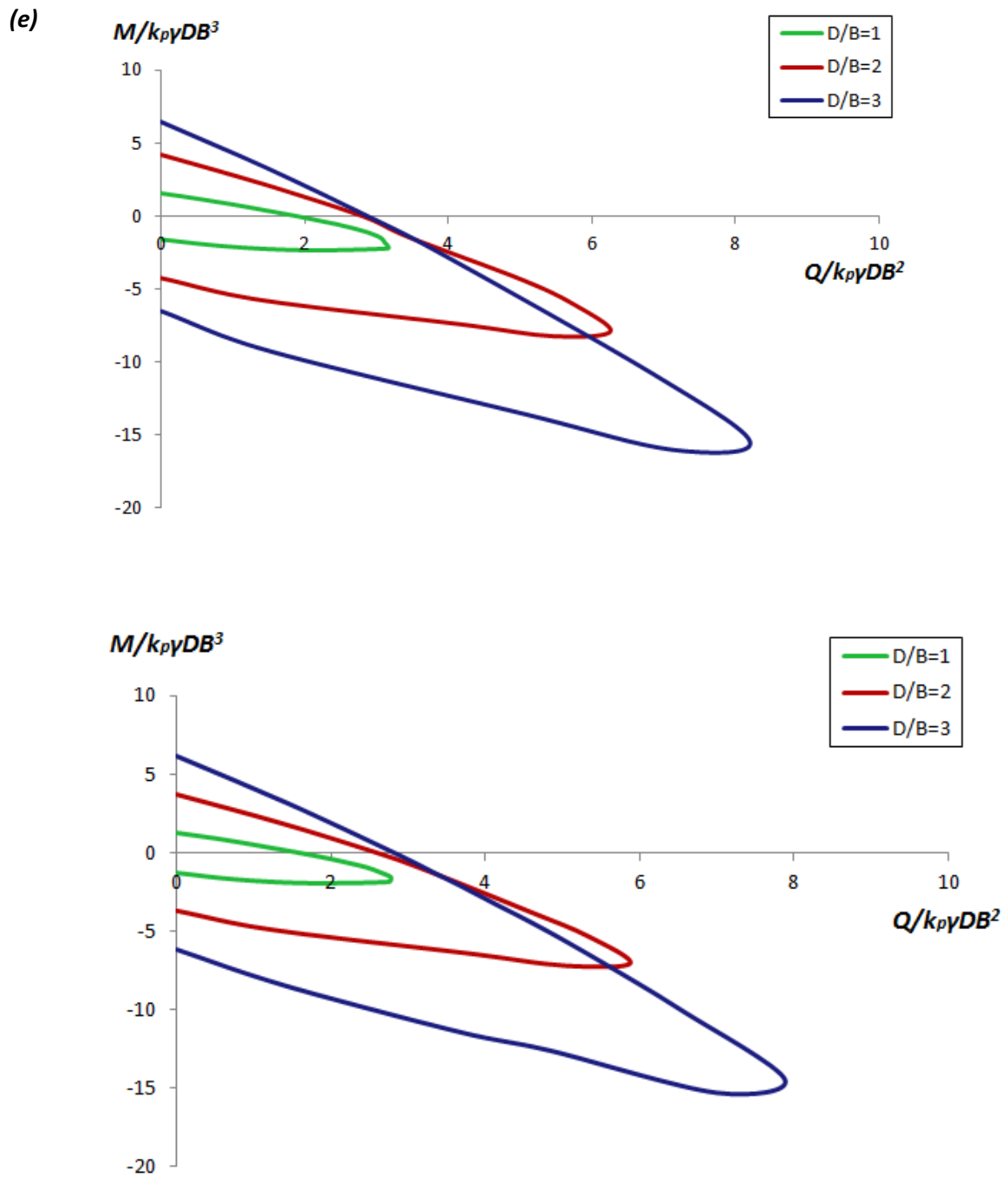
Figure 3.37 *Comparison of dimensionless failure envelopes for embedment ratios D/B=1,2 and 3, μ=1 and safety factors **(a)** FS$_v$=10 , **(b)** FS$_v$=3.33, **(c)** FS$_v$=2, **(d)** FS$_v$=1.43, **(e)** FS$_v$=1.25 and **(f)** FS$_v$=1.1*
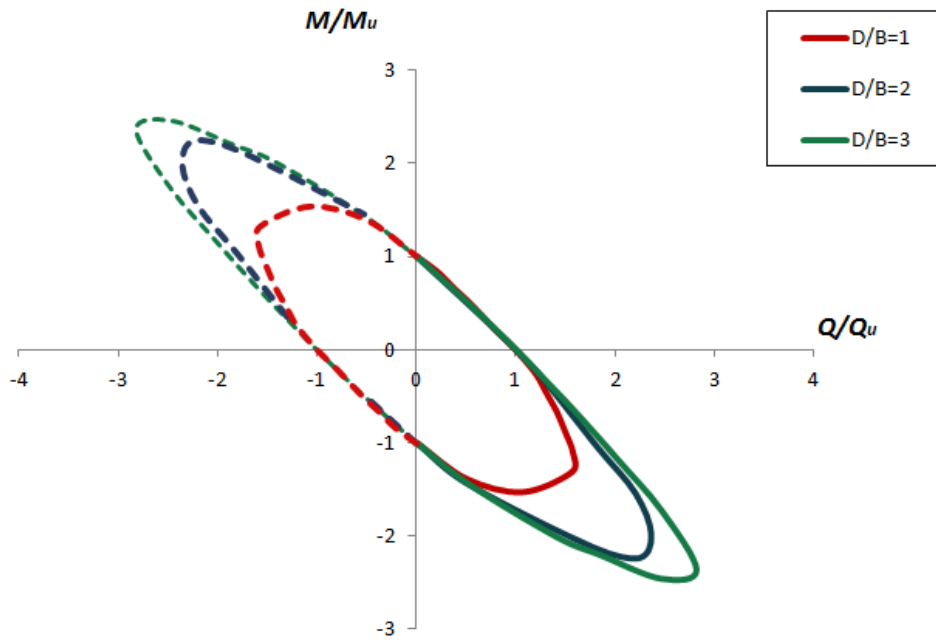
Figure 3.38 *Symmetry of the first to the third quadrant and the fourth quadrant to the second one in failure envelopes for different embedment ratios*
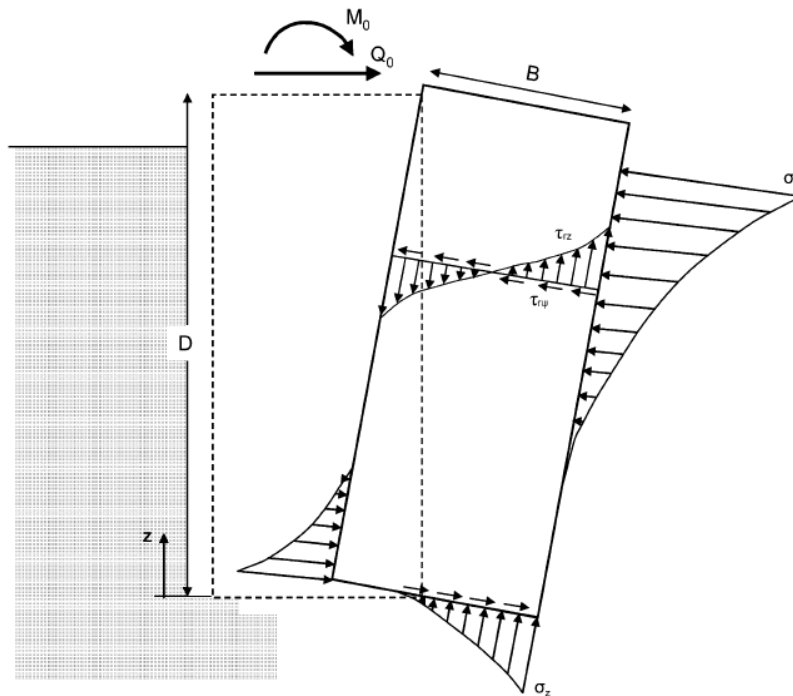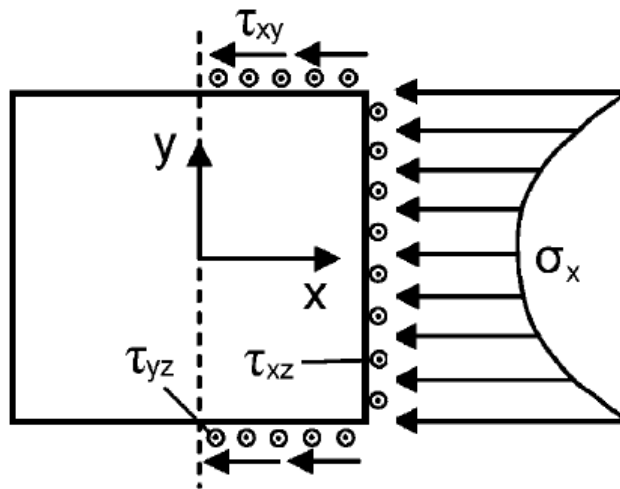
Figure 3.39 *A typical caisson foundation of square plan. The distributions of stresses are schematically illustrated along the soil-caisson interface*

CHAPTER 4

SOIL DEFORMATION MECHANISMS

4.1 *Theoretical Background*

The three dimensional analyses that were performed for the purposes of this thesis, were aimed both at the production of deeply embedded foundations' failure envelopes as well as the study of the different soil deformation mechanisms mobilized during the system's failure. Along a failure envelope, different soil deformation mechanisms are mobilized at every point as many researchers have already indicated [*Salençon and Pecker 1995; Bransby and Randolph 1998; Ukritchon et al. 1998*], suggesting the immediate dependency of the manifested mechanisms on the ratio of the imposed loads M/Q (i.e. the lever arm considered during the static pushover tests, whether that is the height of a bridge's pier or the height of a sDoF oscillator).

Bransby and Yun *[2009]* performed rigid plasticity upper-bound analyses in order to classify the soil failure conditions under combined foundation loading (vertical load N, horizontal load Q and overturning moment M). Those analyses were performed according to the methods proposed by Bransby and Randolph *[1998]* through postulated simple but kinematically variable soil deformation mechanisms, which were based on those observed

during the finite element calculations. Their study focused on skirted foundations, *Figure 4.1.a*, thus taking into account certain additional soil deformation mechanisms that are not available in the case of solid deeply embedded foundations (caissons) since deformation can be observed in-between the skirts.

In *Figure 4.1.b* the aforementioned soil deformation mechanisms are illustrated, as indicated in Bransby and Yun's study. These mechanisms can be classified into the following categories, based on the terminology that was introduced in the particular study : (a) "forward scoop" , (b) "scoop-slide", (c) "internal Hansen", (d) "reverse scoop" and (e) "internal double scoop". It should be noted that the mechanisms pertaining solely to skirted foundations are (c) and (e), which are comprised of a number of elaborate soil deformation mechanisms, and are therefore not examined in the herein study. In brief, the calculation of the section forces at failure through upper-bound plasticity analyses, consists of two steps. Initially, to find a single point on the failure envelope two load components were selected (e.g. Q=0, N=0). Upper-bound work calculations were then carried out numerically in a spreadsheet with each available deformation mechanism to find the lowest value of the unknown load (here the overturning moment M). For each mechanism, the kinematic variables (e.g. the length L; Fig. 3) were changed to give the lowest collapse load. The lowest value found represented the best estimate (lowest upper-bound solution) of the combined N–Q–M failure condition. This process was then repeated for different values of Q and N to describe key sections of the failure envelope. This process was carried out for different soil and foundation conditions to examine how these affected the foundation capacity and optimal failure mechanisms and to compare the results with those from the sideswipe tests, as shown in *Figure 4.2*.

4.2 *Classification of failure envelopes' characteristic points*

Figures 4.3, 4.5 and *4.7* illustrate the plastic strain magnitude contours at the point of failure at characteristic points for caisson foundations of the three embedment ratios considered herein, for a coefficient of friction μ=1 and for the characteristic factor of safety against vertical loading *FS_v = 2*. Furthermore, in *Figures 4.4, 4.6* and *4.8* we compare the plastic strain magnitude contours at characteristic points at the point of failure for three different safety factors (*FS_v = 10,2 and 5)* and each figure concerns a different embedment ratio: D/B=1, 2 or 3 respectively. Finally, in *Figure 4.9* we compare the plastic strain magnitude contours at the point of failure for FS_v=2 and every embedment ratio.

The failure points along the yield surface in these figures were picked to match either a limit value of a load component *M* or *Q* or a characteristic location of the pivot point in respect to the depth of embedment *D*. These points include:

(a) Ultimate moment capacity: $Q = 0$, $M = M_u$
(b) Ultimate horizontal load capacity: $Q = Q_u$, $M = 0$
(c) Point of "negative" horizontal load and "negative" moment : $Q > 0$, $M < 0$, z_p=D
(d) Maximum horizontal capacity: $Q = Qmax$, $M < 0$, , $z_p = \infty$
(e) Maximum moment capacity: $Q > 0$, $M = M_{max}$, , z_p=0

We can observe that every mobilized soil deformation mechanism of the embedded foundation does not depend on the embedment ratio D/B or on the static safety factor FS_v; it only depends on the location of the considered point on the failure envelope. It follows that the individual points of the failure envelopes can be classified into the following categories :

i) Point (a) of ultimate moment capacity corresponds to the "forward scoop" category.

ii) Point (b) of ultimate horizontal capacity corresponds to a "scoop-slide" mechanism.

iii) Point (c) of positive horizontal load and negative moment , Q>0 and M<0, corresponds to an even deeper "scoop-slide" mechanism.

iv) Point (d) of maximum horizontal capacity Q_{max} corresponds to a pure sliding mechanism. This particular mechanism has not been identified neither is it clearly depicted in **Figure 4.1.b** , although it can be considered similar to mechanism (c) of the specific figure. As we have already indicated, mechanism (c) is not applicable in the case of solid embedded foundations, as it involves soil deformation between the skirts of the foundation, thus pertaining only to skirted foundations. Nevertheless, if we ignore the deformed soil between the skirts, at the point of maximum horizontal capacity , the soil ,both in front of the caisson and behind it, is deformed in a way similar to the one manifested in skirted foundations.

v) Point (e) of maximum moment capacity M_{max} corresponds to the "reverse scoop" category, with a prevailing rotational trend. In this case, the response of the system is fundamentally different from the response manifested for maximum horizontal capacity Q_{max}, since the foundation's rotational component is now significantly enhanced in comparison to the displacement component.

The differentiation between the mechanisms that shallow and deep embedded foundations exhibit at maximum horizontal capacity is of particular importance. In the former, the small depth of embedment allows for a plastic strain localization (shear band) to be developed while both the caisson and the soil lying above the failure zone move as a "rigid" body. In the case of a deeply embedded foundation, however, it seems that the critical type of failure is not localized but rather diffusive. This means that plastification is

not limited to a small shear band but is diffused to the soil surrounding the caisson. A smaller diffusive mechanism is also deployed at the point where deeply embedded foundations exhibit their maximum moment capacity. Driven by the similar characteristics of the *d)-e)* region of the envelope - lack of a specific pivot point - we make the assumption that deeply embedded foundations actually exhibit the above behavior in the whole *d)–e)* region of their yield surface.

The five distinct types of soil resisting mechanisms that are deployed by embedded foundations subject to combined M-Q loading are presented in ***Figure 4.10.*** The above considerations allow us to map the yield surface according to ***Figure 4.11.***

The aforementioned mechanisms are manifested for about the same load angle (where as load angle we define the ratio of the moment M to the shear force Q at failure) regardless of the embedment ratio or the factor of safety against vertical loading. The above is validated by ***Figures 4.12, 4.14, 4.16*** where the pivot points are schematically illustrated through contours of resultant displacement at the point of failure for caisson foundations of embedment ratios D/B=1,2 and 3 respectively, for a coefficient of friction μ=1 and for the characteristic factor of safety against vertical loading $FS_v = 2$. Furthermore, in ***Figures 4.13, 4.15*** and ***4.17*** we compare the pivot points at the point of failure for three different safety factors ($FS_v = 10,2$ *and 5)* and each figure concerns a different embedment ratio: D/B=1, 2 or 3 respectively. Finally, in ***Figure 4.18*** we compare the pivot points at the point of failure for FS_v=2 and every embedment ratio. Evidently, for ultimate moment capacity (point a)), the foundation rotates around a point located approximately at the middle of the caisson's height. Moving along the yield surface in a clockwise fashion, for absolutely smaller load angles, the depth of the pivot point increases, reaching the depth of embedment *D* at point c). At this point, the caisson moves as an inverted pendulum. After that point, the depth of the pivot point increases dramatically approaching infinity at point d) (pure sliding). This is actually the deepest "scoop-slide" mechanism that can be

developed. In a very short region, the depth of the pivot point is nullified and a pendulum mechanism is revealed. In the final section, the pivot point is lowered again reaching its starting value, this time for negative ultimate moment capacity. Observing **Figure 4.18** we conclude that the pivot path is fairly insensitive to the embedment ratio. However, if we carefully notice **Figures 4.13, 4.15** and **4.17** , even though the depth of the pivot point remains the same despite the change in vertical load, we can detect a shift of the pivot point in the horizontal direction: as the safety factor decreases from $FS_v=10$ to $FS_v=1.11$ for points a), b) and c) the position of the pivot point shifts to the left. To explain this behavior we can examine the accumulation of plastic shear strains (**Figures 4.4, 4.6** and **4.8**). Evidently, as the vertical load increases the symmetry in the mobilized failure mechanisms vanishes. The response of the system is instead described by excessive accumulation of plastic shear strains in the direction of the prevalent loading ,(in this case to the right of the caisson) and the soil is significantly deformed, something that can explain the shift of the pivot point to the left, where the soil is not as deformed.

FIGURES

(a)
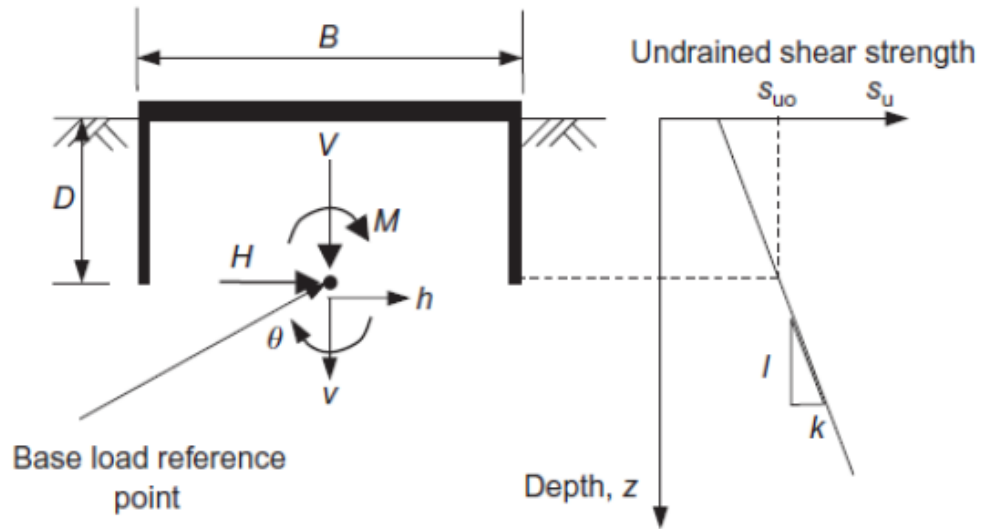
(b)
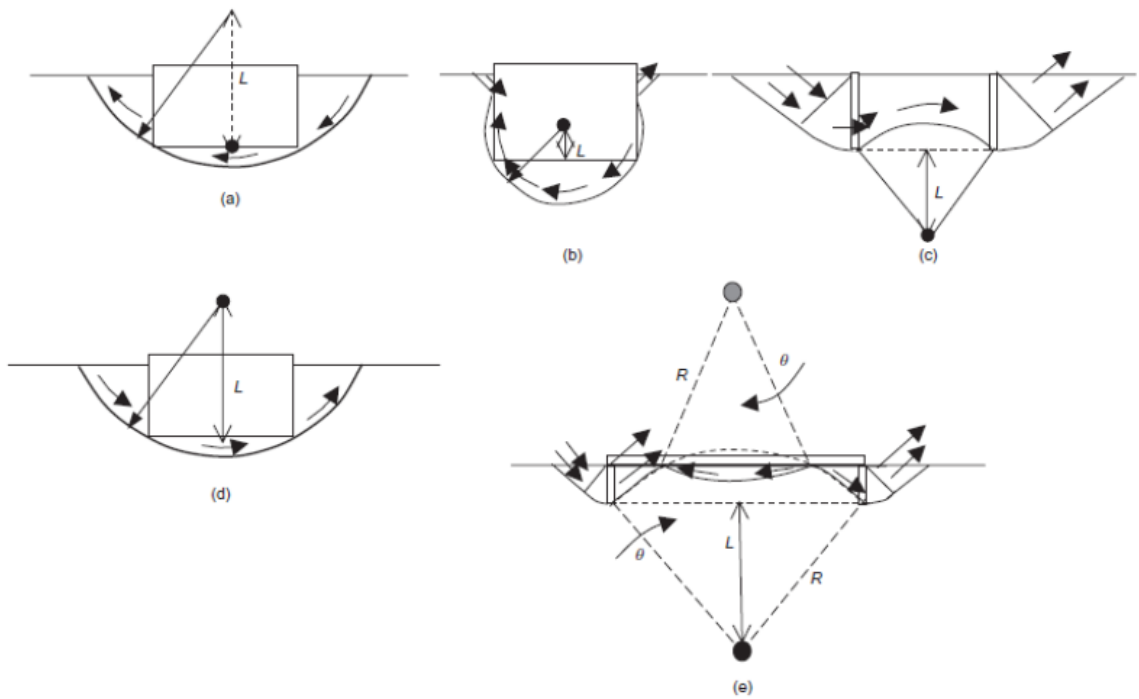
Figure 4.1 (a) *The skirted foundation examined by Bransby and Yun [2009], submitted to lateral loading **(b)** The 5 distinct soil mechanisms that can be developed by skirted foundations as recognized by Bransby and Yun [2009]: (a) "forward scoop", (b) "scoop-slide", (c) "internal*

Hansen", (d) "reverse scoop" and (e) "internal double scoop". Of these, (c) and (e) cannot be deployed by embedded foundations, where there is no internal soil to be mobilized.
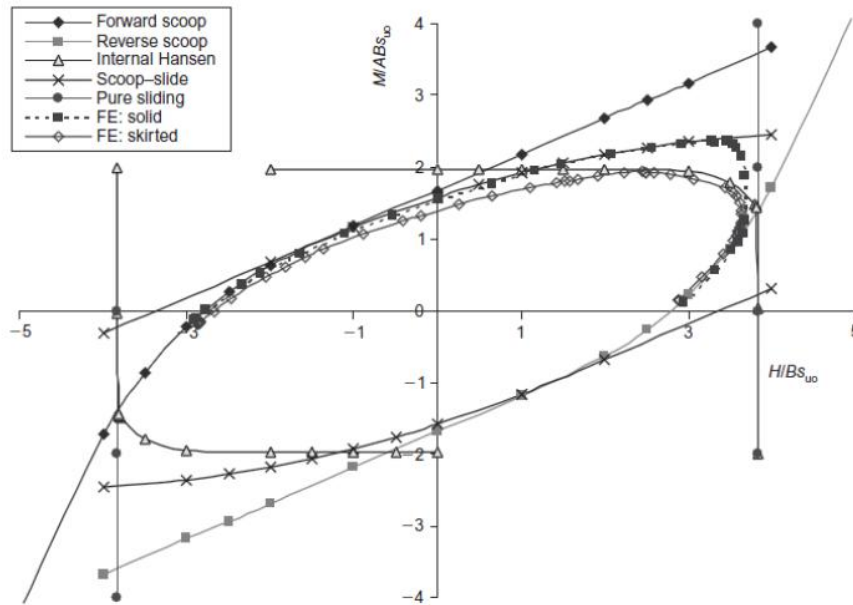
Figure 4.2 *Effective sweep of the failure envelope through upper bound plasticity analyses based on the above soil deformation patterns. [Bransby and Yun, 2009]*
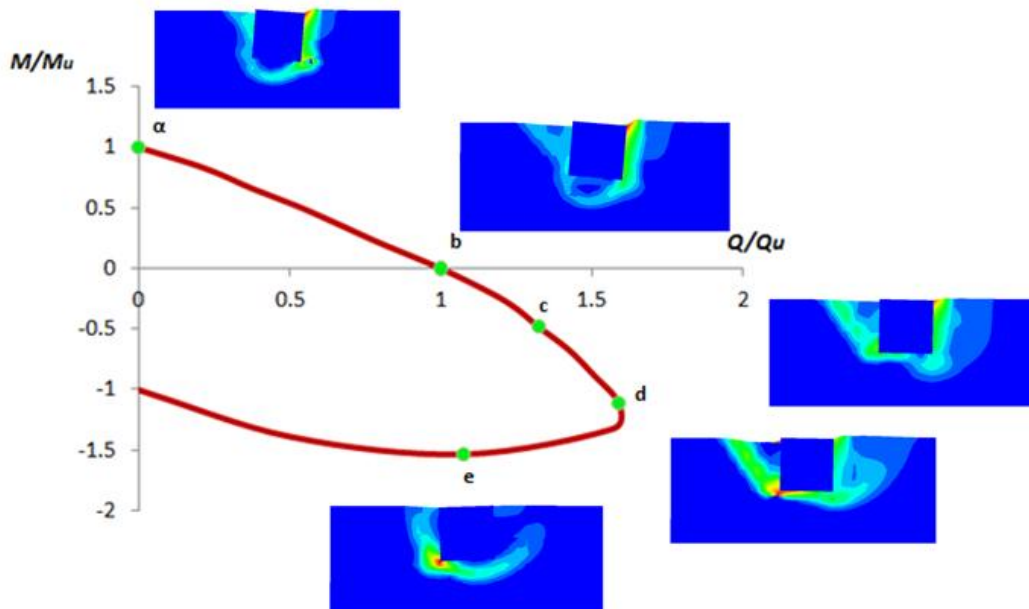
Figure 4.3 Illustration of the plastic strain magnitude contours developed at characteristic points along the yield surface for $FS_v=2$, $\mu=1$, $D/B=1$.
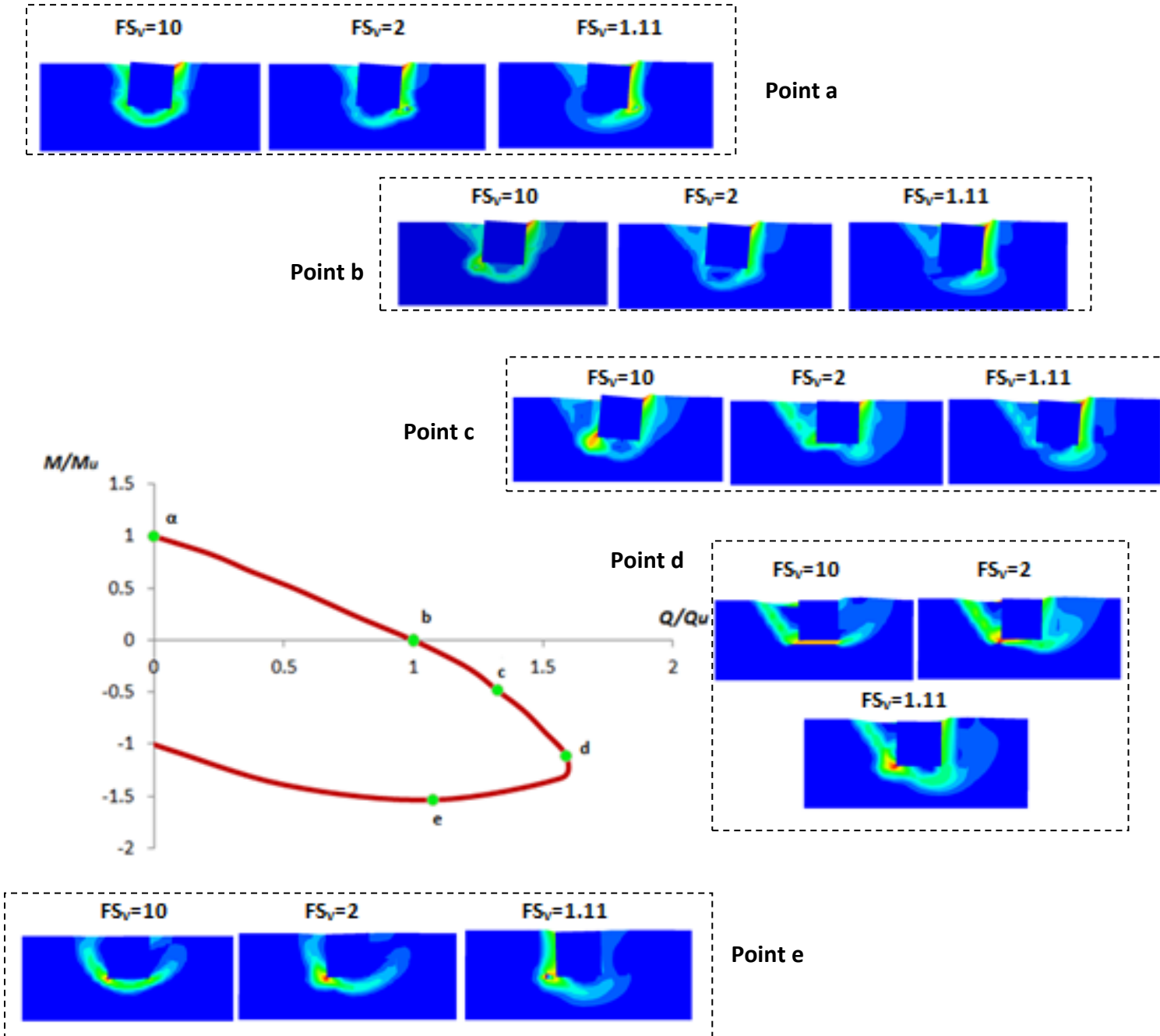
Figure 4.4 *Comparison of the plastic strain magnitude contours developed at characteristic points along the yield surface for FSᵥ=10,2 and 1.11, μ=1, D/B=1.*
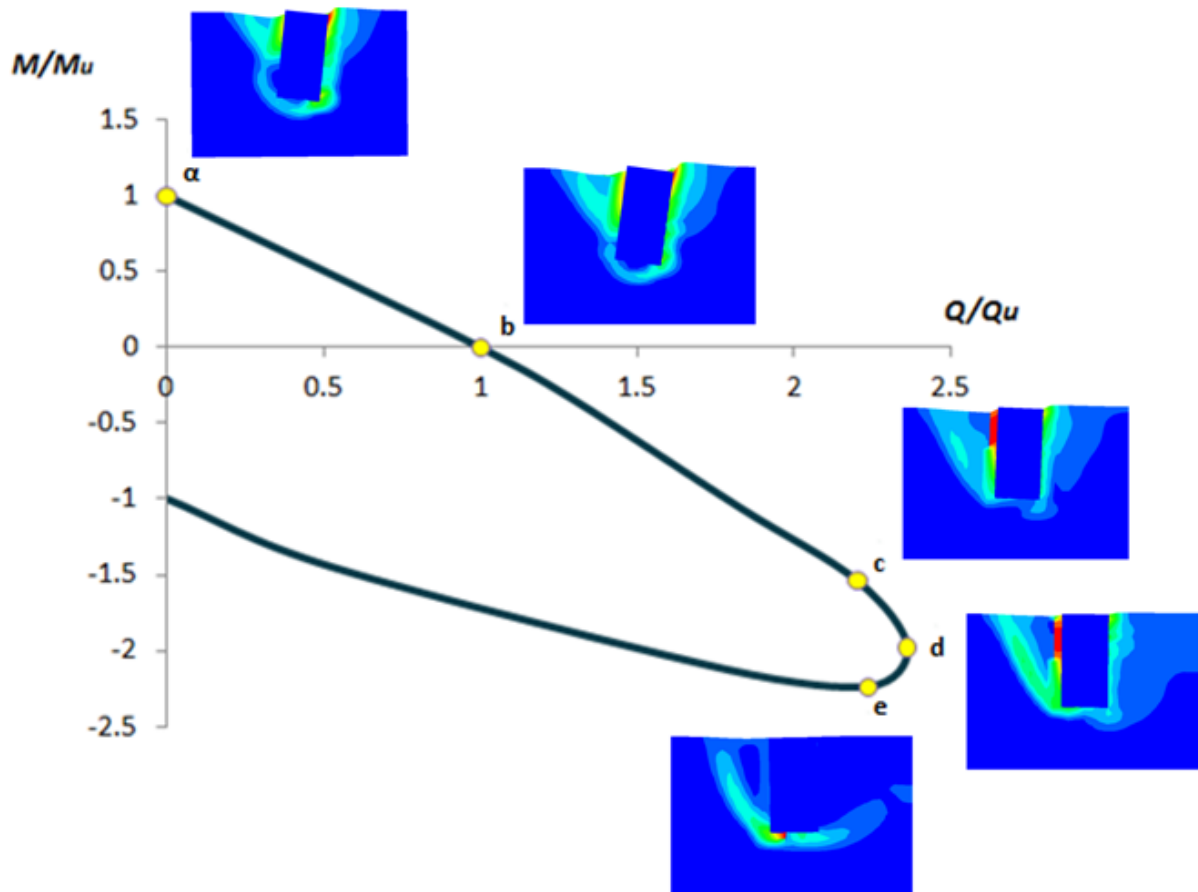
Figure 4.5 *Illustration of the plastic strain magnitude contours developed at characteristic points along the yield surface for FSᵥ=2, μ=1, D/B=2.*

Point a

Point b

Point c
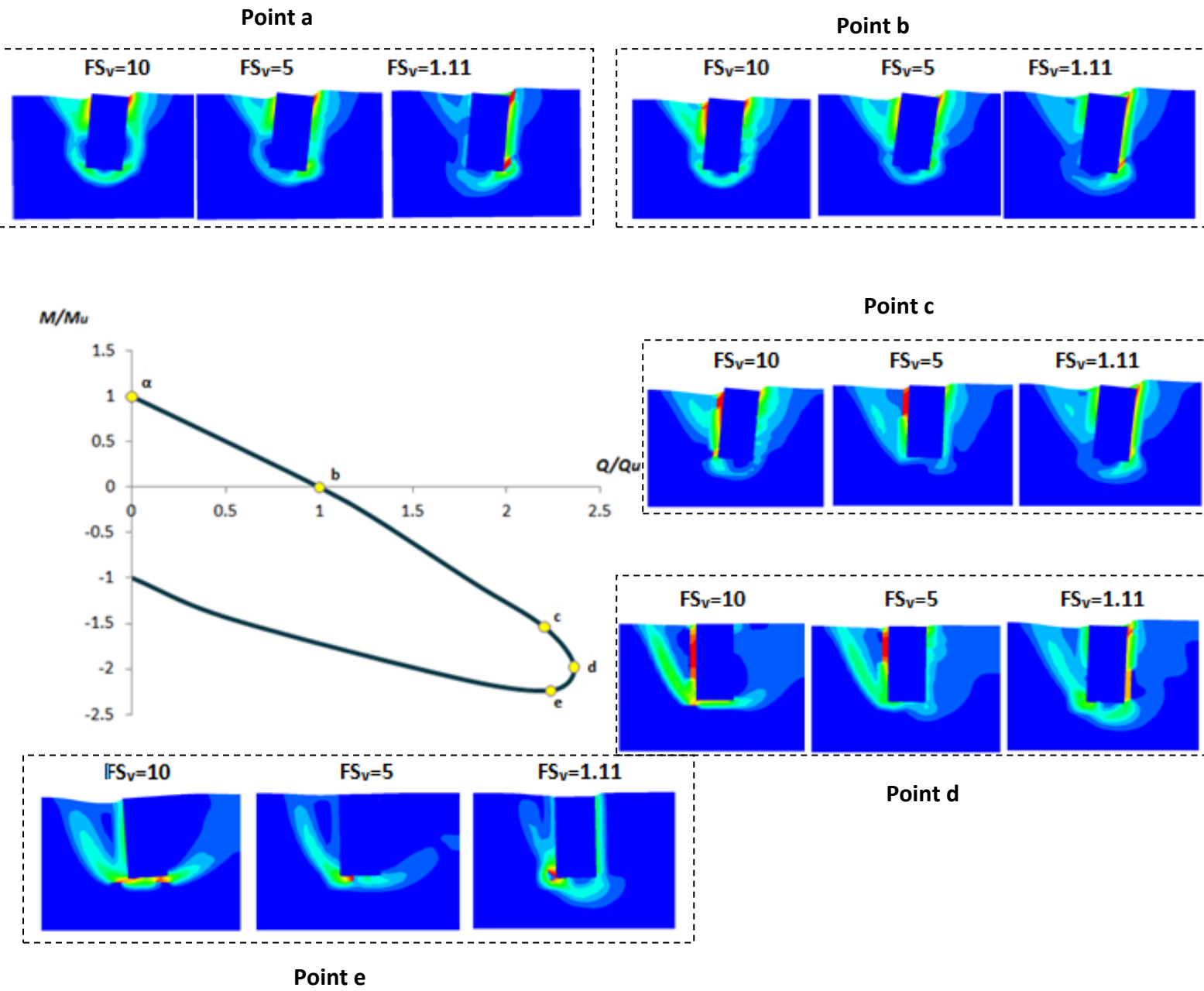
Point d

Point e

Figure 4.6 *Comparison of the plastic strain magnitude contours developed at characteristic points along the yield surface for FS_v=10,2 and 1.11, μ=1, D/B=2.*
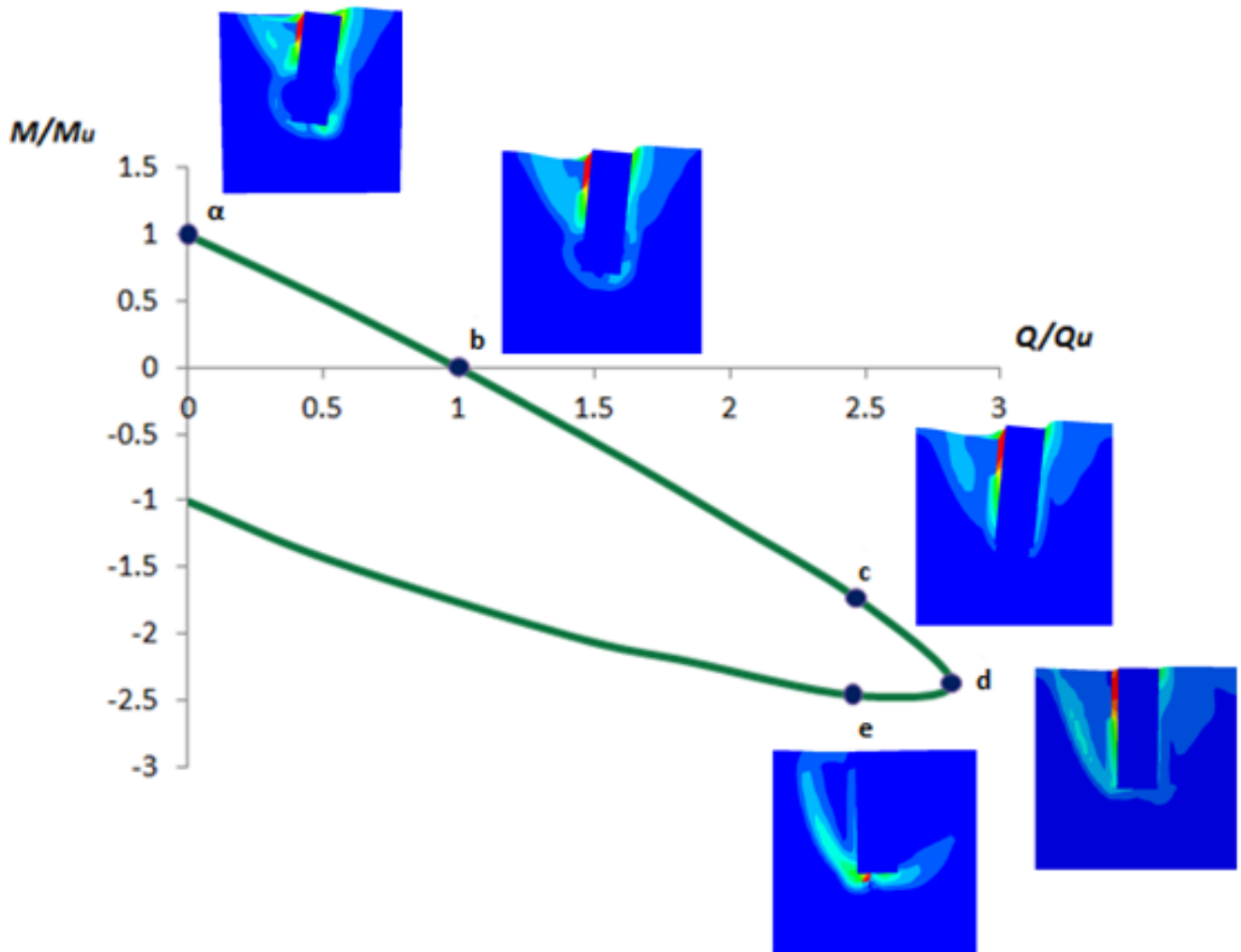
Figure 4.7 Illustration of the plastic strain magnitude contours developed at characteristic points along the yield surface for FS_v=2, μ=1, D/B=3.

Point a

Point b

Point c
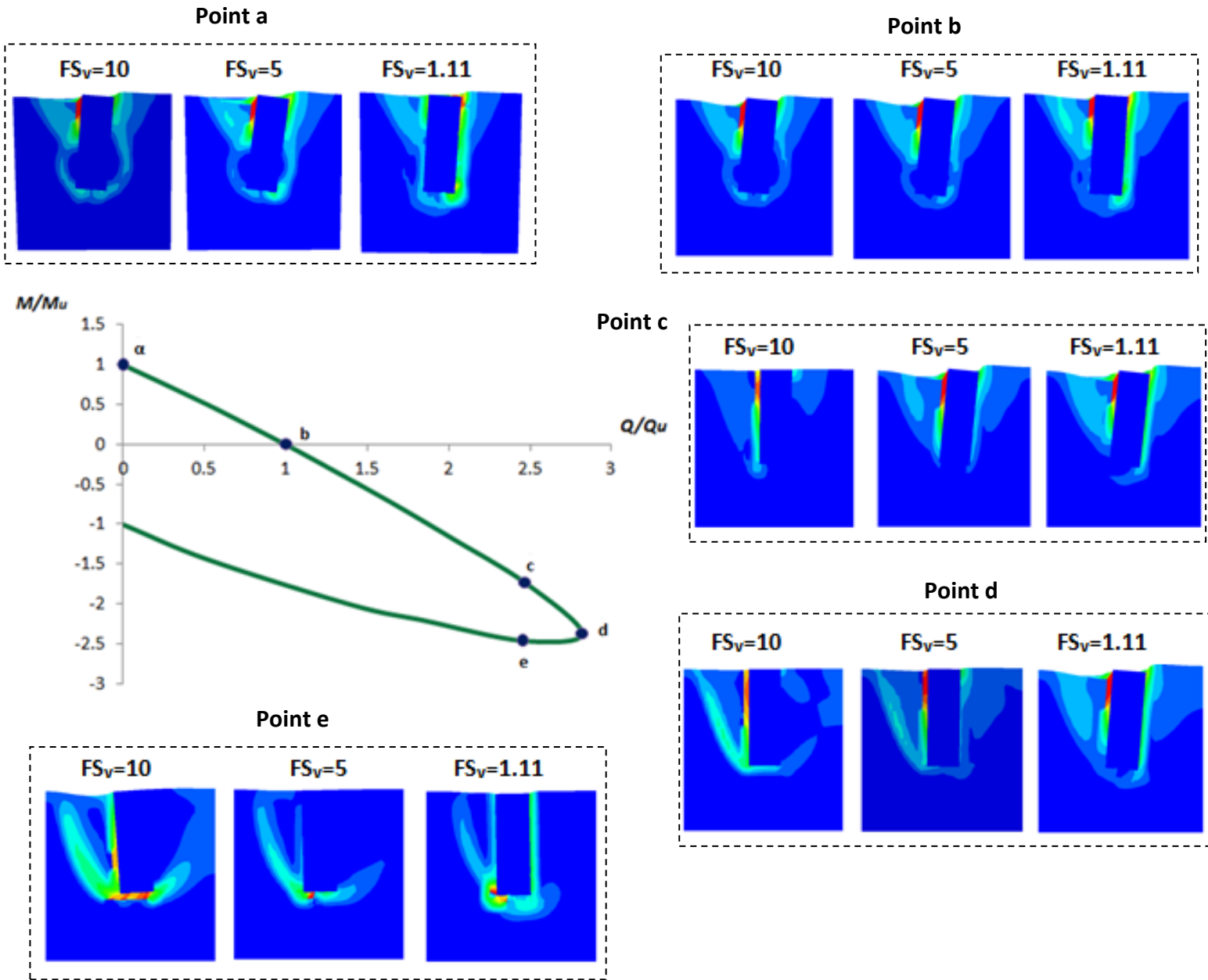
Point d

Point e

Figure 4.8 *Comparison of the plastic strain magnitude contours developed at characteristic points along the yield surface for FS$_v$=10,2 and 1.11, μ=1, D/B=3.*

Points a,a',a''

Points b,b',b''
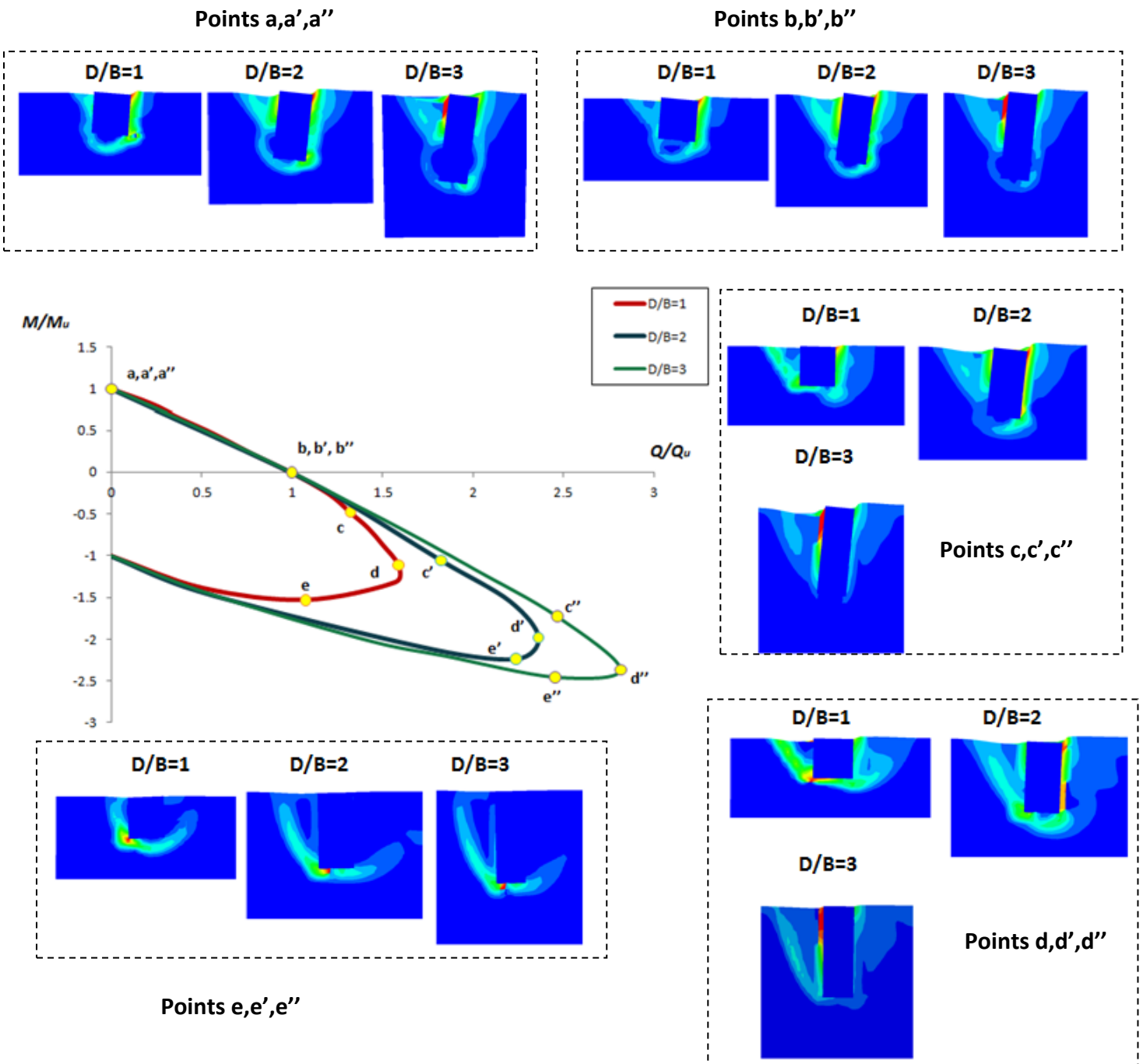
Figure 4.9 *Comparison of the plastic strain magnitude contours developed at characteristic points along the yield surface for FS$_v$=2 , µ=1 and D/B=1, 2 and 3.*

"scoop"   "scoop-slide"

"diffusive mechanism"   "slide"

"reverse scoop"
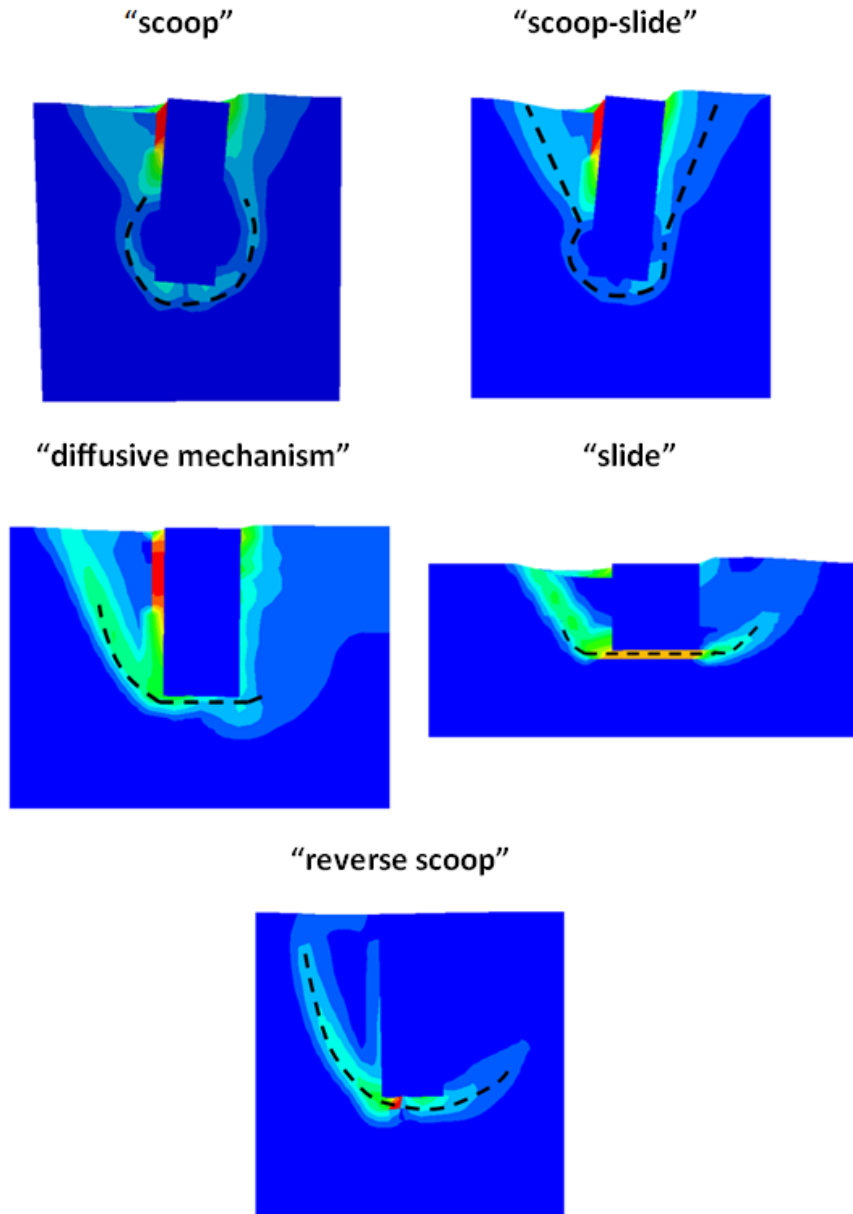
Figure 4.10 *The five distinct types of soil resisting mechanisms that are deployed by embedded foundations subject to combined M-Q loading. The "diffusive mechanism" may only be developed by deeply embedded foundations exhibiting their maximum horizontal capacity, while the "sliding mechanism" may only be developed by shallow embedded foundations exhibiting their maximum horizontal capacity as well.*
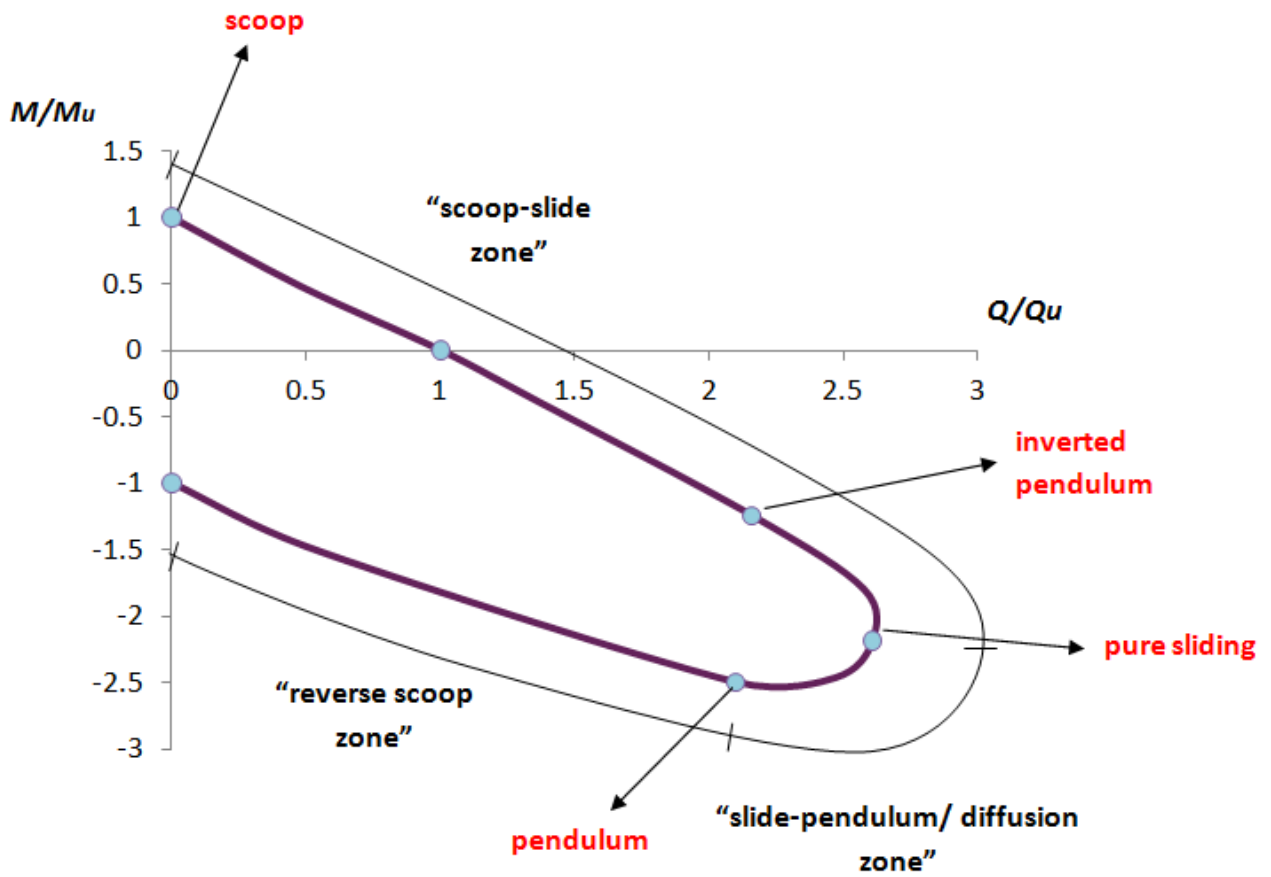
Figure 4.11 *Map of the yield surface of embedded foundations accounting for mechanism types and individual mechanisms observed.*
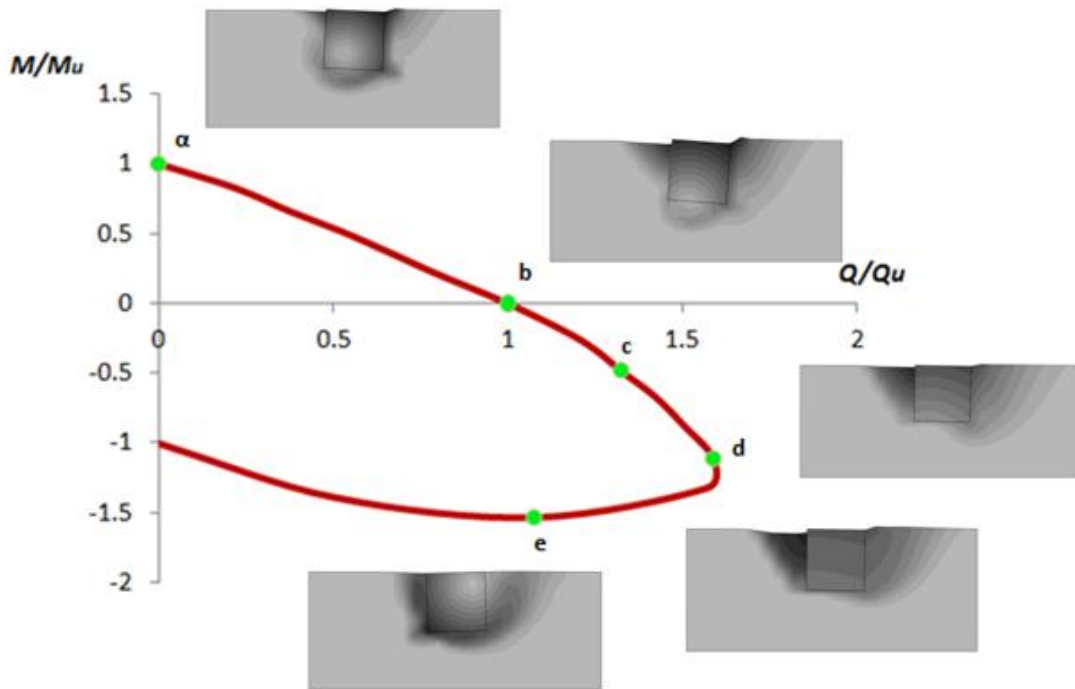
Figure 4.12 *Illustration of the caisson's pivot point along the yield surface through contours of resultant displacement for $FS_v=2$, $\mu=1$, $D/B=1$.*
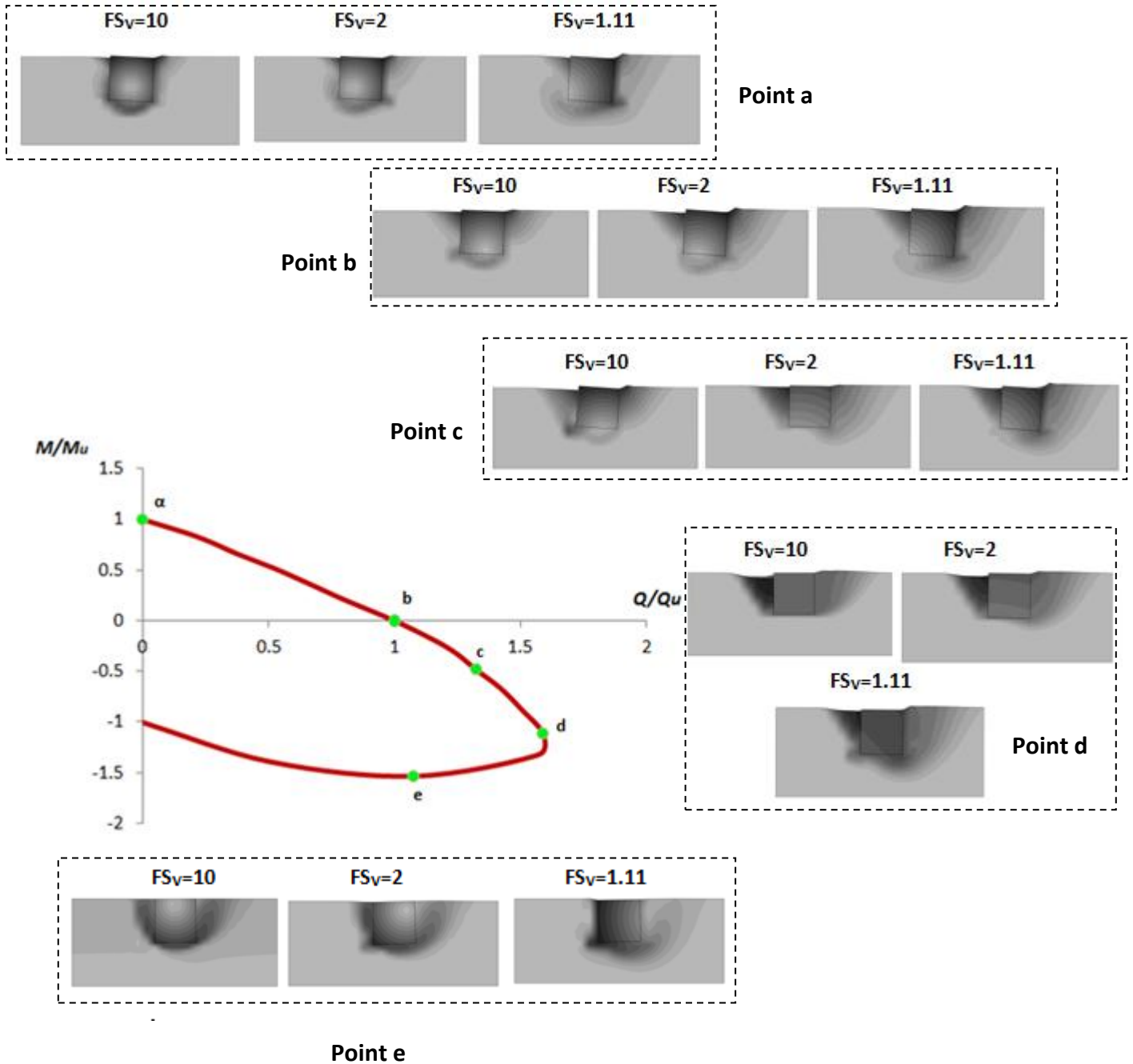
Figure 4.13 Comparison of the caisson's pivot points along the yield surface through contours of resultant displacement $FS_v=10,2$ and 1.11, $\mu=1$, D/B=1.
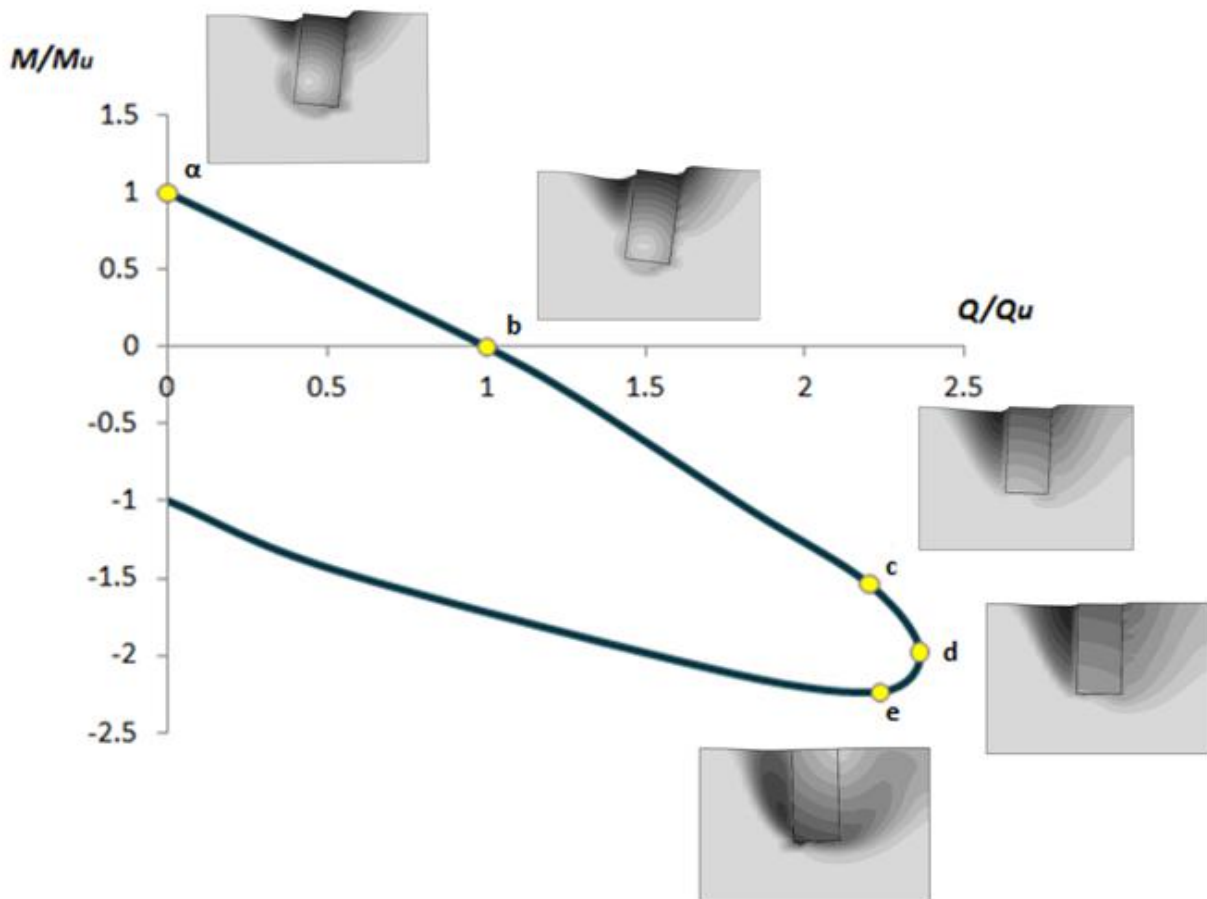
Figure 4.14 Illustration of the caisson's pivot point along the yield surface through contours of resultant displacement for $FS_v=2$, $\mu=1$, D/B=2.
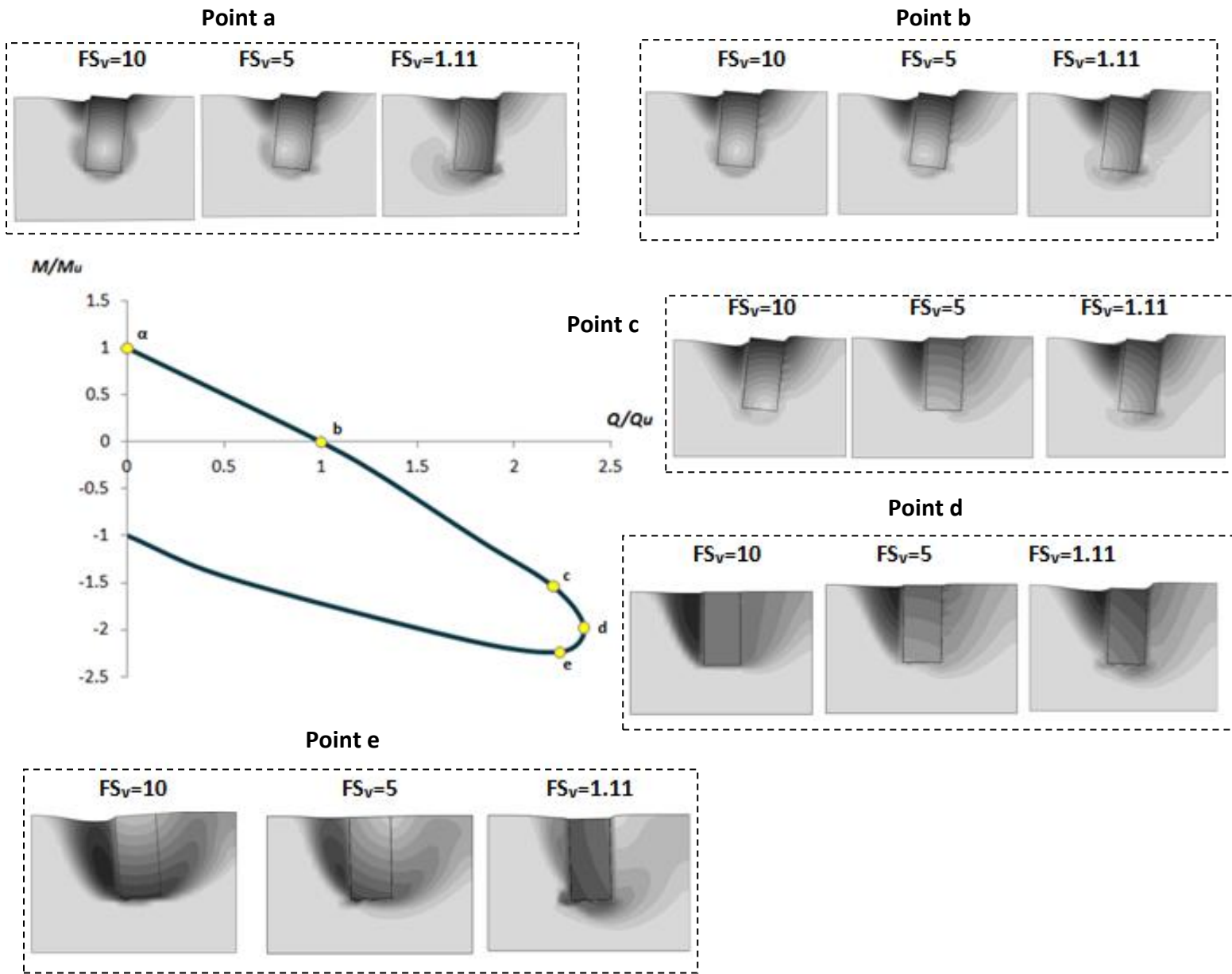
Figure 4.15 *Comparison of the caisson's pivot points along the yield surface through contours of resultant displacement for FS_v=10,2 and 1.11, μ=1, D/B=2.*
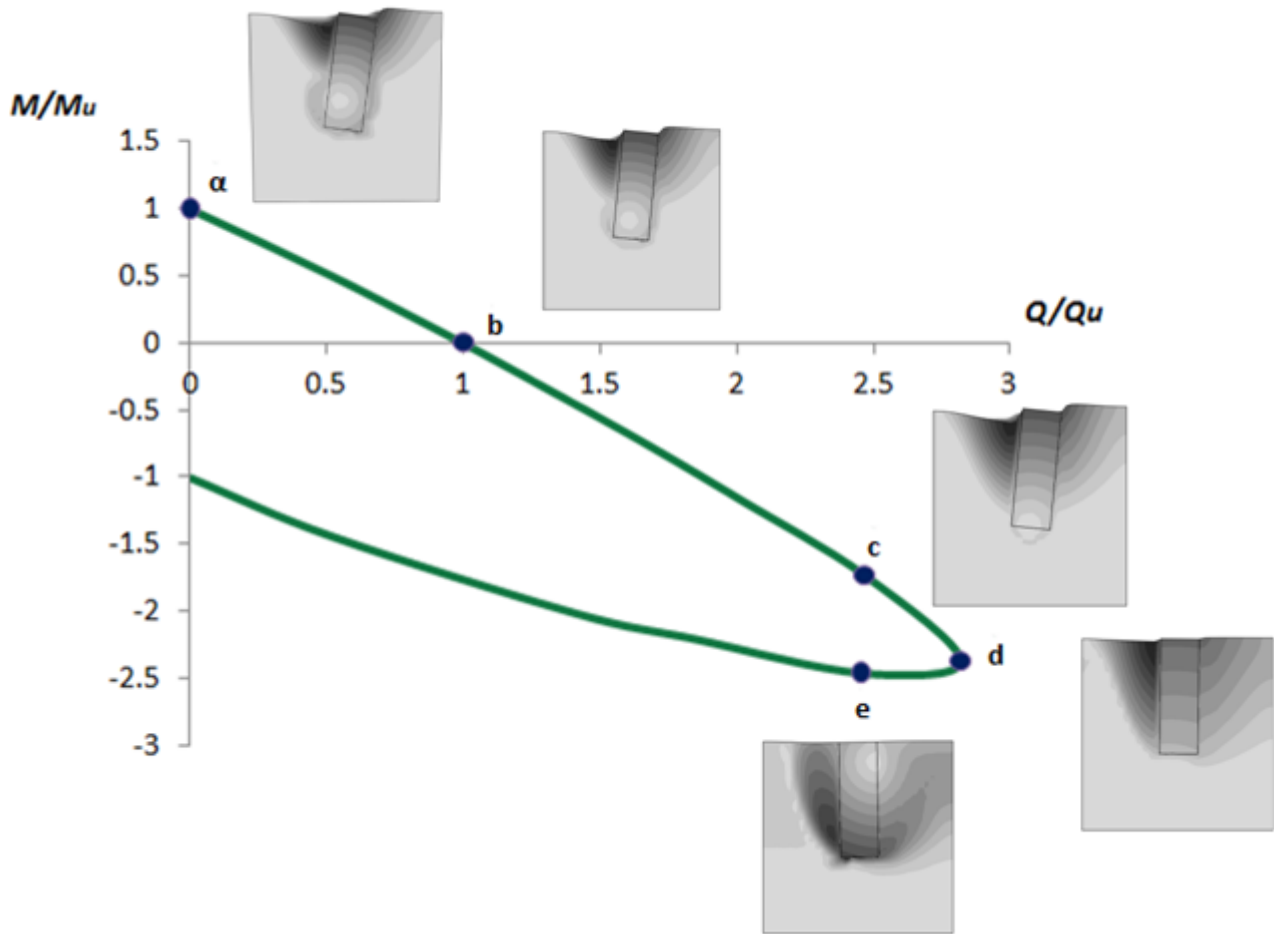
Figure 4.16 *Illustration of the caisson's pivot point along the yield surface through contours of resultant displacement for $FS_v=2$, $\mu=1$, $D/B=3$*

Point a

Point b

Point c

Point d

Point e

.
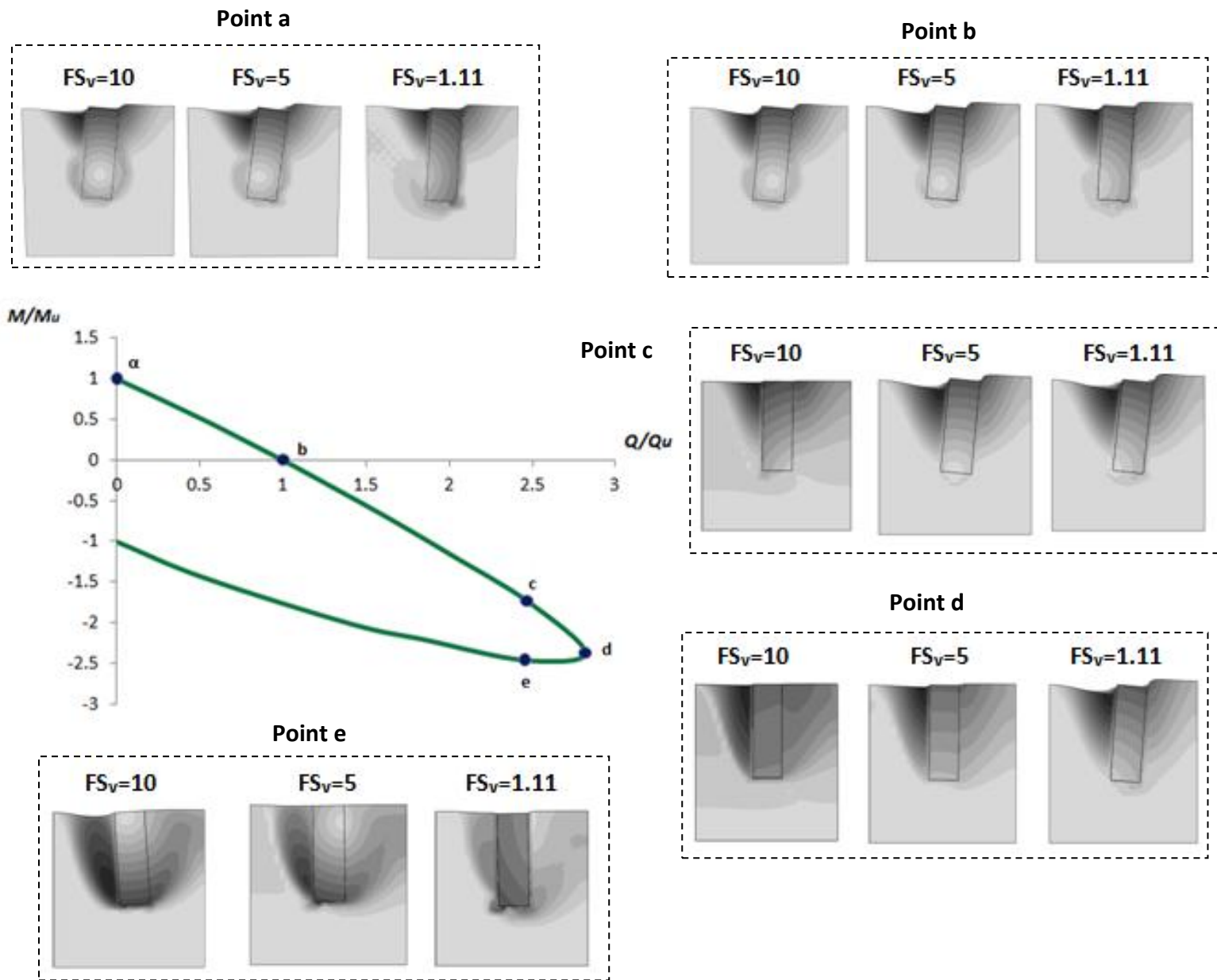
Figure 4.17 *Comparison of the caisson's pivot points along the yield surface through contours of resultant displacement for $FS_v=10,2$ and 1.11, $\mu=1$, D/B=3.*
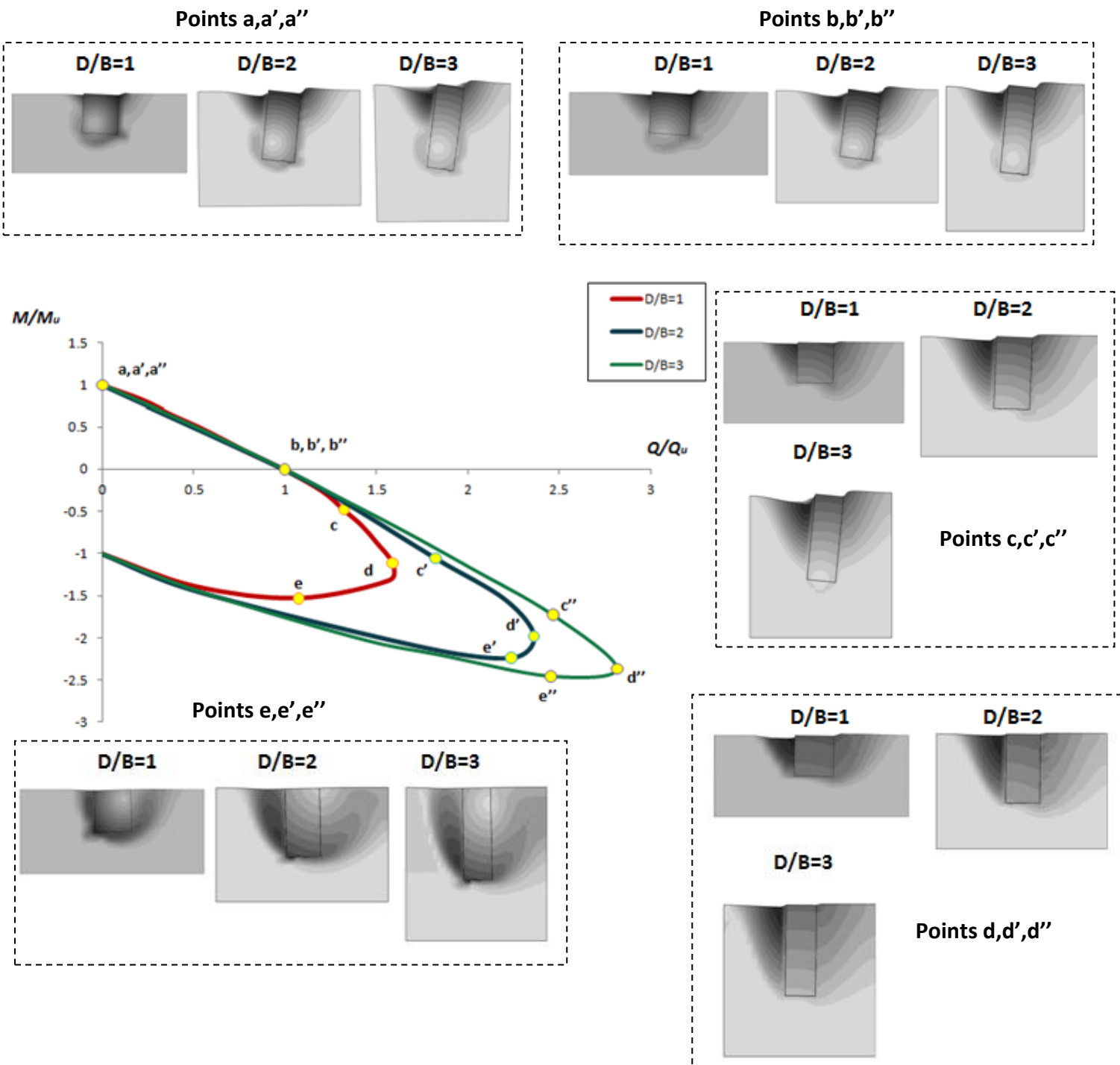
**Figure 4.18** *Comparison of the caisson's pivot points along the yield surface through contours of resultant displacement for FS$_v$=2, μ=1 and D/B=1,2 and 3.*

CHAPTER 5

ANALYTICAL EXPRESSIONS AND VALIDATION

5.1 *Introduction*

One of the goals of the herein study is the production of appropriate analytical expressions that will describe the response of deeply embedded foundations. In the last chapter, an attempt was made to thoroughly explain the mechanisms that govern caissons' behavior, without being concerned about their quantification. However, at this point of the study, it is essential to introduce mathematical expressions that can be utilized for the soil-foundation system's mathematical simulation through macro-element modeling, which will be able to reproduce the response of deeply embedded foundations under any loading conditions. Two of the main advantages of this process are : (a) the minimization of calculation time, avoiding the particularly time-consuming three-dimensional finite element analyses and (b) the immediate profit from a single mathematical tool, whose credibility lies in its ability to accurately reproduce the behavior of the herein studied foundations both at very small strain (quasi elastic behavior) and at failure. Additionally, approaching the problem from a modeling point of view can establish a better communication between geotechnical and structural engineers. Provided geotechnical engineers manage to express the response of deeply embedded foundations in terms of

"force-displacement", structural engineers will be able to acquire a much more realistic foundation behavior during non-linear incremental structural analyses *[Martin and Houlsby 2000]*. An essential prerequisite for the appropriate utilization of the aforementioned advantages is the mathematical expression of the qualities manifested during the response of deeply embedded foundations (e.g. state parameters of the foundation system), while at the same time those expressions must be consistent with the physics of the particular problem as these have been identified in the herein thesis.

5.2 Ultimate Capacity

In ***Figures 5.1, 5.2*** we witness the change of ultimate horizontal capacity (Q_u) and ultimate moment capacity (M_u), normalized by their pure capacities for zero vertical load Q_u^* and M_u^*, in respect to the inverse safety factor χ for the three examined embedment ratios. It is worth noting that the two capacities demonstrate similar behavior, thus allowing us to reach the same conclusions. As we have already observed in chapter 3 both lateral capacities are influenced by the inverse factor of safety χ, the coefficient of friction μ and the embedment ratio D/B.

After the appropriate processing of the data that derived from the three-dimensional finite element analyses, the following analytical expressions were formed to fit these numerical results and calculate the ultimate capacities of deeply embedded foundations:

$$\frac{Q_u}{Q_u^*} = (a_Q \chi^2 + \beta_Q \chi + 1)^{\delta_Q} (1 - \chi)^{\varepsilon_Q} \qquad \text{(5.1)}$$

$$\frac{M_u}{M_u^*} = (a_M \chi^2 + \beta_M \chi + 1)^{\delta_M} (1 - \chi)^{\varepsilon_M} \tag{5.2}$$

where $a_Q, \beta_Q, \delta_Q, \varepsilon_Q$ and $a_M, \beta_M, \delta_M, \varepsilon_M$ are all dependent on the coefficient of friction μ and the embedment ratio D/B. However, a clear trend is not evident for these quantities in the results of numerical analyses, as far as μ and D/B are concerned. Producing analytical expressions for these variables in order to take account of the effect of slippage and embedment would be possible but it would defy the purposes of this thesis, since these expressions would be very elaborate and difficult to use. Instead, we provide charts that demonstrate the change of these parameters in respect to the embedment ratio D/B and the coefficient of friction μ (*Figures 5.3, 5.4).*

Furthermore, it is evident that in order to utilize these expressions, one needs the values of the pure ultimate lateral capacities under zero vertical load, Q_u* and M_u* respectively. Providing analytical expressions for these quantities would not be prudent for the case of cohesionless soils, since we do not have enough data to produce useful expressions. More specifically, we run numerical analyses for three embedment ratios D/B (1, 2 and 3) but for only one width (B=10m). However, in the case of cohesionless soils, where the scale effect is of great importance, it is not possible to generalize results that have derived from a foundation of specific geometrical characteristics. To determine the exact expression of the capacities under zero vertical load we would need data from numerical analyses concerning at least two more different geometries.

It should be noted that for the same reasons mentioned above, we do not attempt to provide an analytical expression for the ultimate vertical load that can be undertaken by the foundation, N_u.

In **Figures 5.5** and **5.6** the numerical data are compared to the analytical expression for different coefficients of friction and embedment ratios both for the horizontal load and the moment capacity, and the fit proves to be very satisfactory in every case.

5.3 *Yield equation for the soil-caisson system*

5.3.1. Literature

Scientific research concerning different types of embedded foundations have shown that the shape of the yield surface of the soil-foundation system can be described by an oblique ellipse in the M-Q space [*Bransby and Randolph 1999a; Martin and Houlsby 2001; Yun and Bransby 2007*]. For instance, Yun and Bransby [*2007*], have proposed the following equation representing the yield locus of lightly embedded foundations (D/B ≤ 1) :

$$(\frac{H}{H_{max}})^2 + (\frac{M^*}{M_0})^2 = 1 \qquad (5.3)$$

where:

- H, H_{max} are the applied and the maximum horizontal force for the foundation respectively
- M^*, M_0 are the applied moment and the pure moment capacity of the foundation

Through an optimization technique, Gerolymos and Souliotis [*2012]*   have concluded that the following form of equation most accurately represents the failure envelope of a foundation embedded in cohesive soil with bonded interface:

$$f = (\frac{Q}{Q_u})^2 + (\frac{M}{M_u})^2 + n_3 \left(\frac{Q}{Q_u}\right) \left(\frac{M}{M_u}\right) - 1 = 0 \qquad \text{(5.4)}$$

where n_3 is a function of the embedment ratio capturing the expansion of the curve and is given by:

$$n_3 = 1.84 - 0.21(\frac{D}{B})^{-1.98} \qquad \text{(5.5)}$$

Respectively, Gerolymos and Karapiperis [*2012]* proposed the following equation for embedded foundations in cohesive soil considering the non-linearity of the interface:

$$f = (\frac{Q}{Q_u})^{n_1} + (\frac{M}{M_u})^{n_2} + n_3 \left(\frac{Q}{Q_u}\right) \left(\frac{M}{M_u}\right) - 1 = 0 \qquad \text{(5.6)}$$

where parameters n_1, n_2 control the yield locus's rotation (introduced by the detachment of the caisson from the soil) and n_3 controls the yield locus's expansion, both in respect to the embedment ratio *D/B*.

The following expressions were deduced for the above parameters:

$$n_1 = 2 - 0.25(\frac{D}{B})^{-2.06} \qquad \text{(5.7)}$$

$$n_2 = 2 + 0.1(\frac{D}{B})^{-1.135} \qquad (5.8)$$

$$n_3 = 1.891 - 0.386(\frac{D}{B})^{-2.361} \qquad (5.9)$$

5.3.2. Proposed analytical expression

As previously stated in the herein thesis, for cohesionless soils the effect of the coefficient of friction μ and the safety factor FS_v cannot be disregarded as it has been for cohesive soils in the aforementioned studies. Therefore, we suggest that the shape of the envelope is affected by the embedment ratio D/B, the safety factor FS_v and the coefficient of friction μ. In order to capture the effect of those parameters on the yield surface, expression **5.6** was given as input in an optimization procedure:

$$f = (\frac{Q}{Q_u})^{n_1} + (\frac{M}{M_u})^{n_2} + n_3 \left(\frac{Q}{Q_u}\right)\left(\frac{M}{M_u}\right) - 1 = 0 \qquad (5.6)$$

The highly nonlinear nature of the parameters n_1, n_2 and n_3 with respect to μ, *FSV* and *D/B* left no option but to train appropriate neural networks, as will be displayed in the next section.

5.3.3. Neural Networks

5.3.3.1. Theoretical basis

A neural network is a mathematical model inspired by biological neural networks and is generally used to recognize patterns in data. Such a network consists of at least three layers: *(a)* the *input layer* that receives input data in the form of a matrix and passes the information to the network for processing, *(b)* the *hidden layer* which is a layer of neurons that receives information from the input layer and processes it in a hidden way to the posterior hidden layer or to the out layer, and *(c)* the *output layer* that receives processed information and produces the response of the system.

Each layer has a weight matrix, *w*, a bias vector, *b,* and an output vector, *y.* Each element of the input vector, *x,* is connected to each neuron input through the weight matrix, *w.* The neuron output, *o,* is a scalar number; it is a nonlinear function (known as the *transfer* or "*activation*" function) of the sum of the outputs of all neurons in the most anterior layer (the neuron input net):

$$o_j\left(net_j\right) = f\left(\sum_i w_{ij}\, x_i + b_j\right) \qquad (5.10)$$

The effectiveness of a neural network to simulate highly non−linear problems is partially attributed to the transfer function used for processing the output of a neuron.

There are several types of transfer functions, the appropriate choice of which depends strongly on the nature of the problem and the type of employed neural network.

In our case, the powerful hyperbolic tangent was utilized as a transfer function together with a back-propagation learning rule.

Supplying the neural network with sufficient input data, the former is trained by repeatedly applying as much as 75% of the input data and calculating errors with respect to the difference between the target and the output vectors. The weight and bias of each neuron in the network is then updated with the learning rule after each training cycle / "epoch". This procedure is repeated until the network error falls beneath an error goal, or a maximum number of epochs have occurred.

After the training, the neural network is validated and tested for the remaining 25% of the data. In this step, the network's ability to capture the existing patterns and generalize for new input data is confirmed. Besides the above validation, the efficiency of the network is about to be tested as part of the whole model.

5.3.3.2. Representation of parameters n_1, n_2, n_3

The highly nonlinear nature of the hardening parameters n_1, n_2 and n_3 renders it extremely difficult to deduce analytical expressions that can accurately fit the numerical data. Hence, we are led to train three separate neural networks for each variable. Using Matlab's neural networking tool, we supply a sufficiently large number of data and test the network's ability to capture the basic hardening trends as well as generalize. The basic architecture of the multilayer neural network developed is shown in *Figure 5.7.* The input data involve the embedment ratio D/B, the factor of safety against vertical loading FS_v and the coefficient of friction μ, while the output is of course one of the parameters for each network. The "hidden" layer of the network consists of three neurons and the output layer

of one neuron, while the hyperbolic tangent function is used as the "activation" function for all neurons:

$$n_k = \tanh\left[\sum_{j}^{3} w2_j \, tanh\left(\sum_{i}^{3} w1_{i,j} x_i + b1_j\right) + b2\right] \qquad \textbf{(5.11)}$$

where $k=1,2$ or 3, $w1_{ij}$ and $b1_j$ are the weights and biases of the hidden layer (i representing the number of the input parameters and j the number of neurons) and $w2_j$ and $b2$ are the weights and biases of the output layer.

In **Figure 5.8**, the weights and the biases of the hidden layer ($w1_{ij}$ and $b1_j$) as well as the weights and the biases of the output layer ($w2_j$ and $b2$) are provided for every variable separately. In **Figure 5.9** we attempt to compare the results from the neural networks to the results from the optimization of the data that derived from the three dimensional finite element analyses for **a)** parameter n_1 **b)** parameter n_2 and **c)** parameter n_3. Evidently, the neural network approach is fairly satisfactory with the greatest deviation from the analytical results being 4% for parameter n_2, which implies that the network managed to recognize the majority of the patterns lying behind the values of the parameters.

After determining these parameters we attempt to validate our results by comparing the failure envelopes produced by the proposed analytical fit to the ones that derived from the finite element analyses. In **Figures 5.10** through **5.14** we contrast the data derived from the numerical experiments (points) and the analytical expression proposed for the yield surfaces of caisson foundations for different factors of safety, coefficients of friction and embedment ratios. Evidently, the fit proves to be satisfactory in every case.

FIGURES

(a)

(b)
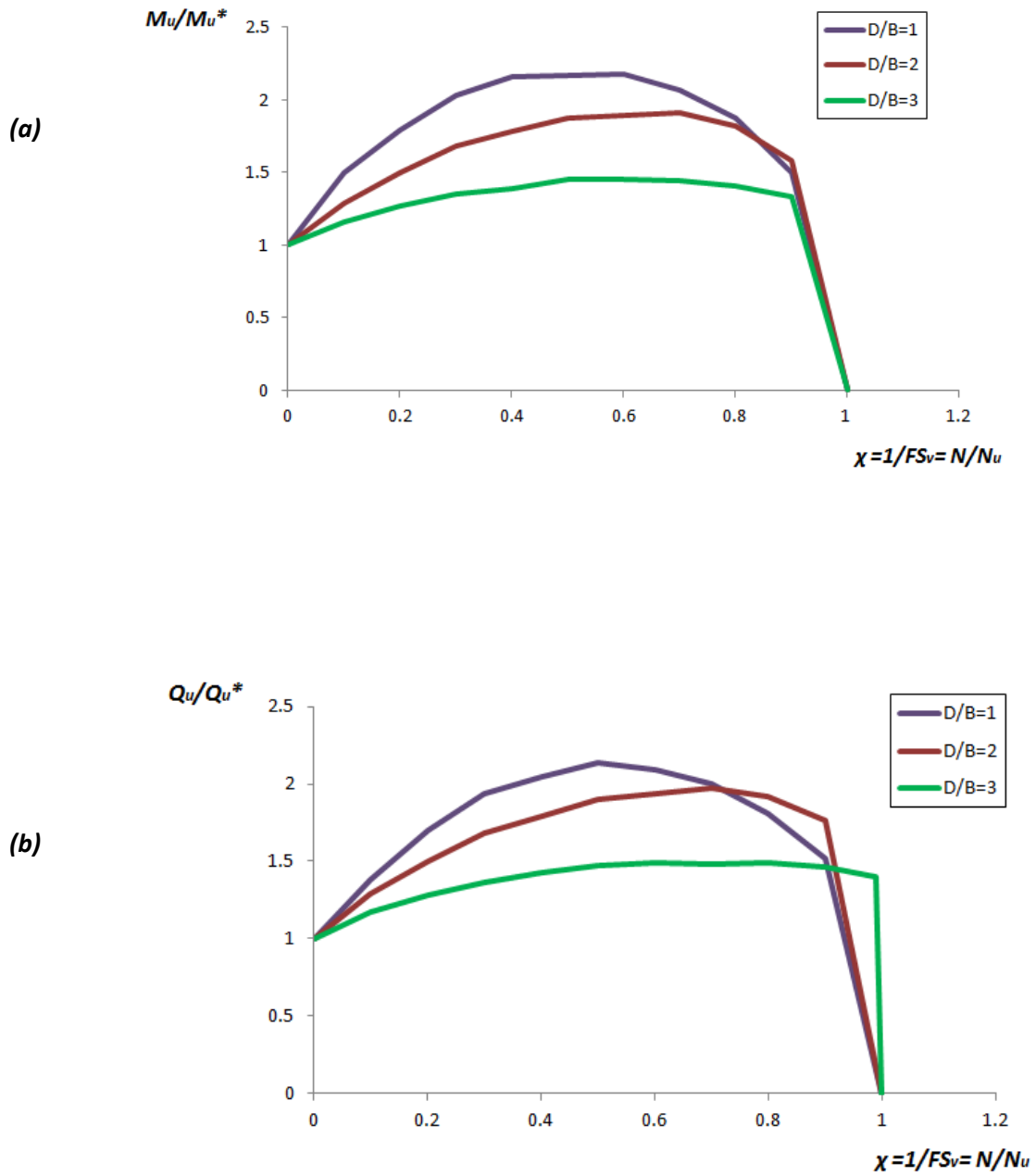
Figure 5.1 *Comparison of the normalized ultimate **(α)** moment and **(b)** horizontal capacities for μ=1 and D/B=1, 2 and 3.*
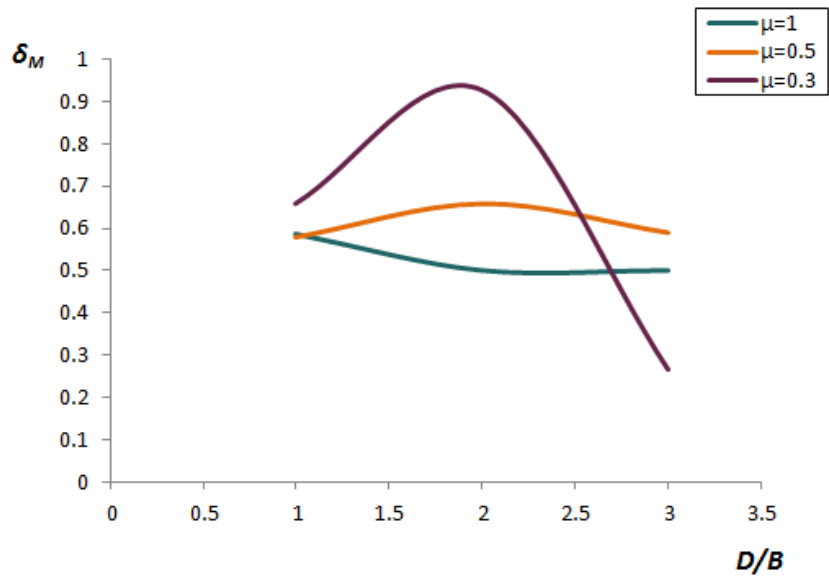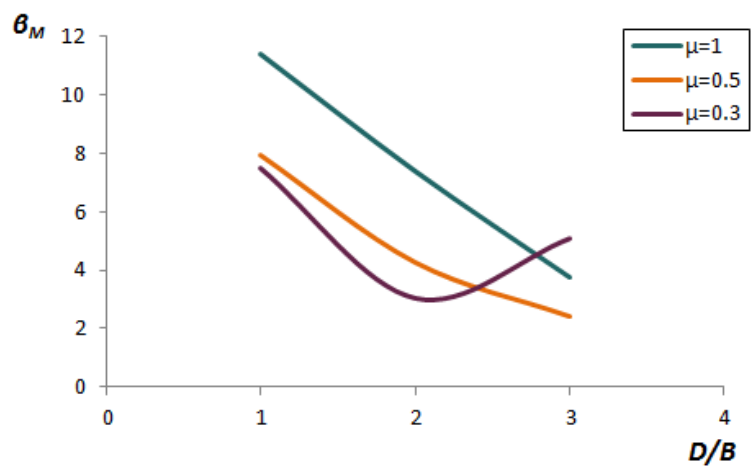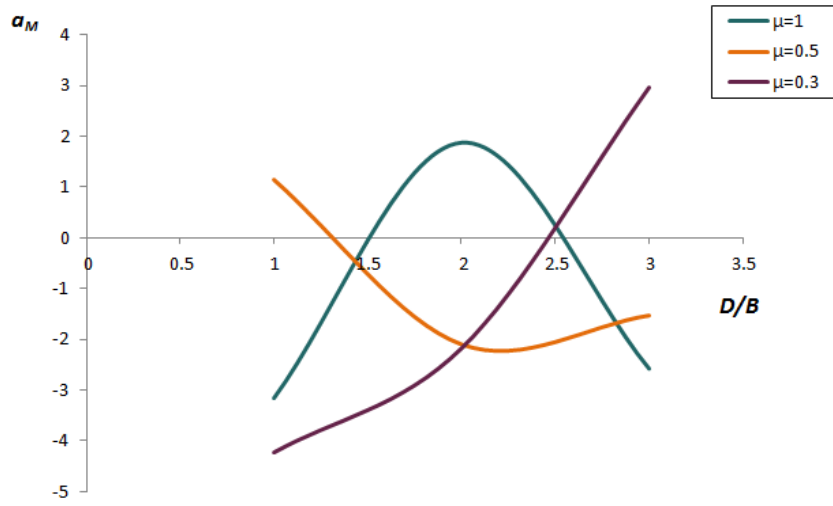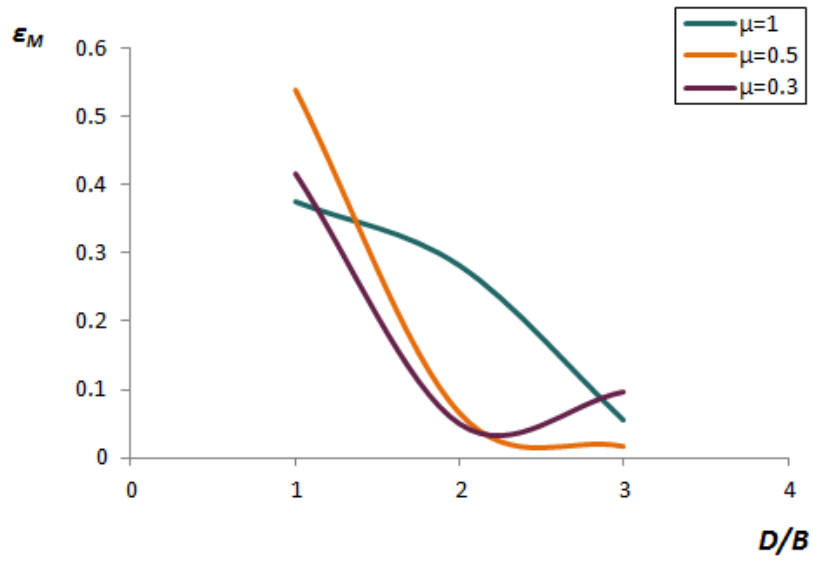
**Figure 5.3** *Charts of parameters a_M, β_M, δ_M and ε_M (variables employed for the analytical expression of the caisson's moment capacity) in respect to the embedment ratio D/B for different coefficients of friction µ=1, 0.5, 0.3.*
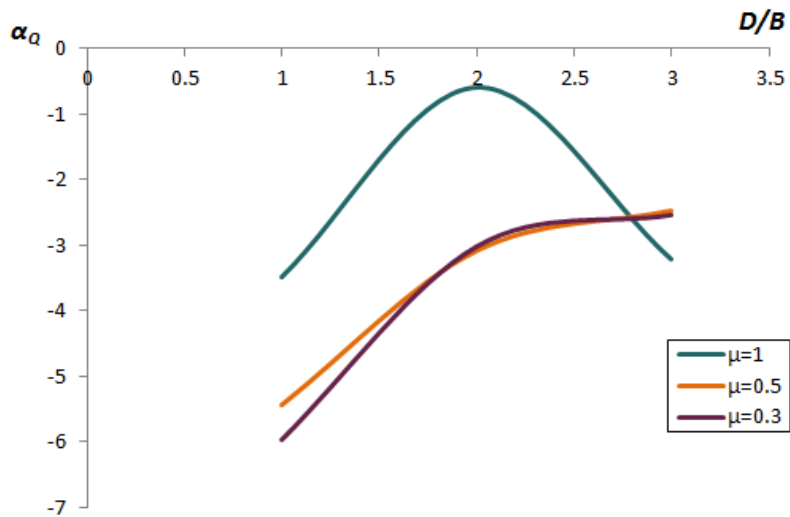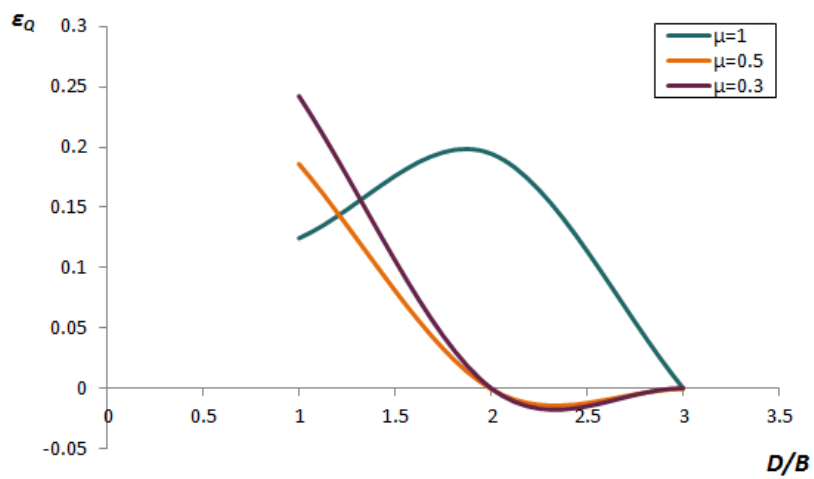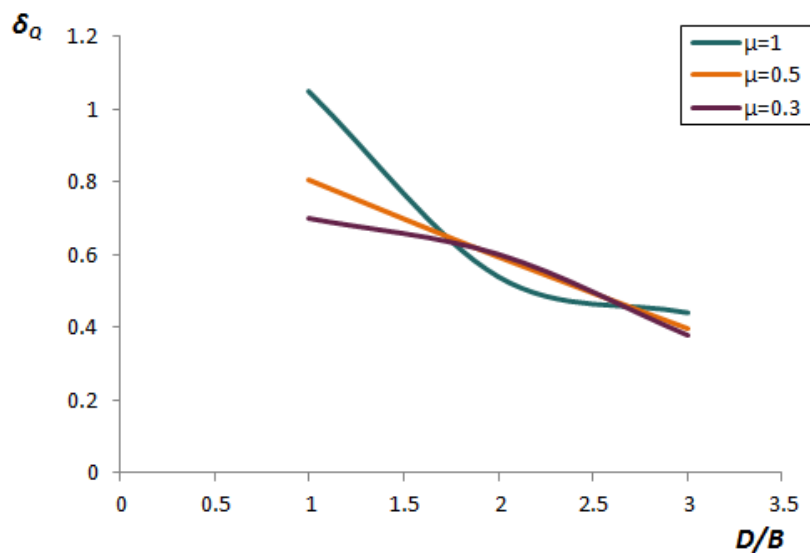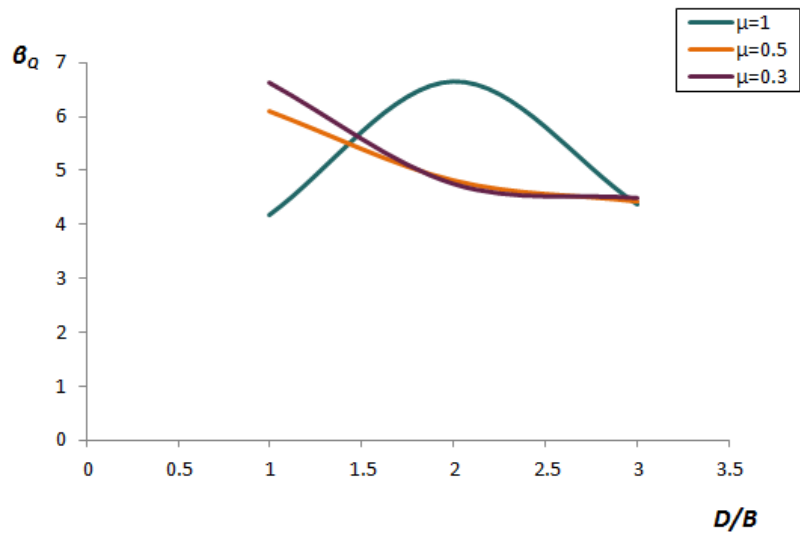
Figure 5.4 *Charts of parameters a_Q, β_Q, δ_Q and ε_Q (variables employed for the analytical expression of the caisson's horizontal capacity) in respect to the embedment ratio D/B for different coefficients of friction μ=1, 0.5, 0.3*

a)

b)

c)
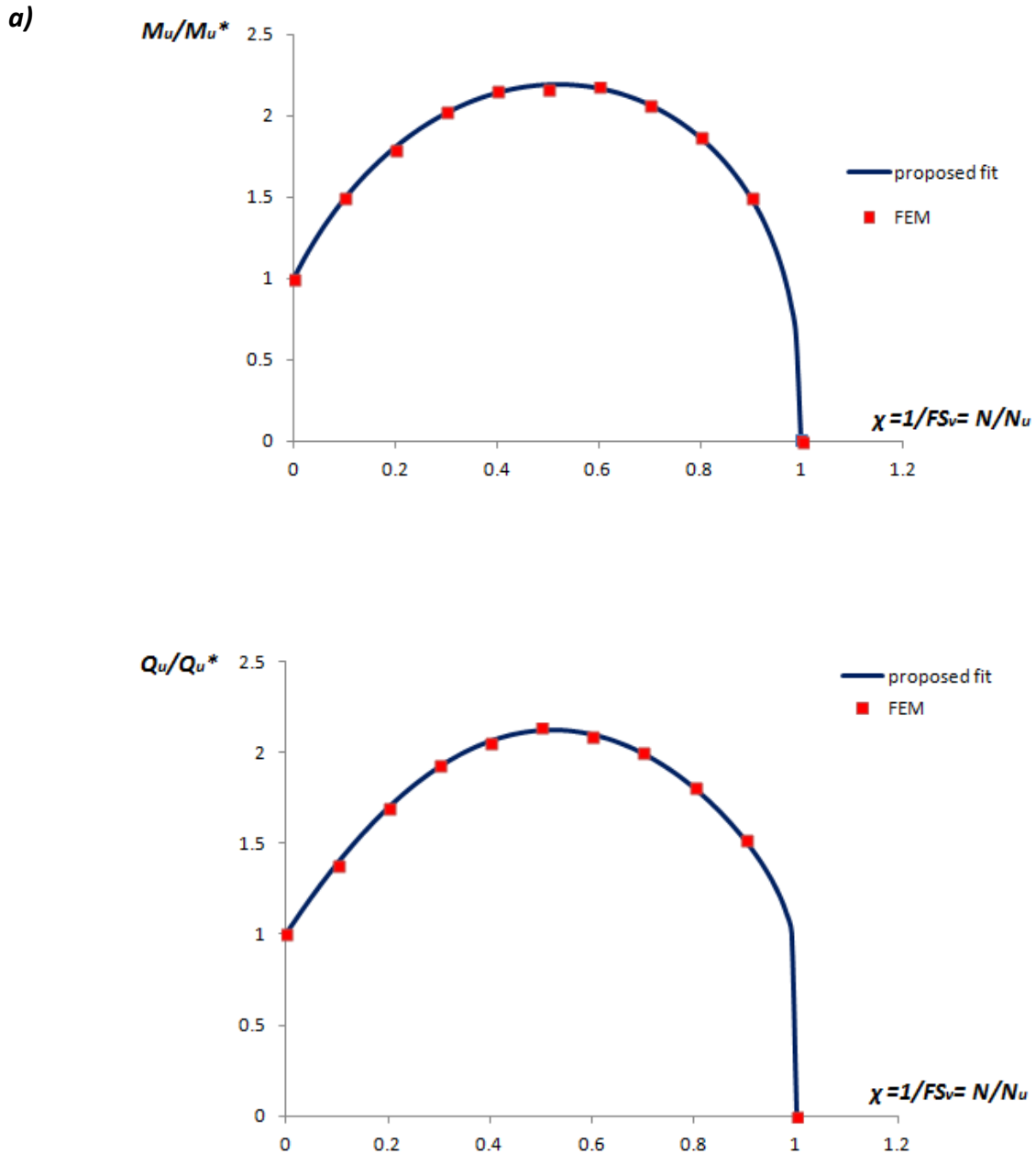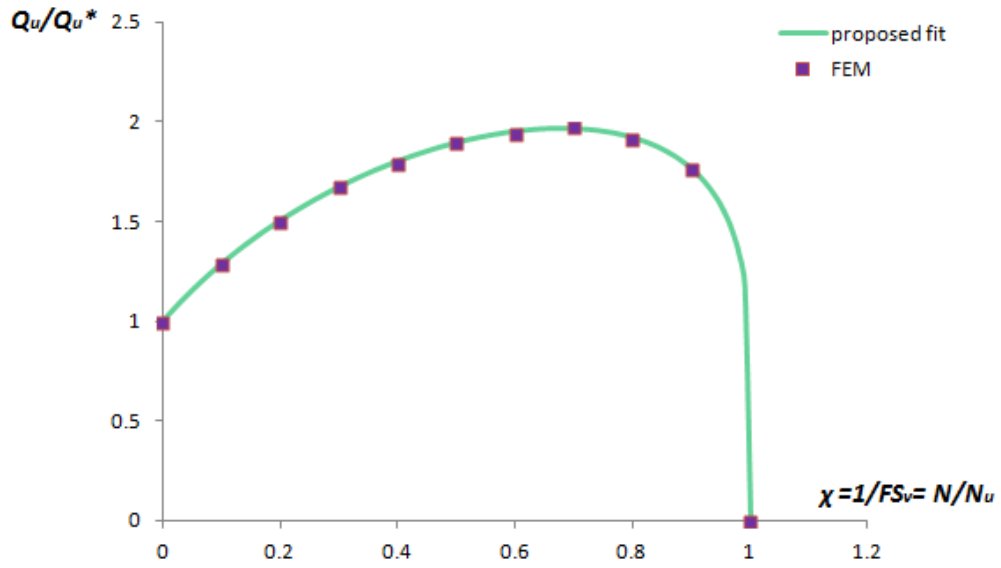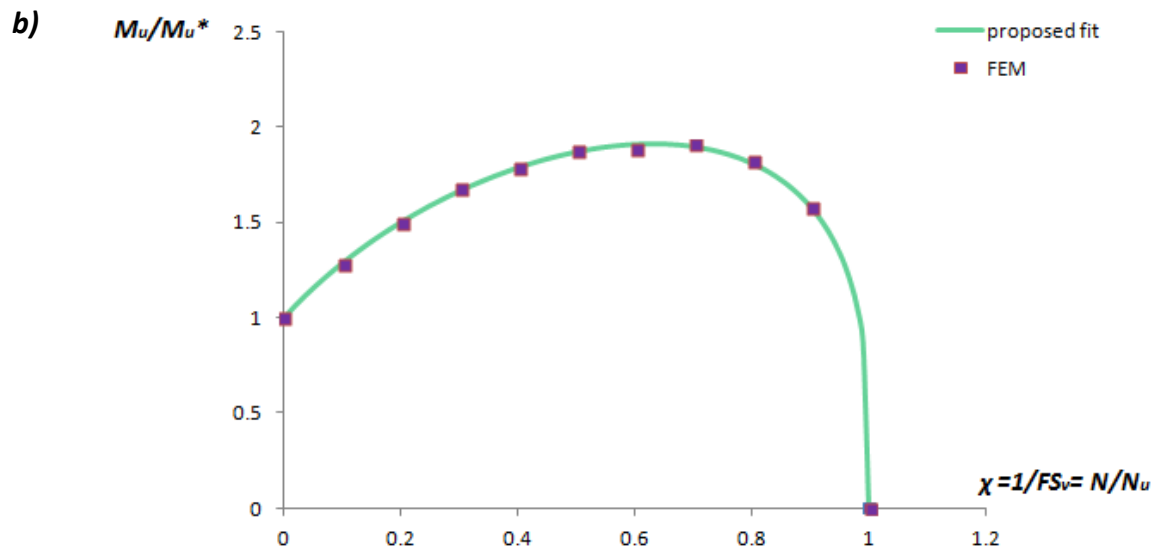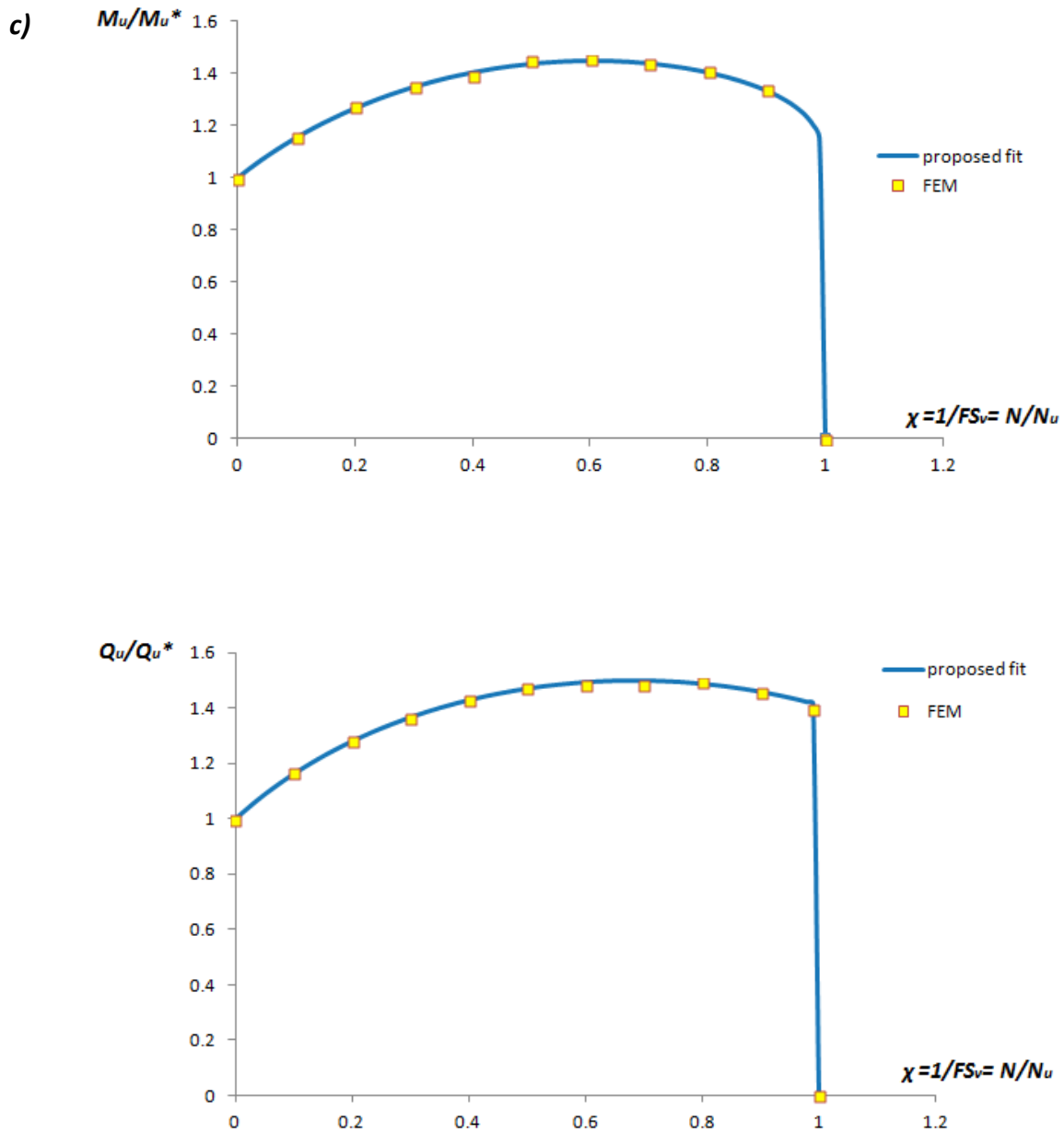
Figure 5.5 *The normalized ultimate moment and horizontal capacities derived from the FE analyses (data points) are compared to the proposed analytical expression (lines) for μ=1 and **α)** D/B=1 **b)** D/B=2 and **c)** D/B=3.*

a)
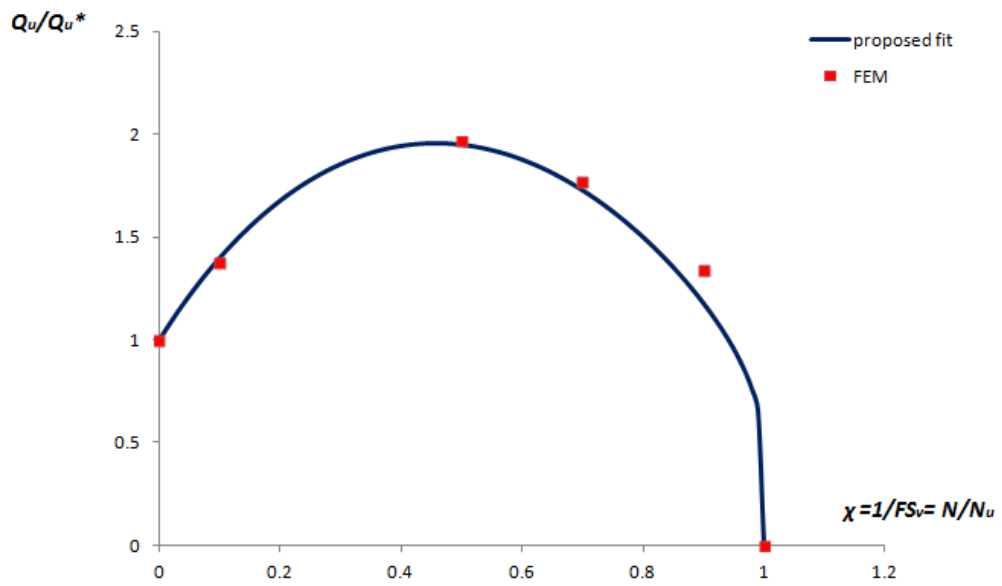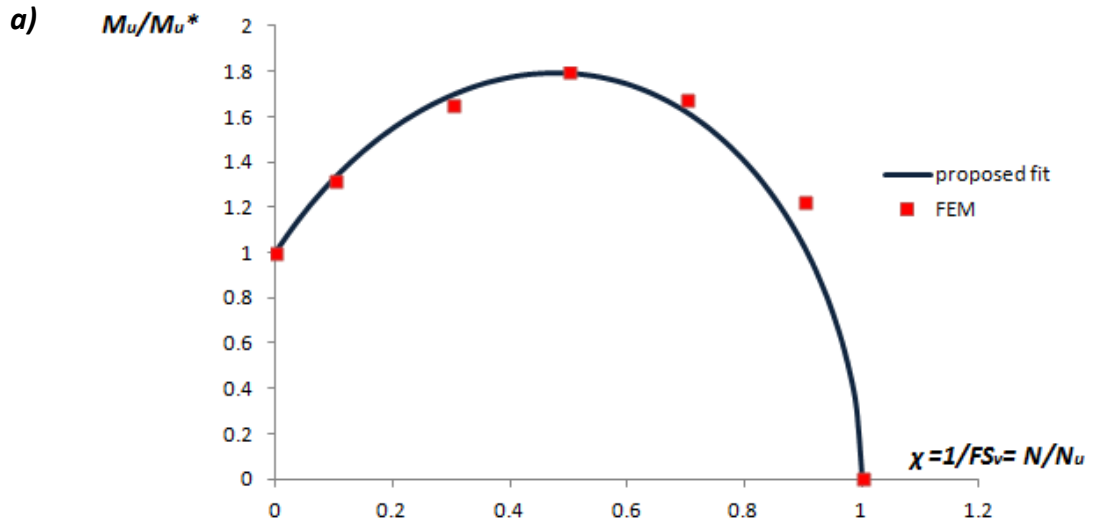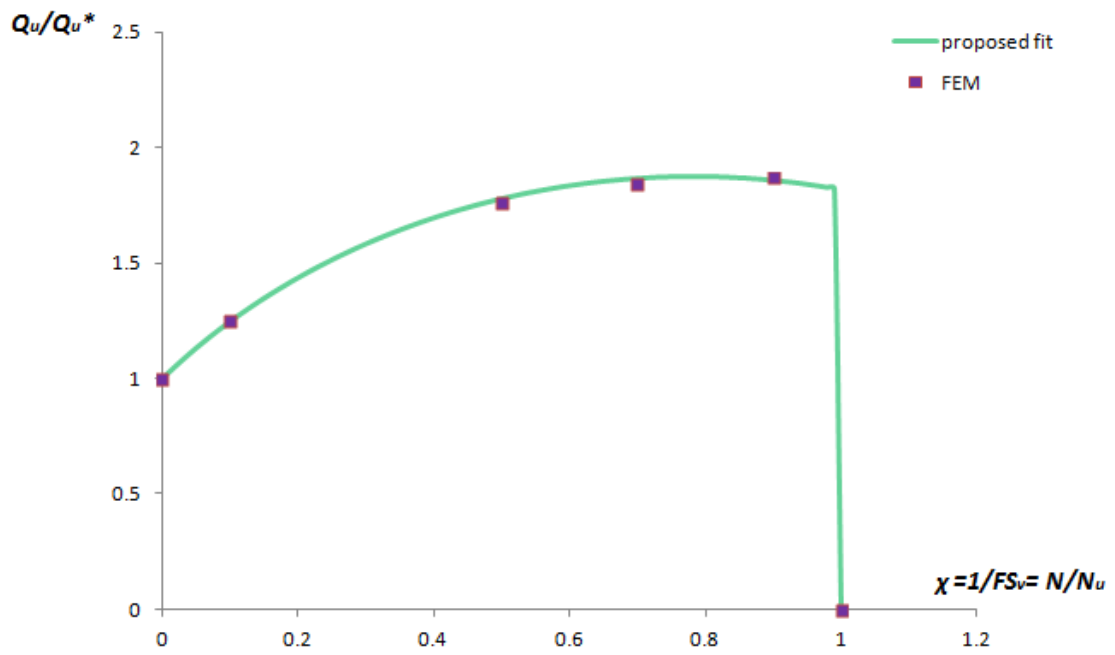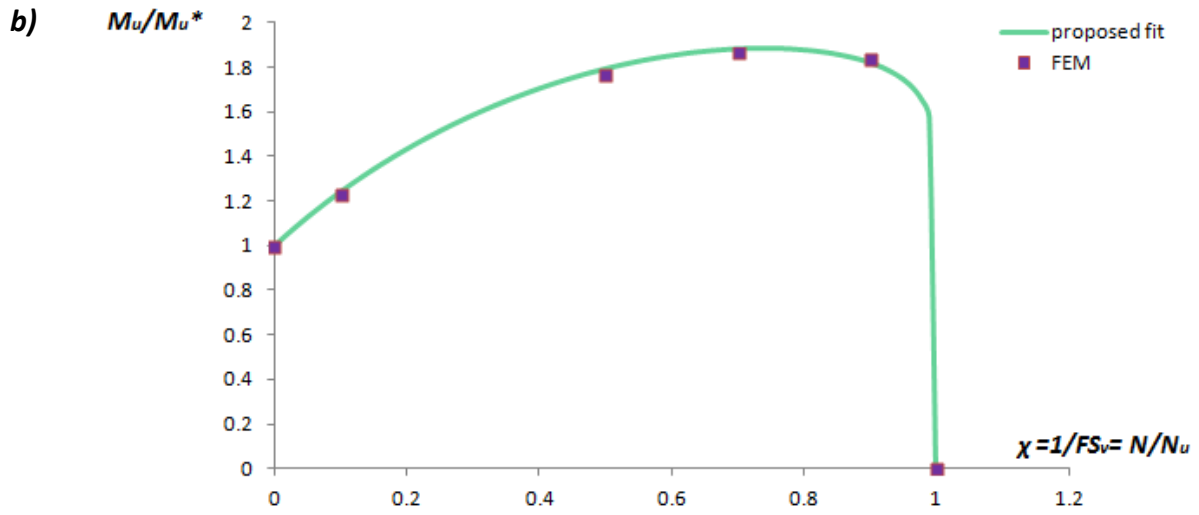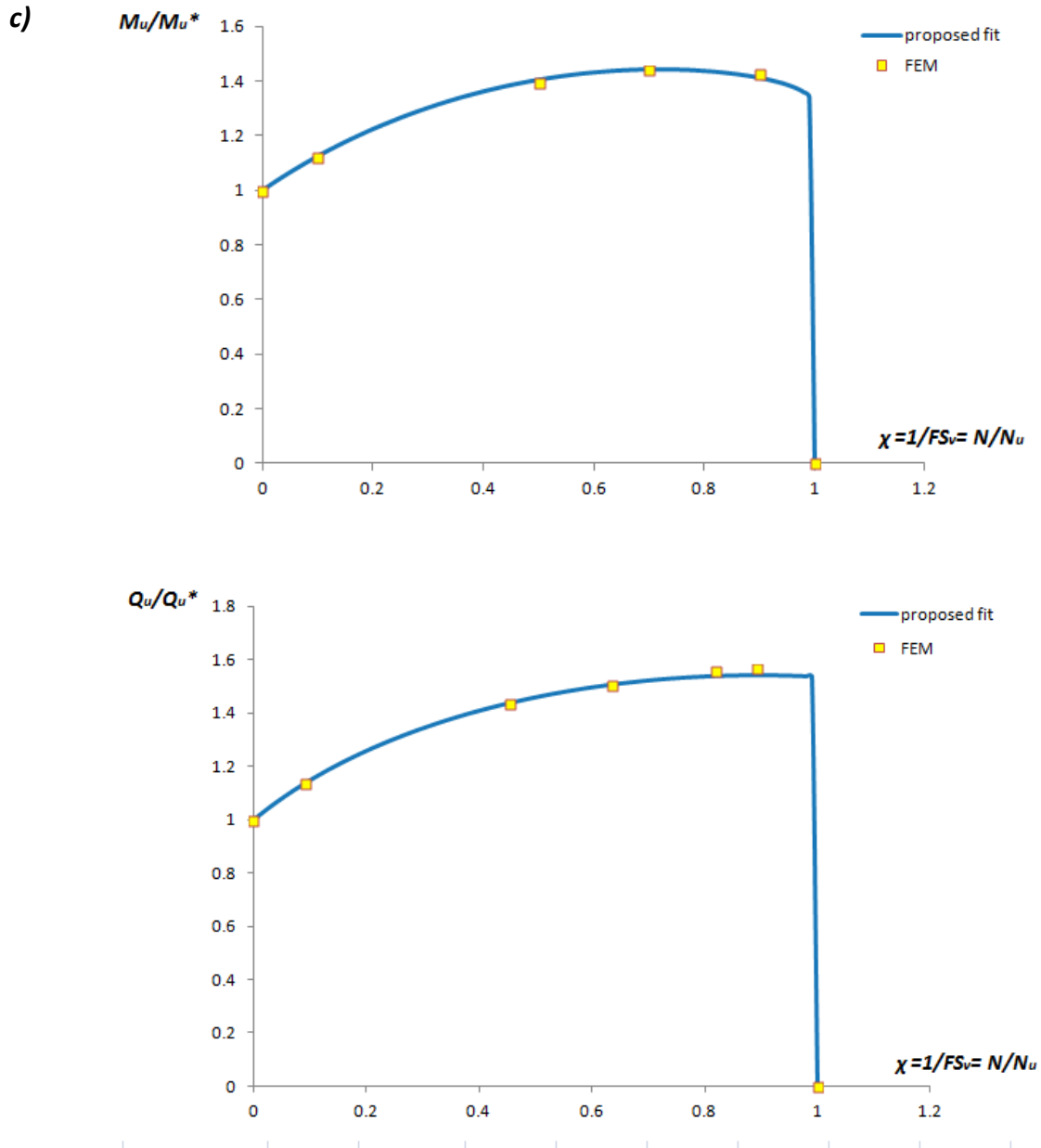
Figure 5.6 *The normalized ultimate moment and horizontal capacities derived from the FE analyses (data points) are compared to the proposed analytical expression (lines) for μ=0.5 and **α)** D/B=1 **b)** D/B=2 and **c)** D/B=3*
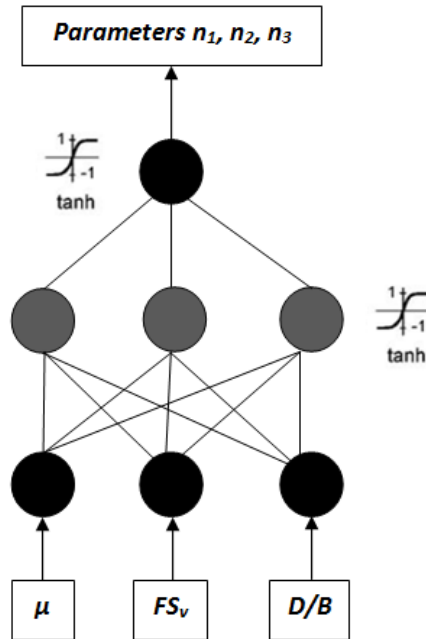
Figure 5.7 *Schematic representation of the neural network incorporated in the model.*

a)

| Parameter n_1						
Hidden Layer				**Output Layer**		
w1$_{i,j}$			**b1$_j$**	**w2$_j$**		**b2**
	i=1	**i=2**	**i=3**			
j=1	5.844	0.060	-0.105	-0.064	**j=1** 1.917	-0.305
j=2	-0.710	0.142	-0.266	0.024	**j=2** 3.572	
j=3	0.358	-5.176	0.669	5.012	**j=3** 1.023	

b)

Parameter n_2						
Hidden Layer					Output Layer	
w1$_{i,j}$			b1$_j$	w2$_j$		b2
	i=1	i=2	i=3			
j=1	2.053	5.570	9.210	2.998	**j=1** -0.981	-0.179
j=2	43.883	15.482	50.120	10.219	**j=2** 0.248	
j=3	8.964	-29.112	-9.321	-13.381	**j=3** -0.608	

c)

Parameter n_3						
Hidden Layer					Output Layer	
w1$_{i,j}$			b1$_j$	w2$_j$		b2
	i=1	i=2	i=3			
j=1	-23.599	-5.272	0.572	-15.732	**j=1** 102.407	1.859
j=2	15.032	0.141	-1.515	4.299	**j=2** 102.431	
j=3	1.149	0.154	2.316	2.419	**j=3** -1.912	

Figure 5.8 *The weights and biases of the hidden layer (w1$_{ij}$ and b1$_j$ – i representing the number of the input parameters and j the number of neurons)   as well as the weights and the biases of the output layer (w2$_j$ and b2) are presented for **a)** parameter n_1 **b)** parameter n_2 and **c)** parameter n_3*

a)

Parameter n_1

b)

Parameter n_2
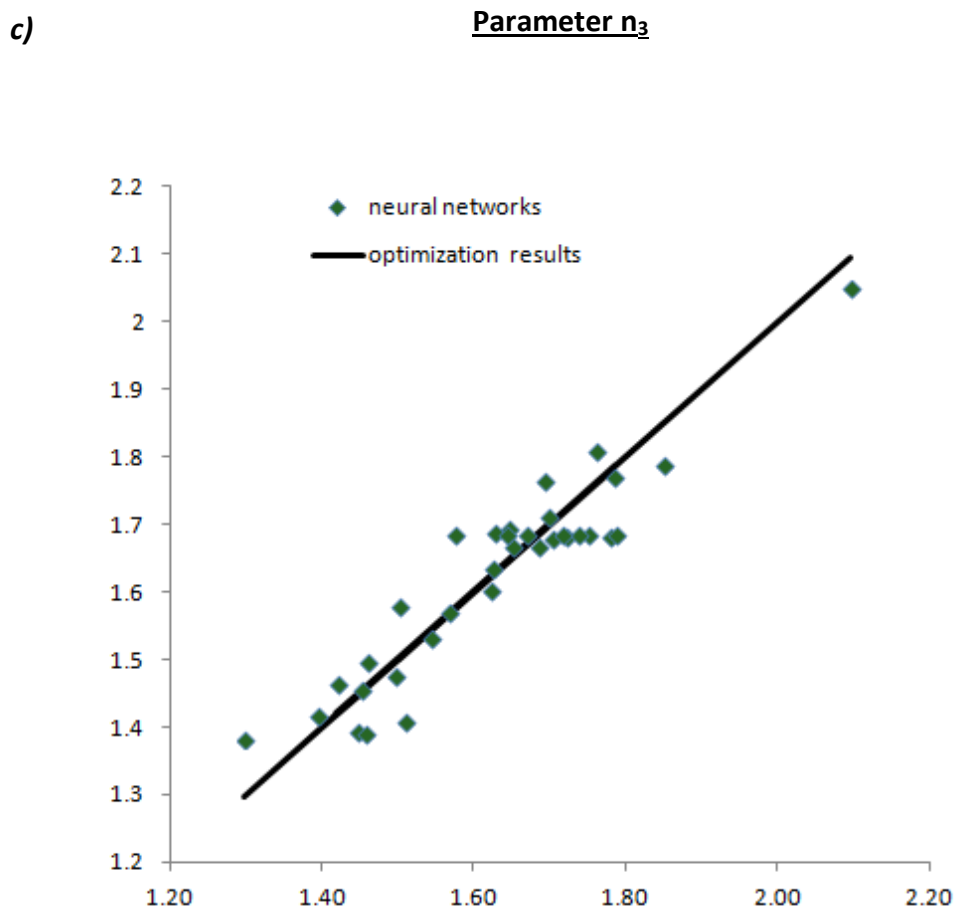
c)   **Parameter n_3**

Figure 5.9 *Comparison of the results from the neural networks to the results from the optimization of the data that derived from the three dimensional finite element analyses for **a)** parameter **n_1** **b)** parameter **n_2** and **c)** parameter **n_3***

a)

b)

c)
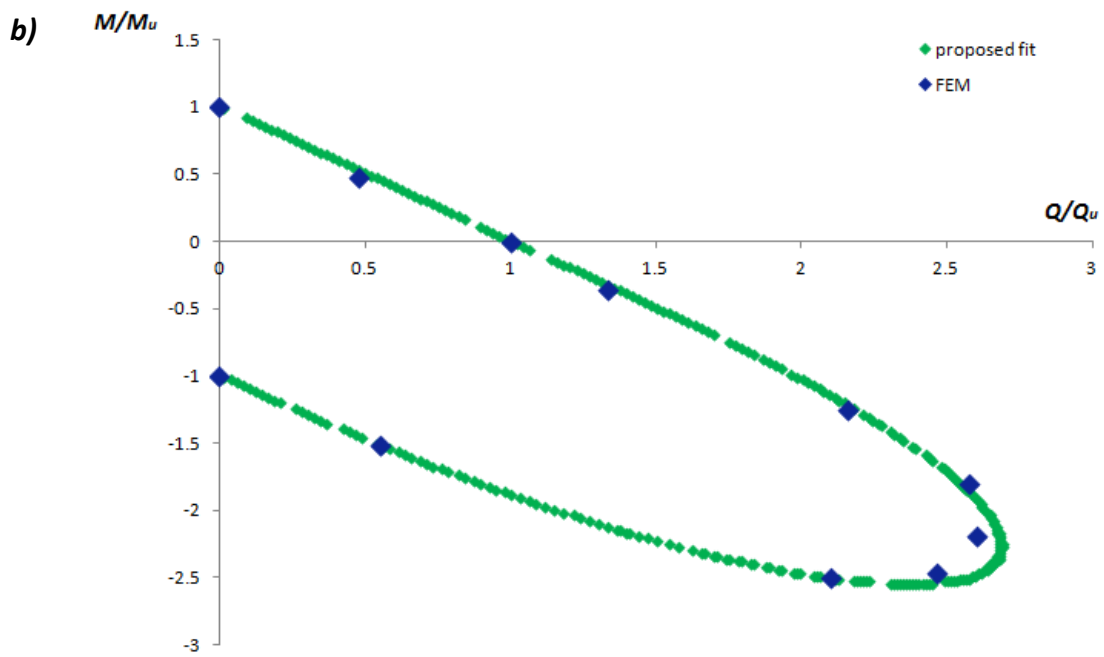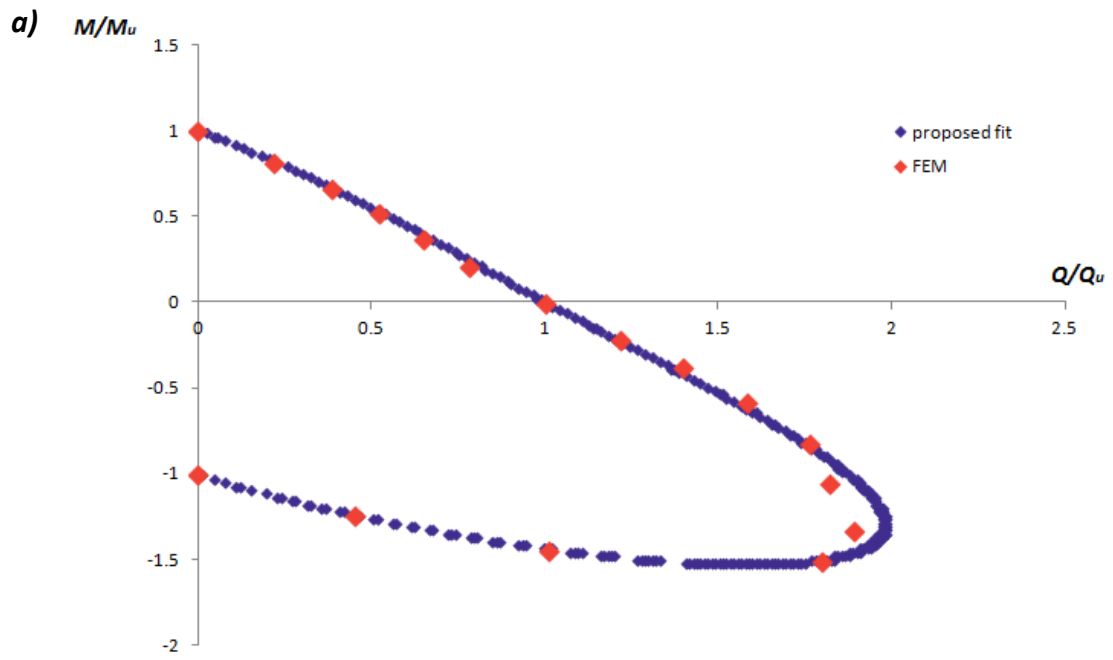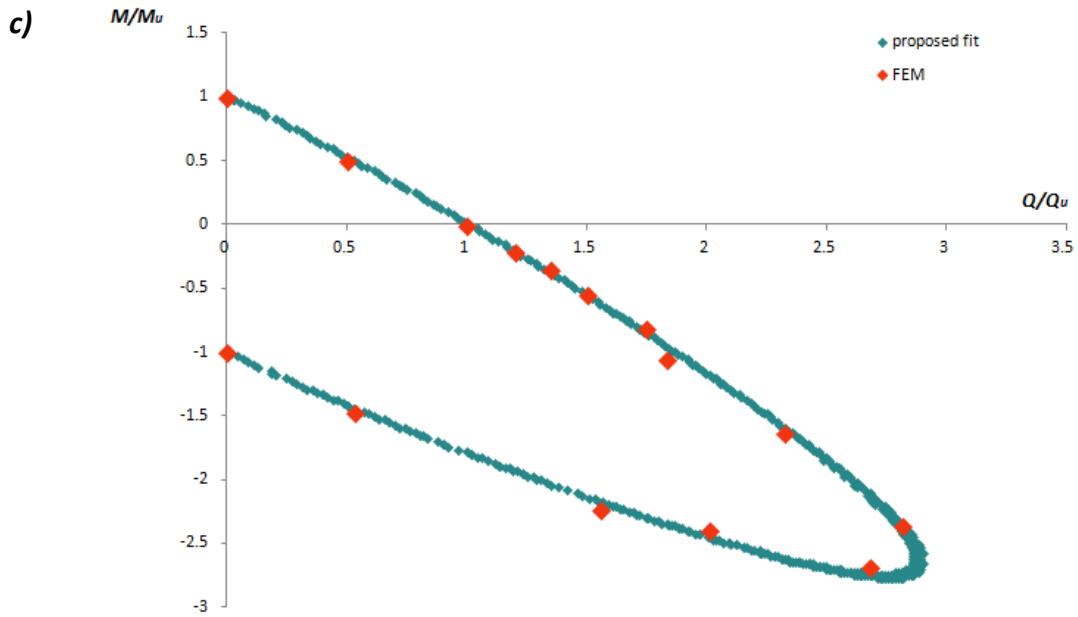
Figure 5.10 *Comparison between the data derived from the numerical experiments (points) and the analytical expression proposed for the yield surfaces of caisson foundations of a factor of safety $FS_v=10$, coefficient of friction $\mu=1$ and embedment ratio a) D/B = 1, b) D/B = 2 and c) D/B = 3*

α)

b)

c)
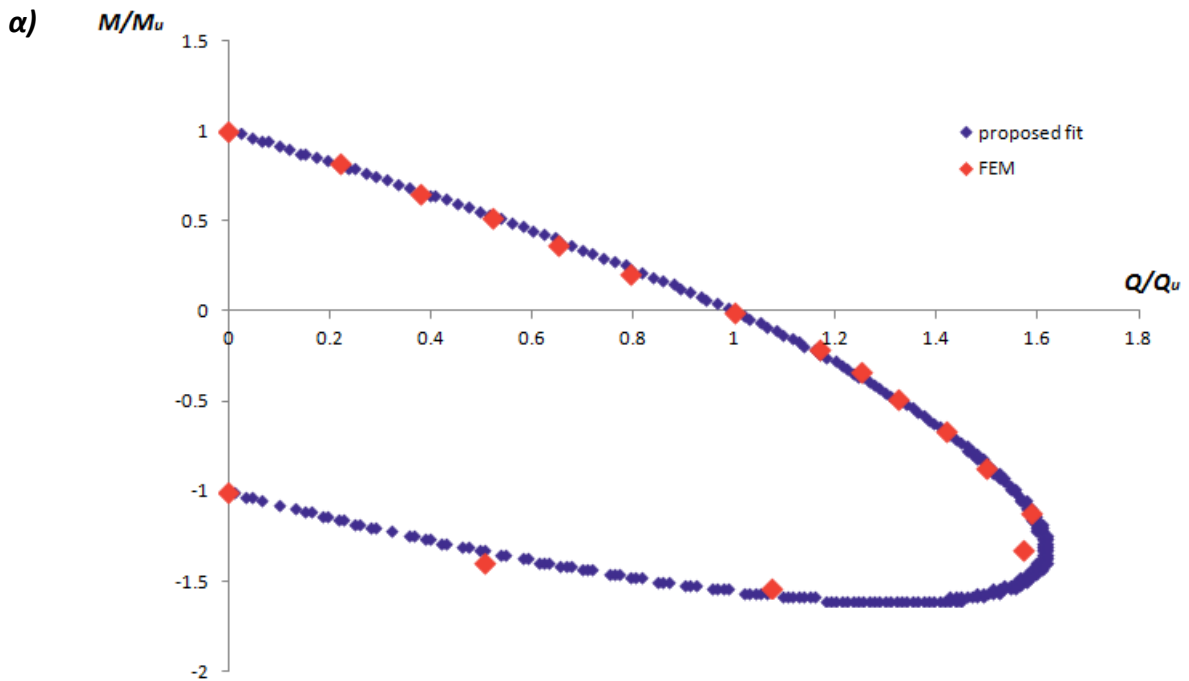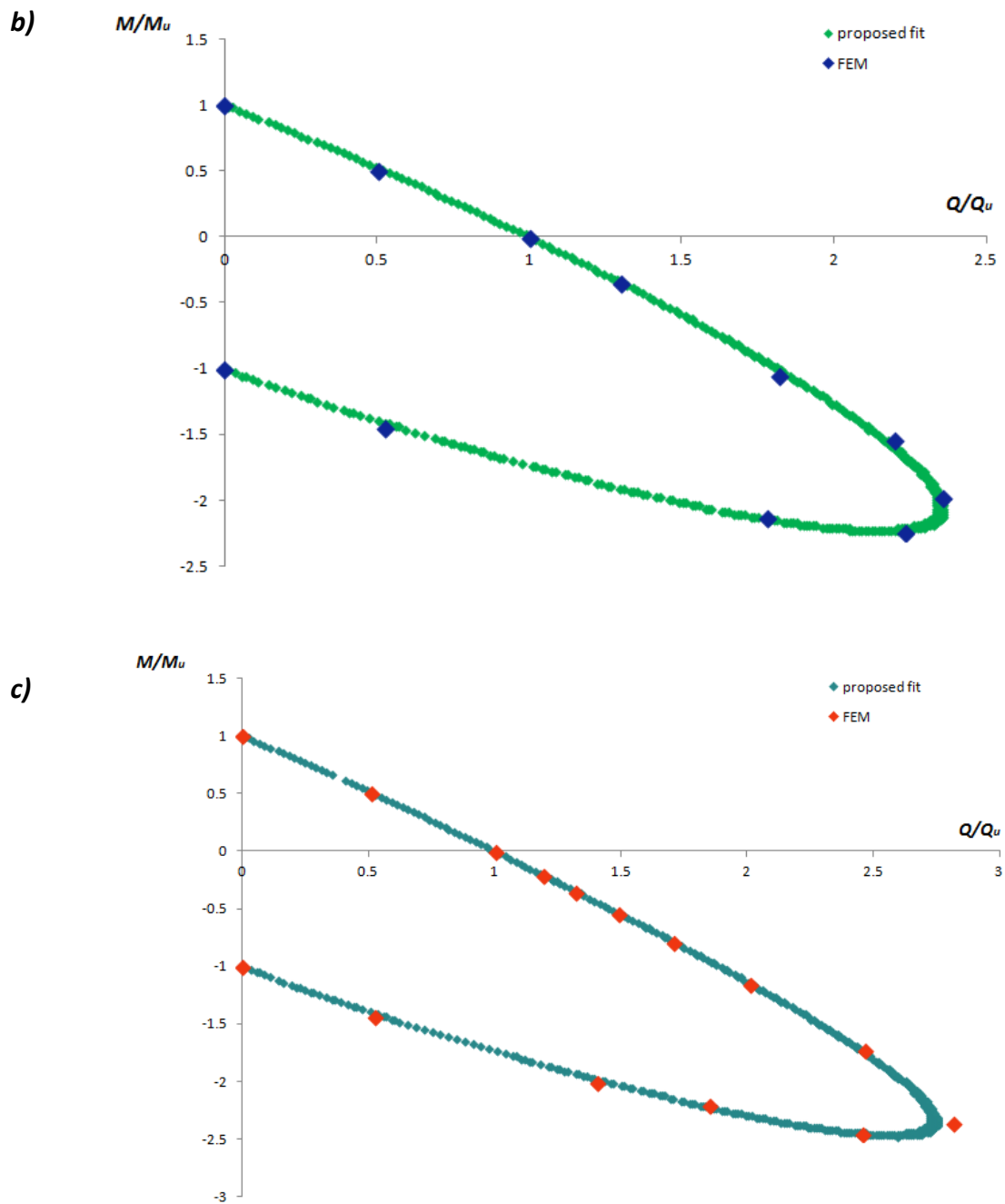
Figure 5.11 *Comparison between the data derived from the numerical experiments (points) and the analytical expression proposed for the yield surfaces of caisson foundations of a factor of safety $FS_v=2$, coefficient of friction $\mu=1$ and embedment ratio a) D/B = 1, b) D/B = 2 and c) D/B =3.*

a)

b)

c)
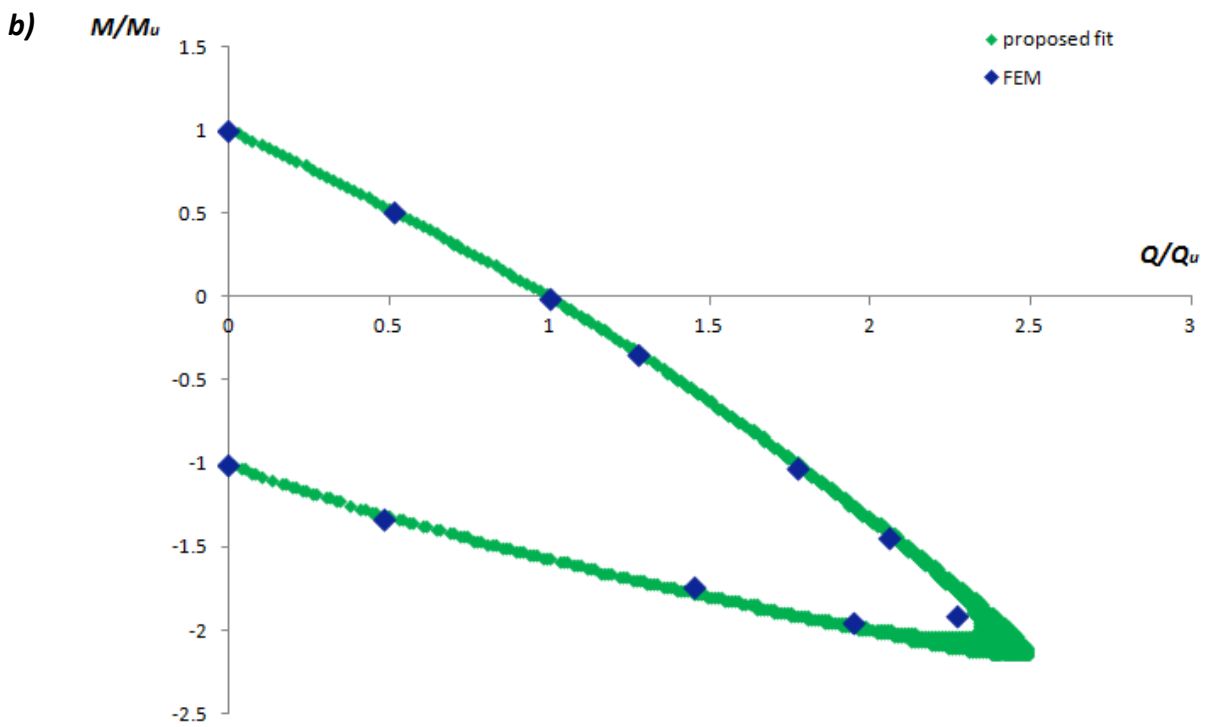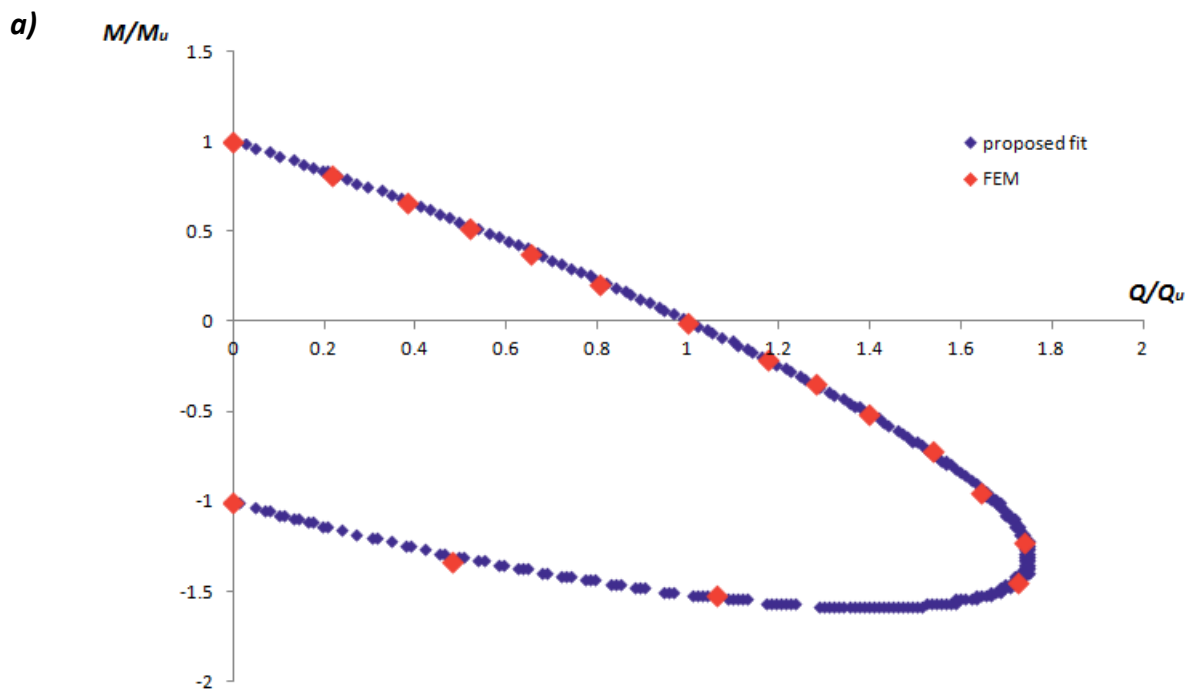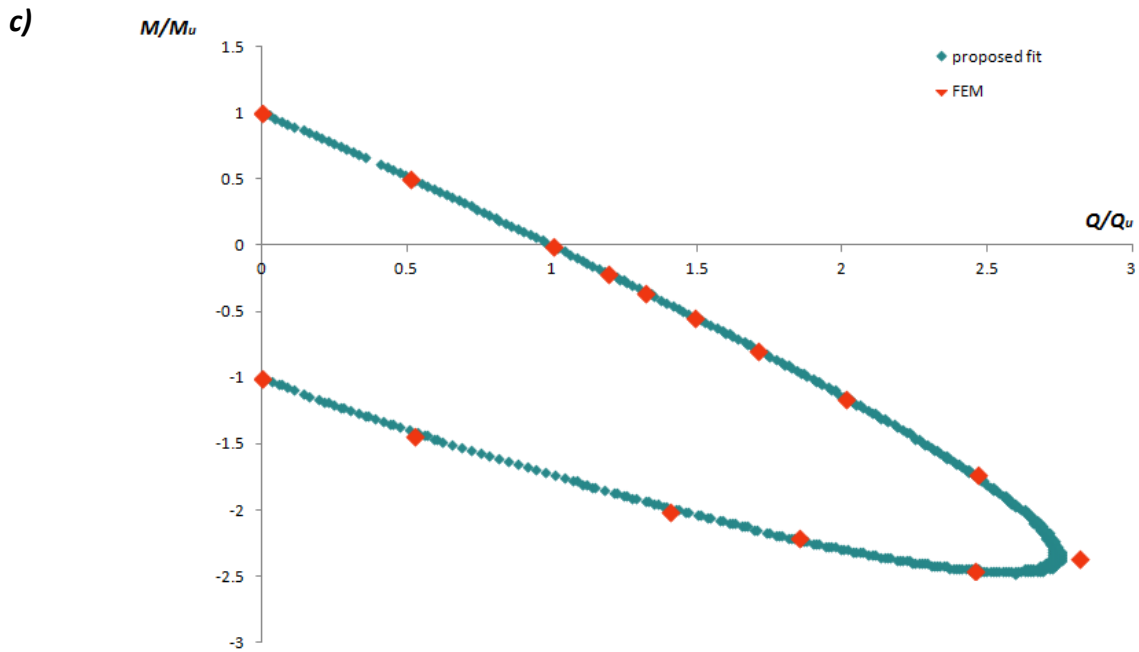
Figure 5.12 *Comparison between the data derived from the numerical experiments (points) and the analytical expression proposed for the yield surfaces of caisson foundations of a factor of safety $FS_v=1.11$, coefficient of friction $\mu=1$ and embedment ratio a) D/B = 1, b) D/B = 2 and c) D/B =3.*

a)

b)

c)
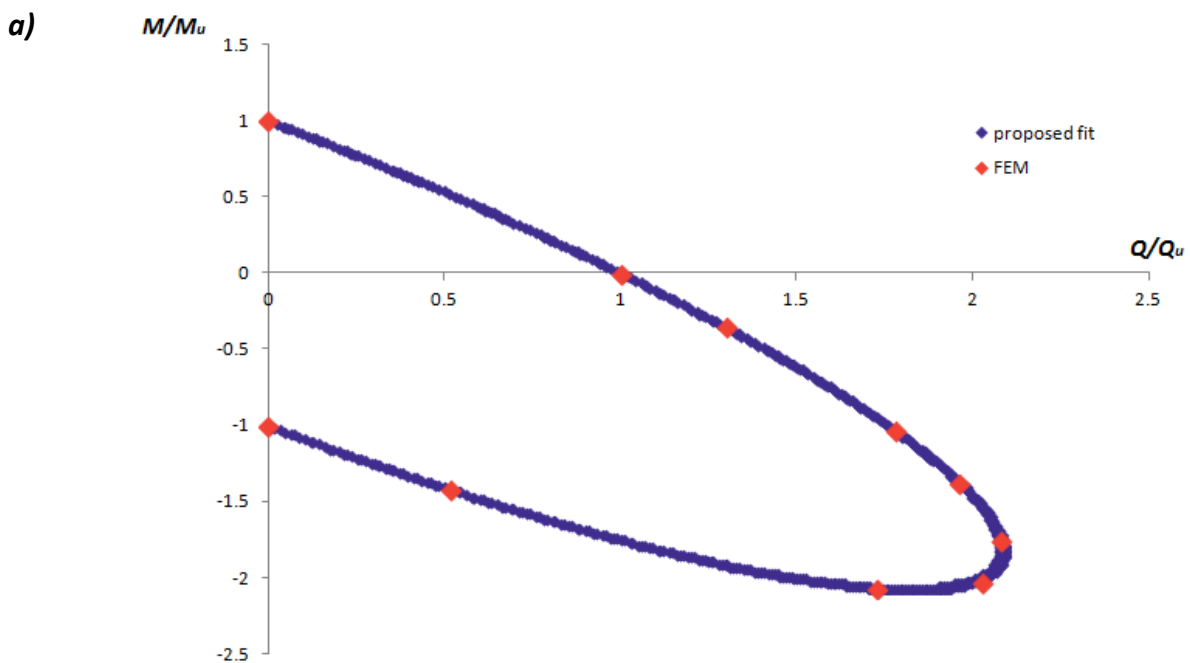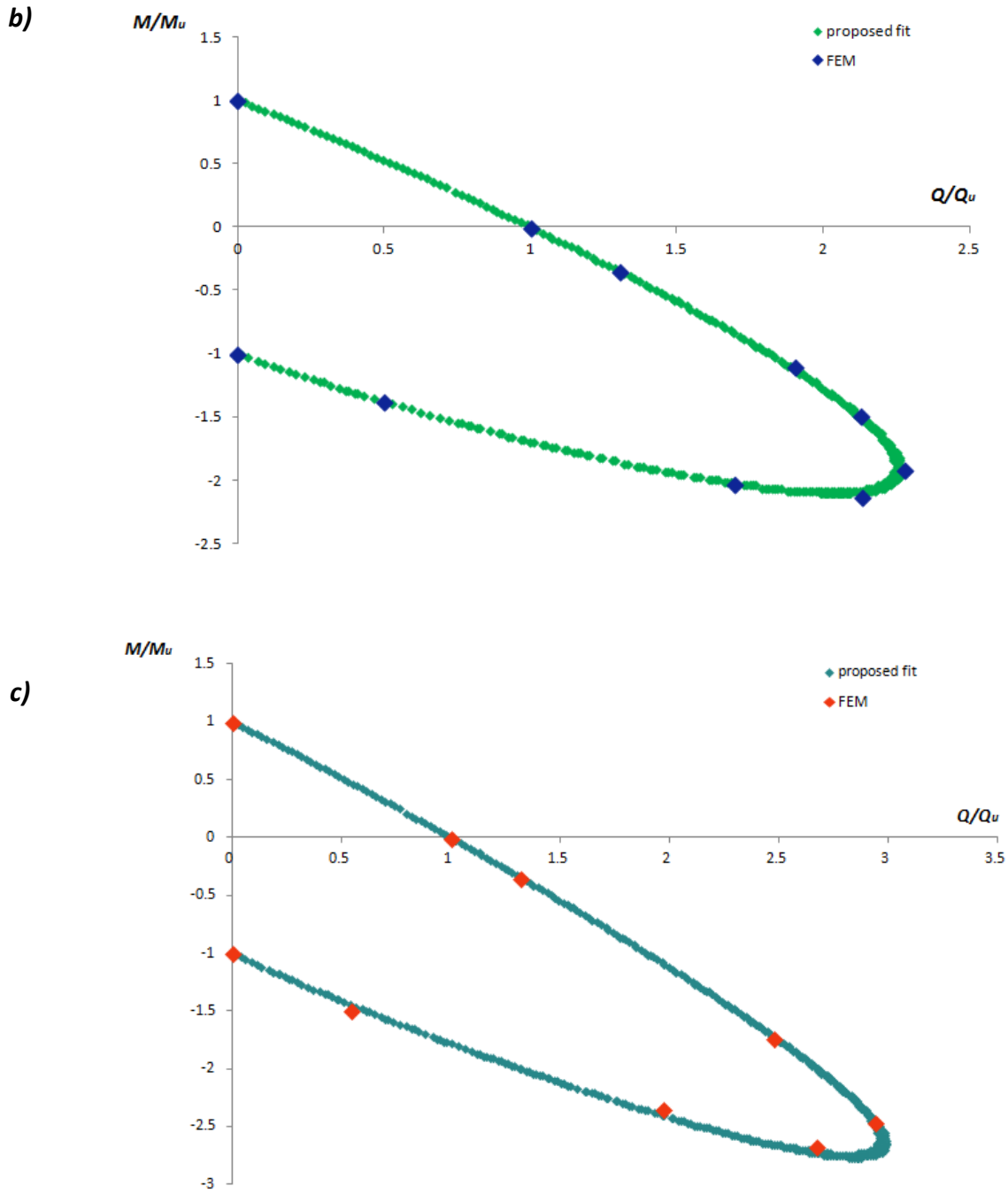
Figure 5.13 *Comparison between the data derived from the numerical experiments (points) and the analytical expression proposed for the yield surfaces of caisson foundations of a factor of safety $FS_v=2$, coefficient of friction $\mu=0.3$ and embedment ratio a) D/B = 1, b) D/B = 2 and c) D/B =3.*

a)

b)

c)
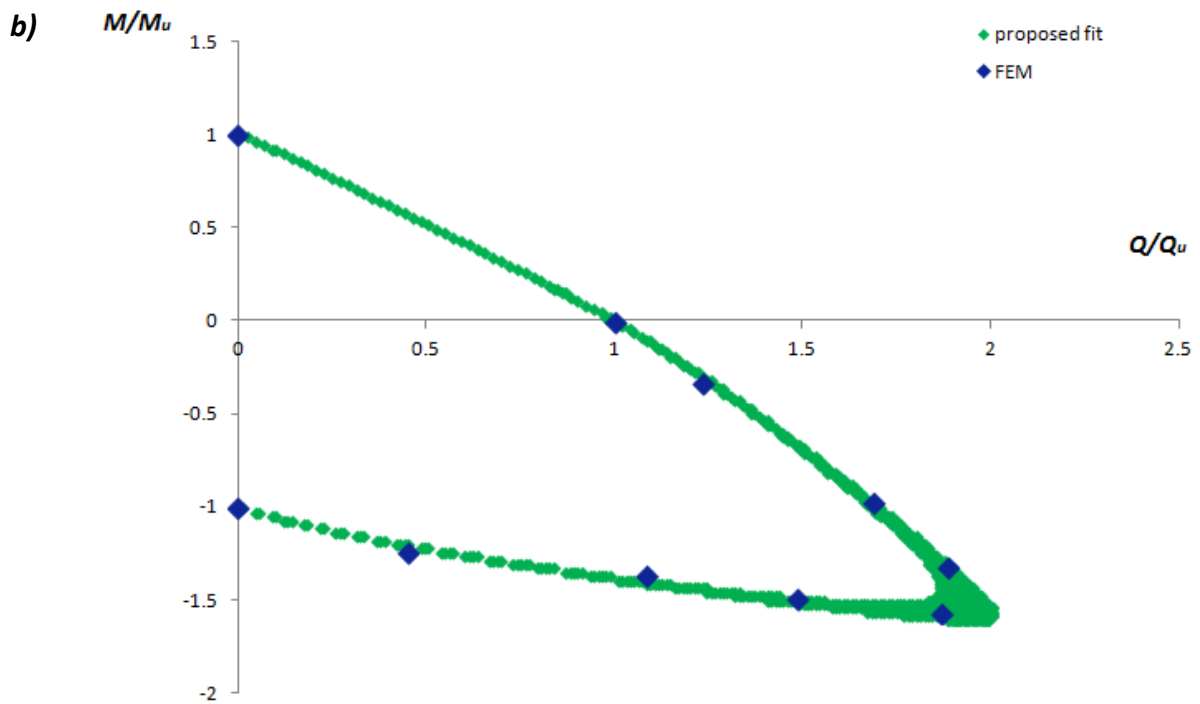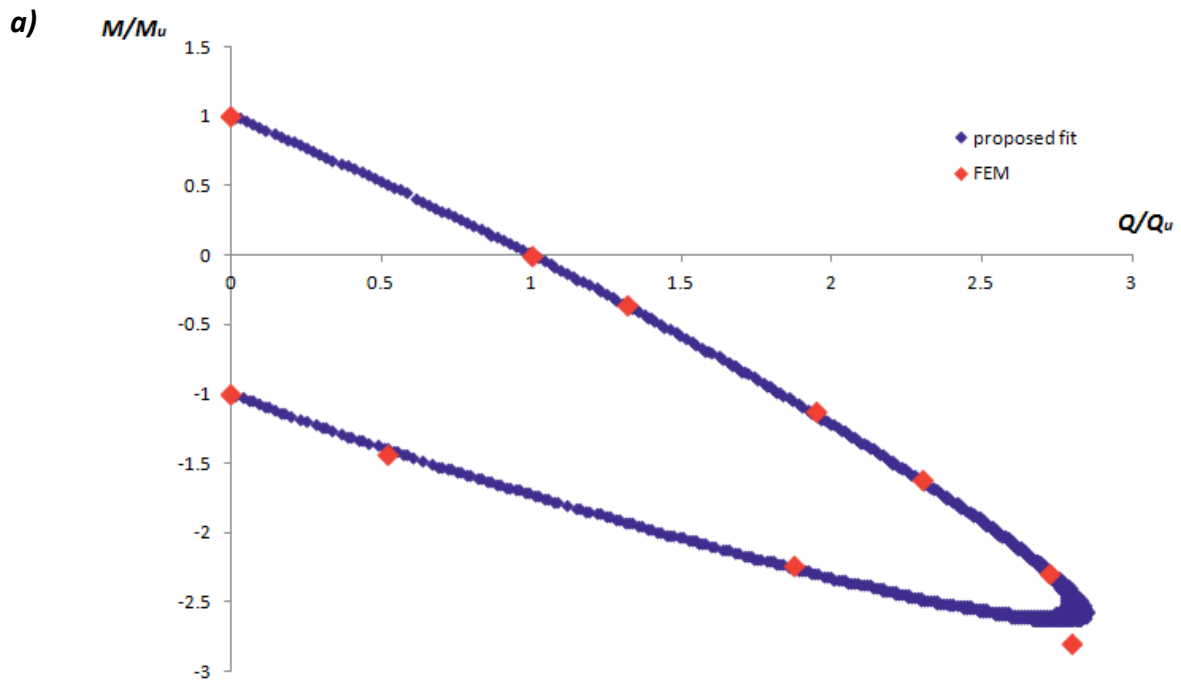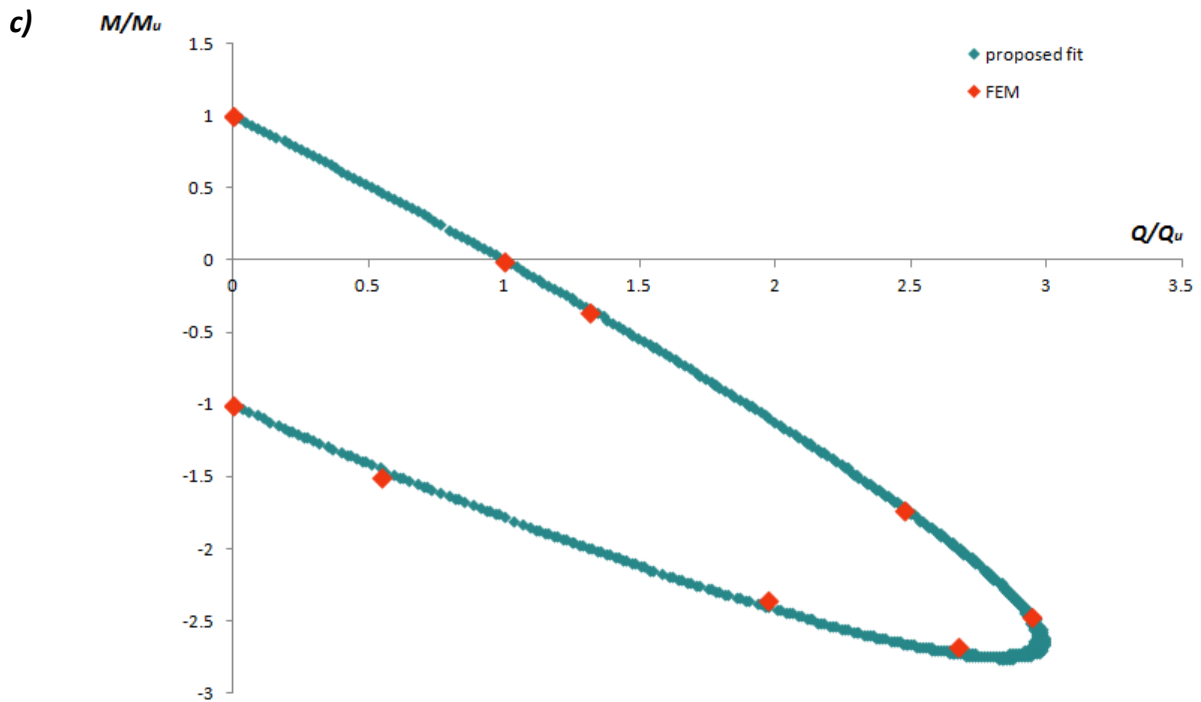
Figure 5.14 *Comparison between the data derived from the numerical experiments (points) and the analytical expression proposed for the yield surfaces of caisson foundations of a factor of safety $FS_v=1.11$, coefficient of friction $\mu=0.3$ and embedment ratio a) D/B = 1, b) D/B = 2 and c) D/B =3.*

CHAPTER 6

CONCLUSIONS

6.1 *Conclusions*

This thesis dealt with the behavior of caisson foundations embedded in cohesionless soil and subjected to combined axial and lateral loading. After developing appropriate Finite Element models for the soil-foundation system, numerous experiments were carried out that served the purpose of our work.

Our first aim was to produce the failure envelopes of caisson foundations under combined *M-Q-N* loading, examining different coefficients of friction, embedment ratios and factors of safety against vertical loading. Furthermore, an effort was made to thoroughly examine the soil deformation mechanisms that are manifested along a failure envelope. Finally, following the work of Gerolymos et al in the case of cohesive soil, we determine analytical expressions that represent these failure envelopes.

The important conclusions that were drawn from this thesis are presented below:

- As part of our approach to the failure envelopes of embedded foundations, we first determine the ultimate horizontal and moment capacities of caisson

foundations as functions of the following parameters: 1) the embedment ratio *D/B* (for values *1, 2* and *3*)*, 2)* the factor of safety against vertical bearing capacity *FS_v =* FS_v = *1.11, 1.25,1.43, 1.67, 2, 2.5, 3.33, 5* and *10* and 3) the coefficient of friction *μ*, for values *0.3, 0.5* and *1.* The limit values of μ are carefully chosen to correspond to a very smooth and a rough interface. For smaller embedment ratios the influence of the vertical load as well as the coefficient of friction are evident: both the moment and the horizontal capacity increase until they reach their maximum for χ~0.5 and then decline and are nullified for χ=1. Additionally, for a smoother interface the values of the capacities are remarkably smaller. However, as the embedment ratio increases, the vertical load and the friction cease to have a significant impact on the shape of the normalized M-N curve. We also observe that for larger embedment ratios (D/B>2) and especially for a smooth interface (μ<0.5) the foundation's lateral capacity declines abruptly for value of χ=1.

- Afterwards, the yield surfaces in the M-Q plane are determined through force-controlled tests. For an embedment ratio D/B=1 the failure envelopes demonstrate a distinct variability in the branch of over strength with respect to the safety factor FS_v and the coefficient of friction *μ* has a considerable effect on the shape of the yield locus. However, for greater embedment ratios this distinct variability is no longer observed, with the failure envelopes coinciding for D/B=3 and different factors of safety and coefficients of friction. Furthermore, as the embedment ratio increases the failure envelopes exhibit a significant expansion, with a rate that appears to decline for foundations of embedment ratio greater than D/B=2. It is also worth noting that in these failure envelopes quantities M and Q were normalized by their ultimate capacities, since the dimensionless failure envelopes demonstrate a significant rotation with respect to the embedment ratio that constitutes them difficult to compare.

- Prior to the analytical representation of the yield surface, we delve into a thorough examination and categorization of the characteristic points of failure and of the soil deformation mechanisms that develop along the failure envelope. We classify the characteristic points into five different categories : scoop (M_u), scoop-slide (Q_u), inverted pendulum ($z_p = D$), pure sliding (Q_{max}, $z_p = \infty$) and pendulum (M_{max}, $z_p = 0$). We are then able to map the yield locus on the M-Q plane; apart from the already referenced *scoop, scoop-slide*, *pure sliding* and *reverse scoop* mechanisms, another mechanism is suggested governing the region between maximum horizontal and maximum moment capacity in deeply embedded caissons. This mechanism accounts for a generalized (*"diffusive"*) soil failure around the caisson, with no plastic strain localization (shear band) being developed except for the base of the caisson. In this narrow region of special interest, the depth of the caisson pivot point rapidly changes from *z = 0* to *z = ∞*.

- After successfully mapping the yield locus on the M-Q plane, we deal with the analytical representation of both the ultimate capacities. We produce analytical expressions for the normalized ultimate lateral capacities. The expressions derived from fitting the finite element analyses results are functions of the safety factor FS_v and of parameters that are dependent on the coefficient of friction μ and the embedment ratio D/B. The complexity of those parameters did not allow us to produce a simple expression for them. Then, we compared the analytical fit to the data from the finite element analyses and validated our results.

- Finally, we provide an analytical fit for the failure envelopes; we use the yield equation introduced by Gerolymos et al as input in an optimization procedure, but the highly non-linear behavior of the variables n_1, n_2 and n_3 of the

yield equation made it extremely difficult to produce analytical expressions for them and led us to train three neural networks, whose weights and biases we provide. Then, we compared the analytical fit to the data that had derived from the finite element analyses, thus validating our results.

REFERENCES

ABAQUS 6.1. (2001). Standard user's manual. Rhode Island: Hibbit, Karlsson and Sorensen. Beredugo YO, Novak M. Coupled horizontal and rocking vibration of embedded footings. Can Geotech J 1972;9(4):477–97.

Bransby, M. F. & Randolph, M. F. (1997). Shallow foundations subject to combined loadings. Proc. 9th Int. Conf. on Computer Methods and Advances in Geomechanics, Wuhan 3, 1947–1952.

Bransby, M. F., Randolph, M. F. (1998). Combined loading of skirted foundations, Geotechnique, 48(5): 637-655.

Bransby, M. F. & Randolph, M. F. (1999a). The effects of embedment on the undrained response of caisson foundations to combined loadings. Soils Found. 39, No. 4, 19–34.

Bransby, M. F. & Randolph, M. F. (1999b). The effect of skirted foundation shape on response to combined V-M-H loadings. Int. J. Offshore Polar Engng 9, No. 3, 214–218.

Chatzigogos, C. T., Figini, R., Pecker, A. and Salençon, J. (2011). A macroelement formulation for shallow foundations on cohesive and frictional soils. Int. J. Numer. Anal. Meth. Geomech. 2011; 35:902–931

Crémer C. Modélisation du comportement non linéaire des fondations superficielles sous séisme. PhD thesis, Laboratoire de Mécanique et de Technologie, ENS – Cachan, France, 2001.

Crémer C, Pecker A, Davenne L. Cyclic macro-element for soil-structure interaction: material and geometrical non linearities. International Journal for Numerical and Analytical Methods in Geomechanics 2001; 25: 1257 – 1284.

Dominguez J. Dynamic stiffness of rectangular foundations. Research Report R78-20. Department of Civil Engineering, Massachusetts Institute of Technology, Cambridge; 1978.

Gadre A, Dobry R. Lateral cyclic loading centrifuge tests on square embedded footing. J Geotech Geoenviron Eng ASCE 1998;124(11): 1128–38.

Gazetas G, Dobry R, Tassoulas JL. Vertical response of arbitrarily shaped embedded foundations. J Geotech Eng ASCE 1985;111(6):750–71.

Gazetas G, Tassoulas J. Horizontal stiffness of arbitrarily shaped embedded foundations. J Geotech Eng ASCE 1987;113(5):440–57.

Gazetas G, Tassoulas JL. Horizontal damping of arbitrarily shaped embedded foundations. J Geotech Eng ASCE 1987;113(5):458–75.

Gazetas G. Formulas and charts for impedances of surface and embedded foundations. J Geotech Eng ASCE 1991;117(9):1363–81.

Gerolymos N, Gazetas G (2006) Winkler model for lateral response of rigid caisson foundations in linear soil. Soil Dynamics and Earthquake Engineering 26 (2006), pp 347–361

Gerolymos N, Gazetas G (2006) Development of Winkler model for static and dynamic response of caisson foundations with soil and interface nonlinearities. Soil Dynamics and Earthquake Engineering 26 (2006), pp 363–376

Gerolymos N, Gazetas G (2006) Static and dynamic response of massive caisson foundations with soil and interface nonlinearities - Validation and results. Soil Dynamics and Earthquake Engineering 26 (2006), pp 377–394

Gerolymos N, Zafeirakos A and Souliotis C (2012). Insight to failure mechanisms of caisson foundations under combined loading: A macro-element approach. Proc. 2nd Int. Conf. on Performance-based design in Earthquake Geotechnical Engineering, Taormina, Italy

Gerolymos N, Vardoulakis I, Gazetas G (2007) A thermo-poro-visco-plastic shear band model for seismic triggering and evolution of catastrophic landslides. Soils and Foundations Vol 47, No 1, 11-25, Feb 2007

Giannakos S, Gerolymos N, Gazetas G (2012) Cyclic lateral response of piles in dry sand: Finite Element modeling and validation. Computers and Geotechnics 44 (2012) 116–131

Gottardi G, Butterfield R. The displacement of a model rigid surface footing on dense sand under general planar loading. Soils and Foundations 1995; 35(3):71–82.

Gottardi G, Houlsby GT, Butterfield R. Plastic response of circular footings on sand under general planar loading. Géotechnique 1999; 49(4): 453 – 469

Gourvenec, S. & Randolph, M. F. (2003). Effect of strength nonhomogeneity on the shape and failure envelopes for combined loading of strip and circular foundations on clay. Geotechnique 53, No. 6, 575–586.

Gourvenec, S. "Bearing capacity under combined loading - a study of the effect of shear strength heterogeneity". Proc. , 9th Australian and New Zealand Conference on Geomechanics, Auckland, New Zealand, 2004, pp. 527-533

Gourvenec, S. (2007). Failure envelopes for offshore shallow foundation under general loading, Geotechnique, 57(9): 715-728.

Gourvenec, S. (2008). Effect of embedment on the undrained capacity of shallow foundations under general loading, Geotechnique, 58(3): 177-185.

Harada T, Kubo K, Katayama T. Dynamic soil–structure interaction analysis by continuum formulation method. Report of the Institute of Industrial Science, vol. 29. The University of Tokyo; 1981 [issue no. 5].

Karabalis DL, Beskos DE. Dynamic response of 3-D embedded foundations by the boundary element method. Comput Methods Appl Mech Eng 1986;56:91–119.

Karapiperis K, Gerolymos N. (2012) Insight to the numerical modeling of the lateral response of caisson foundations to static and cyclic loading. DSpace at NTUA

Kausel E, Roesset JM. Dynamic stiffness of circular foundations. J Eng Mech Div ASCE 1975;101(6):770–85.

Martin, C. M. & Houlsby, G. T. (2000). Combined loading of spudcan foundations on clay: laboratory tests. Geotechnique 50, No. 4, 325–338.

Martin, C. M. & Houlsby, G. T. (2001). Combined loading of spudcan foundations on clay: numerical modelling. Geotechnique 51, No. 8, 687–699.

Mitta A, Luco JE. Dynamic response of a square foundation embedded in an elastic half space. Soil Dyn Earthq Eng 1989;8.

Nova, R. & Montrasio, L. (1991). Settlements of shallow foundations on sand. Geotechnique 41, No. 2, 243–256.

Roscoe KH, Schofield AN. The stability of short pier foundations on sand. British Welding Journal 1956; August: 343–354.

Roscoe, K. H., Schofield, A. N. (1957). The stability of short pier foundations in sand, discussion, British Welding Journal, January, 12-18.

Saitoh M. Effective seismic motion of caisson and pile foundation. RTRI Rep 2001;46.

Souliotis C, Gerolymos N. (2012) Development of macroelement for lateral response of caisson foundation to static and cyclic loading. DSpace at NTUA

Tajimi H. Dynamic analysis of a structure embedded in an elastic stratum. Proceedings of the fourth world conference on earthquake engineering, Santiago, Chile; 1969

Tassoulas JL. Elements for the numerical analysis of wave motion in layered media. Research Report R81-2. Department of Civil Engineering, Massachusetts Institute of Technology, Cambridge; 1981.

Ticof, J., (1977). "Surface footings on sand under general planar loads", PhD thesis, University of Southampton.

Ukritchon, B., Whittle, A. J. & Sloan, S. W. (1998). Undrained limit analyses for combined loading of strip footings on clay. J. Geotech. Geoenviron. Engng ASCE 124, No. 3, 265–276.

Zaharescu, E. (1961). Sur la stabilite des fondations rigides. Proc. 5th Int. Conf. Soil Mech., Paris 1, 867–871